Modified Dual Second-order Generalized Integrator FLL for Frequency Estimation Under Various Grid Abnormalities

Kalpeshkumar R. Patil and Hiren H. Patel

***Abstract*—Proper synchronization of Distributed Generator with grid and its performance in grid-connected mode relies on fast and precise estimation of phase and amplitude of the fundamental component of grid voltage. However, the accuracy with which the frequency is estimated is dependent on the type of grid voltage abnormalities and structure of the phase-locked loop or frequency locked loop control schemes. Among various control schemes, second-order generalized integrator based frequency-locked loop (SOGI-FLL) is reported to have the most promising performance. It tracks the frequency of grid voltage accurately even when grid voltage is characterized by sag, swell, harmonics, imbalance, frequency variations etc. However, estimated frequency contains low frequency oscillations in case when sensed grid-voltage has a dc offset. This paper presents a modified dual second-order generalized integrator frequency-locked loop (MDSOGI-FLL) for three-phase systems to cope with the non-ideal three-phase grid voltages having all type of abnormalities including the dc offset. The complexity in control scheme is almost the same as the standard dual SOGI-FLL, but the performance is enhanced. Simulation results show that the proposed MDSOGI-FLL is effective under all abnormal grid voltage conditions. The results are validated experimentally to justify the superior performance of MDSOGI-FLL under adverse conditions.**

Keywords—Grid synchronization, phase-locked loop, frequency locked loop, second-order generalized integrator.

I. INTRODUCTION

Grid synchronization is an adaptive process in which an internal reference signal generated by the synchronization control algorithm allows power converter output signal to work in synchronism with a fundamental component of the grid voltage. Hence, for the converter to perform satisfactorily, it is desired that the control algorithm correctly derives this reference signal from the grid voltages. However, it is a challenging task especially when the grid voltage is characterized by the presence of different grid abnormalities (voltage fluctuation, harmonics, frequency variation and/or distortion, dc offset, switching notches etc.).The issue is more dominant in a microgrid (or a weak grid) where the effect of non-linear loads, faults, sudden load changes etc., are translated in form of distortion in grid voltage, frequency change, imbalance etc. to a greater extent than that in a stiff or strong grid. Such irregularities may introduce measurement and data conversion errors and hence, makes the task of estimating frequency and synchronization difficult. In addition, the microgrid is likely to have variety of distributed generators (DG) interfaced through static converters, which increases the severity of the problem and makes the task of frequency estimation still more difficult [1-4].

The frequency estimation can be carried out with frequency-domain or time-domain techniques. The frequency-domain techniques based on the discrete Fourier transform (DFT) suffers from the computational burden, accumulation errors etc. Also, complexity in actual implementation increases in case where the measured signal is highly distorted [5-7]. Unlike these methods, several advantages of time-domain techniques like; ease of implementation, reliability, good dynamic response, higher accuracy, low sensitivity to the frequency variations and unbalanced grid voltage etc.; have increased the popularity of the time domain approach based on closed loop phase-locked loop (PLL) for estimating the frequency. The basic structure of a PLL comprises of the phase detector (PD) block, filter and a voltage controlled oscillator (VCO). The PD is responsible for adjusting the gain of VCO whose output signal is synchronized (in terms of phase and frequency) with the input reference signal. The classification of PLL with different PD is discussed in [8-11]. Their performances in single-phase power system network are evaluated under the different grid severity. The three-phase conventional PLL based on the synchronous reference frame (SRF) have superior performance in the balanced grid voltage signal. But, it gives the oscillatory response for the estimated fundamental frequency, if measured grid voltage signal is unbalanced or distorted [12]. The poor performance of the conventional PLL was improved by the technique reported in [13], which employs decoupled double synchronous reference frame PLL (DDSRF-PLL). The DDSRF-PLL decouples the fundamental positive and negative sequence components to estimate the frequency. It results into accurate estimation in case of unbalanced grid voltage signal. However, performance deteriorates when grid signal is distorted. It is observed that PD structure based on the generalized integrator (GI) have a better performance and reliability [14] under such distorted gird signal conditions. Hence, the second-order generalized integrator based PLL (SOGI-PLL) is superior to other configurations. It performs fast and accurately under the adverse grid conditions. Unlike SOGI-PLL where the

K. R. Patil is with the Department of Electrical Engineering Sarvajanik College of Engineering & Technology, Surat, India. (e-mail: kalpesh.patil@scet.ac.in).

H. H. Patel is with the Department of Electrical Engineering, Sarvajanik College of Engineering & Technology, Surat, India. (e-mail: hiren.patel@scet.ac.in).

estimated frequency is used as feedback from the PLL block in the structure of SOGI block, the frequency can be adaptively obtained through frequency-locked loop (FLL) in SOGI-FLL structure to get superior performance. This avoids the PLL and the adaptive nature enhances the performance [15-18]. Two SOGI blocks connected in parallel forming a dual SOGI-FLL (DSOGI-FLL) structure provides good transient response even in the presence of grid abnormalities (i.e. frequency variation, unbalanced voltages etc.). However, performance with distorted grid signals i.e. when harmonics are present is not satisfactory.

Apart from these disturbances, presence of dc component may also affect the performance of synchronization schemes. The probable source of dc component can be the measurement errors, conversion errors resulting through the data converters, inaccurate signal conditioning circuits, injection from DG due to their improper control, saturation of magnetic components etc. The performance of conventional PLLs, DSOGI-PLL, DSOGI-FLL is severely hampered in presence of the dc offset. The estimated frequency under such case is characterized by presence of low frequency component superimposed on the average value.

This aspect (frequency estimation in presence of the dc-offset) is not fully explored. To target this issue, few methods have been reported [19-24]. However, they are complex and suggested for single-phase system. Hence, in order to eliminate errors in frequency estimation caused due to presence of the dc offset and other grid abnormalities (e.g. unbalance, harmonics, frequency variation, magnitude variation etc.), a modified DSOGI-FLL (MDSOGI-FLL) for three-phase systems is proposed [25]. The modified SOGI-QSG structure used in the proposed MDSOGI-FLL employs the third integrator to estimate dc component and overcomes its effect in the estimation of frequency. The performance analysis of this structure has been carried out under presence of different grid voltage abnormalities and the superior performance is illustrated through simulation and experimental results. The details of the MDSOGI-FLL and its capability to perform under different conditions are highlighted in the remaining sections.

II. MODIFIED DSOGI-FLL

The section presents the basic configuration and reports the transfer functions of DSOGI-FLL [8] and proposed MDSOGI-FLL. In addition, the procedure for tuning of gain for both these FLL for estimating frequency under various grid abnormal conditions is also presented.

A. DSOGI-FLL: Structure and Transfer Functions

Fig. 1(a) shows structure of conventional DSOGI-FLL where the three-phase utility voltages (V_{as}, V_{bs}, and V_{cs}) under balanced condition are defined as

$$V_{abcs} = V_m \times \begin{pmatrix} \sin \omega t + \emptyset_a \\ \sin\left(\omega t - \frac{2\pi}{3}\right) + \emptyset_b \\ \sin\left(\omega t + \frac{2\pi}{3}\right) + \emptyset_c \end{pmatrix} \quad (1)$$

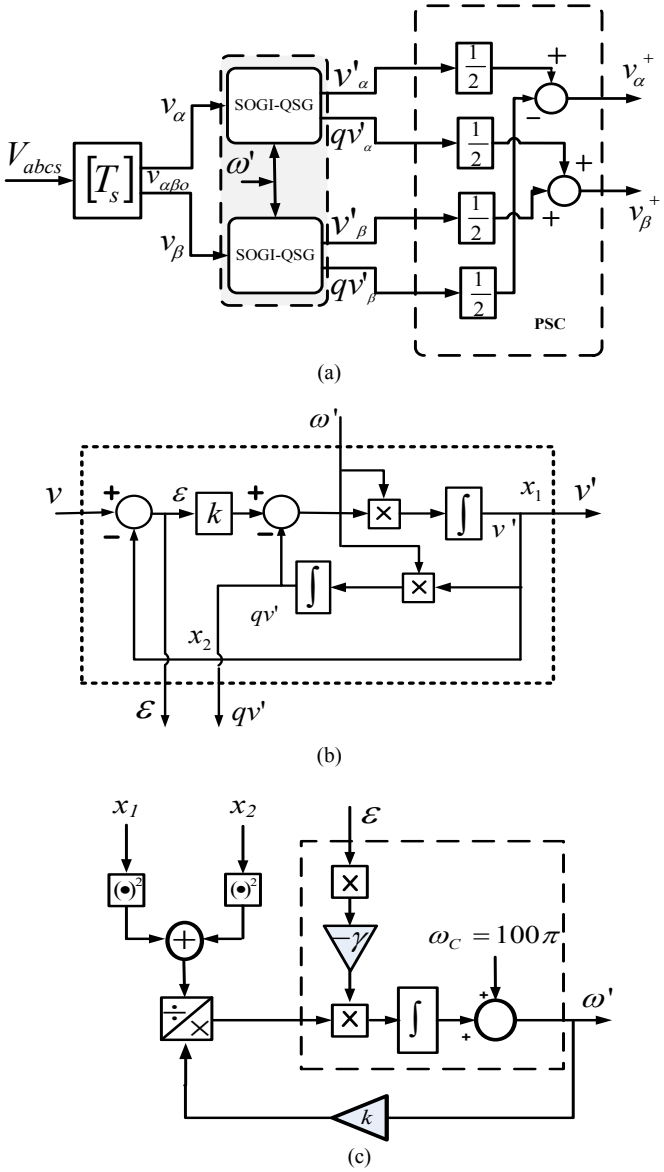

Fig. 1. Basic structure of DSOGI-FLL: (a) abc to $\alpha^+\beta^+$ computation(b) Standard SOGI-QSGs and (c) FLL-block.

$V_{abcs} = [V_{as} V_{bs} V_{cs}]^T$ and V_m, ω and $\emptyset$ are the amplitude, angular frequency and phase difference of the grid signal voltage, respectively. Under the assumption of the balanced utility voltages (1) can be represented in stationary reference frame by (2) as

$$v_{\alpha\beta 0} = [T_s] \times V_{abcs} \quad (2)$$

where $v_{\alpha\beta} = [v_\alpha, v_\beta]^T$ and $[T_s]$ denotes the Clarke transformation matrix represented by (3)

$$[T_s] = \frac{2}{3}\begin{bmatrix} 1 & -\frac{1}{2} & -\frac{1}{2} \\ 0 & \frac{\sqrt{3}}{2} & -\frac{\sqrt{3}}{2} \\ \frac{1}{\sqrt{2}} & \frac{1}{\sqrt{2}} & \frac{1}{\sqrt{2}} \end{bmatrix} \quad (3)$$

The Clarke or *αβ0* transform is a space vector transformation of time-domain signals from a natural three-phase coordinate system (*abc*) into a two-phase stationary reference frame αβ0. The proposed MDSOGI-FLL requires two in-quadrature components in a stationary reference frame, which are thus derived using Clarke transformation.

The shaded block showing two SOGI-QSG that represents dual second-order generalized integrators is the key part of PLL or FLL structure. The details of SOGI-QSG are shown in Fig. 1(b). The *v'* and *qv'* signals forms a pair of quadrature signals where *qv'* lags *v'* by 90º. These signals are used to extract positive sequence components through the Positive Sequence Calculator (PSC shown in Fig. 1(a)) in the *αβ* stationary reference frame. The positive sequence components v_α^+ and v_β^+ can be utilized to estimate the positive sequence (v_{abcs}^+) of the distorted grid input signal. Apart from filtering, SOGI-QSGs also work as voltage controlled oscillator [10] and thus the approach avoids extra voltage controlled oscillator unlike that in SRF based PLL. A simple auto tune block shown in Fig. 1(c) is used to adapt the center frequency ω' of the SOGI resonator to the input frequency. The frequency is estimated through the Frequency-Locked Loop (FLL) block adaptively by adjusting the gain (γ) in DSOGI-FLL and thus it discards the PLL block used in DSOGI-PLL. Hence, in the grid abnormalities like sag, swell, variations, phase jump, harmonics etc., the DSOGI-FLL performs extremely well, fast and precisely as compared to conventional SRF-PLL based schemes.

The transfer functions represented by (4) and (5) for band-pass filter (BPF) and low-pass filter (LPF), respectively, are obtained from the standard SOGI-QSGs shown in Fig.1 (b). They characterize the adaptive filtering structure of it. The bandwidth (or sharpness) of the band-pass filter *D(s)* and low-pass filter *Q(s)*, can be adjusted by proper tuning of the real positive value of gain *k*. Hence, the signals *v'* and *qv'* are the outputs of the BPF and LPF, respectively, with 90º phase shift between them. Actually, the LPF has a better filtering feature to the high frequencies than the BPF. But the *qv'* output of this standard SOGI-QSGs suffers from nonzero dc offset present in input grid voltage or the measured grid voltage. It is reflected in the calculation of positive sequence v_β^+ as shown in Fig. 2, which shows the response of v_α^+ and v_β^+ when sudden frequency change and dc offset are introduced. This leads to inaccurate estimation of fundamental positive sequence components and frequency.

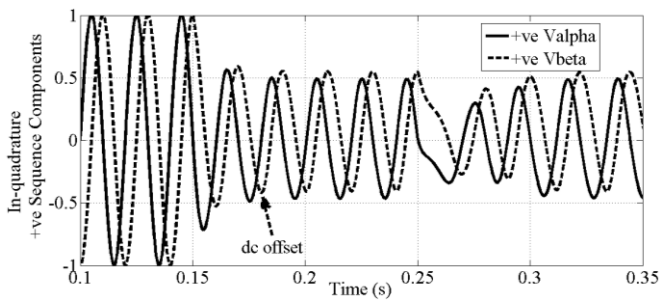

Fig. 2. Output waveform of in-quadrature (v_α^+andv_β^+) positive sequence components in presence of dc offset and frequency jump in the sensed input signal of standard SOGI-QSGs.

$$D(s) = \frac{v'}{v}(s) = \frac{k\omega' s}{s^2 + k\omega' s + \omega'^2} \tag{4}$$

$$Q(s) = \frac{qv'}{v}(s) = \frac{k\omega'^2}{s^2 + k\omega' s + \omega'^2} \tag{5}$$

B. MDSOGI-FLL: Structure and Transfer Functions

It is worth noting from the above section that the conventional DSOGI-FLL fails to estimate the frequency accurately when sensed grid signals are characterized by the dc offset. The proposed MDSOGI-FLL structure is similar to that of DSOGI-FLL shown in Fig.1 (a) except the fact that the SOGI-QSGs (Fig. 1(b)) are now replaced by the modified SOGI-QSGs shown in Fig. 3.

The modified SOGI-QSGs of Fig. 3 can be described by the following transfer functions (6), (7) and (8).

$$D'(s) = \frac{v'(s)}{v(s)} = \frac{k_1\omega' s^2}{\Delta(s)} \tag{6}$$

$$Q'(s) = \frac{qv'(s)}{v(s)} = \frac{k_1\omega'^2 s}{\Delta(s)} \tag{7}$$

$$V_{dc}(s) = \frac{v_{dc}(s)}{v(s)} = \frac{k_{dc}\omega'(s^2 + \omega'^2)}{\Delta(s)} \tag{8}$$

where

$$\Delta(s) = s^3 + (k_1 + k_{dc})\omega' s^2 + \omega'^2 s + k_{dc}\omega'^3 \tag{9}$$

It is depicted from (6) and (7) that $D'(s)$ and $Q'(s)$ both have a band pass filtering characteristic and results into the rejection of offset in the in-quadrature components. However, proper tuning of gain parameters k_1 and k_{dc} is necessary for it.

C. Gain Tuning of SOGI-QSG and Proposed Structure

The sub-section presents the analysis for determination of the parameters involved in the LPF and BPF transfer functions of DSOGI-FLL and MDSOGI-FLL.

i. Tuning of Standard SOGI-QSG

From (4), the characteristic equation $s^2 + k\omega' s + \omega'^2 = 0$ is

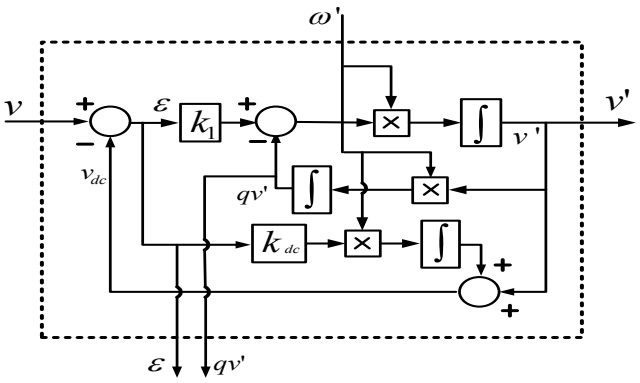

Fig. 3 Block diagram of Modified SOGI-QSG block

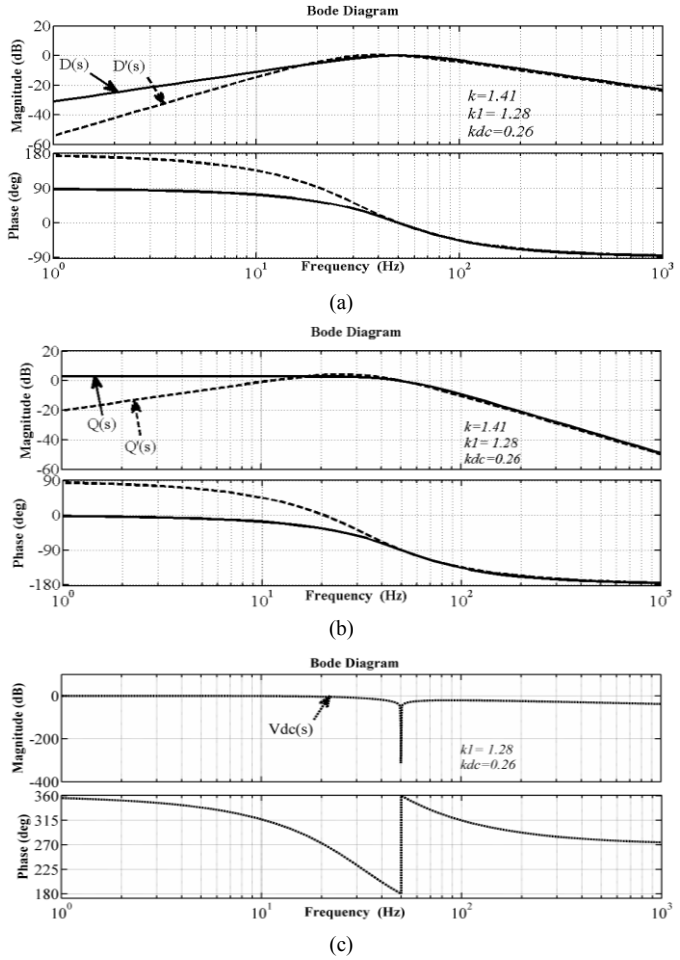

Fig. 4. Comparison of the frequency response for the transfer function (a) *D(s)* and$D^{'}(s)$(b) *Q(s)* and $Q'(s)$ (c) $V_{dc}(s)$.

compared with the standard characteristic equation $s^2 + 2\zeta\omega_n s + \omega_n^2 = 0$ to obtain the gain k at the damping ratio ζ =0.707 (underdamped system) and natural frequency of oscillation ω_n= 2π50 rad/s. The gain k is given by (10).

$$k = \frac{9.2}{t_s \omega'} \tag{10}$$

$$\text{where settling time} t_s = 4.6 \times \tau\,; \tau = \frac{1}{\zeta\omega_n} \tag{11}$$

It is essential to have a proper tuning of the gain k to have appropriate bandwidth to discard the low frequency and higher frequency components present in the input signals. Figs. 4(a) (b) and (c) show bode plots for *D(s)*, *Q(s)* and $V_{dc}(s)$ (represented by (8)), obtained using (10)-(11), for k = 1.41 and ζ = 0.707. It is evident from these plots that *D(s)* attenuates the low frequency components unlike *Q(s)* and hence, the dc offset is not eliminated inv_β^+.

ii. Tuning of Proposed Modified SOGI-QSG

The parameters k_1 and k_{dc} shown in Fig.3 are selected based on the roots of the $\Delta(s)$ assuming that all the roots have equal real parts (all three poles have equal natural frequency of oscillation). These parameters are obtained by comparing the $\Delta(s)$ represented by (9) with (12).

$$(s + \omega_{n_1})(s^2 + 2\zeta\omega_{n_2}s + \omega_{n_2}^2)=0 \tag{12}$$

To estimate the gain k_1 and k_{dc}, $\omega_{n_1} = \omega_{n_2}$= 2π50 rad/s and ζ = 0.707 (same as that considered for tuning DSOGI- FLL) is considered. The effect of both the gain adjustment is clearly indicated in the bode diagrams of Fig. 4. It is observed from Figs. 4(a) and (b) that for low frequencies, magnitude bode plots of *D'(s)* and *Q'(s)* lie below 0dB, indicating attenuation of low frequency components and dc component. The magnitude plots of *D(s)* and *Q(s)* are also shown in Figs. 4(a) and (b) to compare the performance of DSOGI-FLL and MDSOGI-FLL. It is evident that as gain *Q(s)* is positive, it does not attenuate dc component. Fig. 4(c) shows bode plot for (8) that represents the performance of third generalized integrator. The magnitude of transfer function V_{dc}(s) is nearly 0dB till 50Hz indicating no effect on the computation of the low frequency components. However, sudden decrease in the magnitude (large negative magnitude) is observed at 50Hz, which indicates the attenuation of 50Hz (fundamental) component. The attenuation of higher order harmonics also occurs as negative gain is observed for $V_{dc}(s)$ at frequencies higher than 50Hz. However, it is much lower than that at 50Hz. Thus, the inclusion of third integrator results into large attenuation of fundamental component (also higher order frequencies to a certain extent) allowing only the low order frequencies to pass. Thus, it helps to estimate and eliminate the dc offset accurately from input *v* of Fig. 3.

III. Simulation Results

The effectiveness of the proposed MDSOGI-FLL is demonstrated through the simulation results obtained in MATLAB/Simulink. The parameter values used in the modified DSOGI-FLL simulation model are as follows: k_1=1.28, k_{dc}=0.26 and γ=40. The performance is evaluated for three cases: (i) balanced sag, (ii) imbalance in three-phase supply voltage, and (iii) presence of harmonics. In all the cases it is considered that the dc offset is present due to the measurement or data conversion errors.

Fig. 5(a) presents the case (i) where a step change in amplitude of the grid signal is observed at t=0.15s, where the amplitude decreases from 1per unit (pu) to 0.5pu. Also the dc offset of 0.1pu is introduced at t=0.15s. In addition, at t=0.25s frequency of grid signal suddenly changes from 50Hz (314rad/s) to 45Hz (282.6rad/s).

Fig. 5(b) shows that both v_α^+ and v_β^+ for MDSOGI-FLL are free from offset, unlike that observed for DSOGI-FLL in (Fig. 2). The reason being the band-pass filtering capabilities of $D'(s)$ and $Q'(s)$, unlike DSOGI-FLL where *D(s)* behaves as BPF while *Q(s)* behaves as LPF. It is observed from Fig. 5(c), that the DSOGI-FLL is able to track the frequency accurately only till t=0.15s, and then exhibits oscillatory nature. Also the large dip in the estimated frequency is observed at t=0.25s. Unlike the DSOGI-FLL, the MDSOGI-FLL does not show oscillations and estimated frequency quickly settles down to the final value. The dips at the instant of step changes in

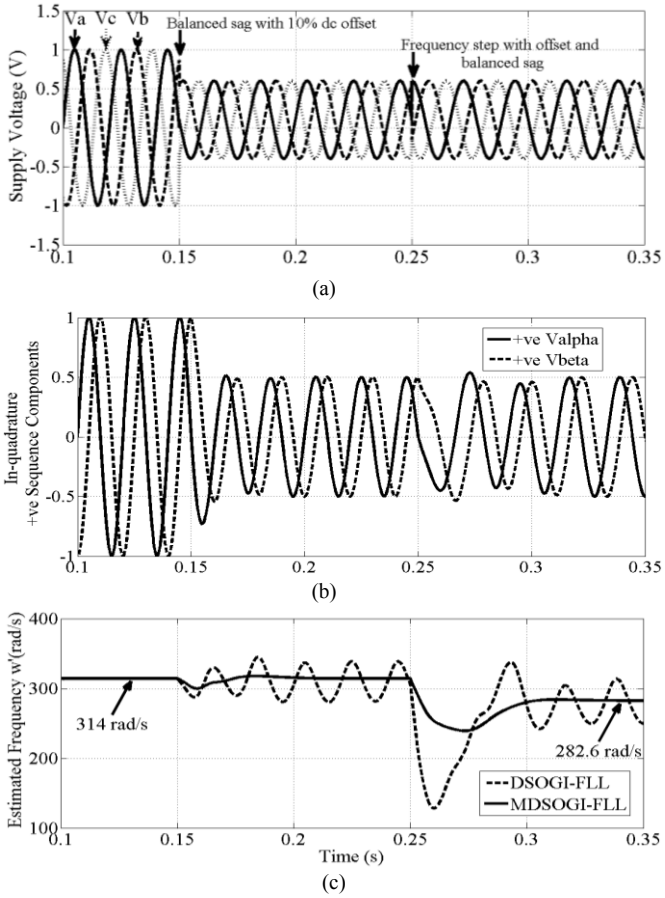

Fig. 5. Performance under balanced sag conditions: (a) Three-phase grid voltage signals (b)in-quadrature (v_α^+andv_β^+) positive sequence components (c) Estimated frequency.

amplitude of grid voltage and frequency change are also much less than that observed with MDSOGI-FLL.

Unlike case (i), for the case (ii) shown in Fig. 6, step change in amplitude of the grid signal is considered only for phase 'a'. At t=0.15s, the amplitude of phase 'a' voltage decreases from 1pu to 0.5pu. All other changes are similar to that in case (i).The ripple in the estimated frequency of DSOGI-FLL is less than the earlier case. However, the nature is similar to that observed in case (i). The MDSOGI-FLL once again shows superior performance. Fig. 7(a) shows the grid voltage characterized by the presence of 5^{th}, 7^{th}, 11^{th}, and 13^{th} harmonics alongwith the dc offset of 0.1pu after t=0.15s.The step change in frequency is applied at t=0.25s as in case (i)and case (ii). Fig. 7(b) displays oscillations in the estimated frequency of DSOGI-FLL, while the proposed MDSOGI-FLL eliminates the oscillation caused by the dc offset. As a result, the grid signal frequency is quickly and accurately tracked.

Fig. 8 shows the comparison of different frequency estimation techniques when subjected to a step change in the supply frequency. The supply voltage is considered to have the harmonics, unbalance and the dc-offset. The comparison is carried out for $\omega_n = 2\pi 50$ rad/s, $\zeta = 0.707$ to have the settling time of 40ms. Table I shows the settling time for these frequency estimation techniques in -PLL are relatively faster than other techniques. It must response to a step change in the frequency at t=0.25s. SRF-PLL and MDSOGI be noted that

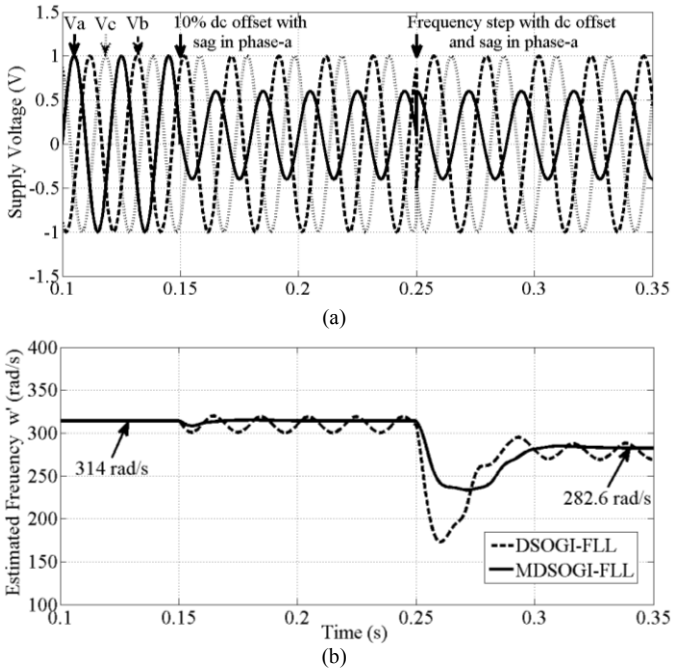

Fig. 6. Performance under unbalanced sag conditions: (a) Three-phase grid voltage signals (b) Estimated frequency.

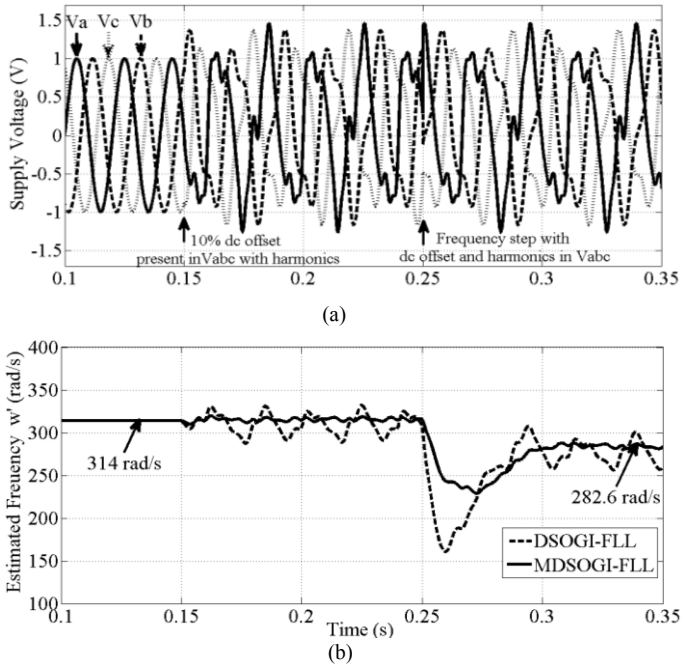

Fig. 7. Performance when harmonics are present: (a) Three-phase grid voltage signals (b) Estimated frequency with DSOGI-FLL and MDSOGI-FLL.

except MDSOGI-FLL all other techniques show sustained oscillations in the estimated frequency. Hence, the settling time for these techniques is determined as the time from the step change till the estimated frequency waveform reaches a stage where sustained oscillations with a constant average (dc) value is achieved. The qualitative comparison of these frequency estimation techniques is also provided in Table II to show their capabilities of detecting and rejecting the effect of harmonics, unbalance and dc-offset in the frequency estimation. The proposed MDSOGI-PLL performs well on all

the aspect even when the dc-offset is present. Thus, it is not only fast but also accurate under all grid abnormalities.

TABLE I
TIME RESPONSE FOR DIFFERENT FREQUENCY ESTIMATION TECHNIQUES

PLL-Type	Estimated Time (ms)	Observed Time (ms)
SRF-PLL	40	50
DDSRF-PLL	40	70
DSOGI-PLL	40	45
DSOGI-FLL	40	60
MDSOGI-FLL	40	50

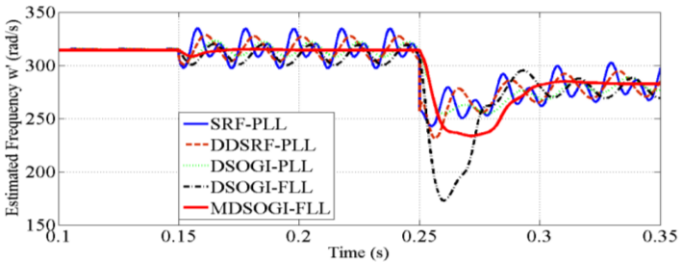

Fig. 8. Comparison of performance of various frequency estimation methods.

TABLE II
PERFORMANCE EVALUATION OF DIFFERENT PLL TECHNIQUES

PLL-Type	Detection of Negative Sequence Components	Harmonic Detection	DC offset Rejection
SRF-PLL	No	No	No
DDSRF-PLL	Yes	Requires more decoupling term	No
DSOGI-PLL	Yes	Yes	No
DSOGI-FLL	Yes	Yes	No
MDSOGI-FLL	Yes	Yes	Yes

IV. EXPERIMENTAL RESULTS

The experimental results are included in this section to validate the effectiveness of the proposed MDSOGI-FLL. The cases considered for simulation are verified experimentally using DSpace DS1104 DSP board as control system. The values of various parameters for which the MDSOGI-FLL is tuned are k_1= 1.28 k_{dc} = 0.26 and γ=40, while those for DSOGI-FLL are k = 1.41 and γ=100. The fundamental frequency of the three phase supply voltage and the sampling frequency are 50Hz and 10kHz, respectively. Thus, the same parameters that are considered for simulation through MATLAB/Simulink are adopted for experimental verification.

Fig.9 shows the three-phase supply voltage along with the frequency estimated by MDSOGI-FLL. The supply, shown in Fig. 9(a) is initially balanced with 50Hz and then undergoes the disturbances similar to that shown in Fig. 5(a). Thus, the balanced sag of 50% and even a frequency step change of 10% (frequency change from 50Hz to 45Hz) is applied in the supply voltage. The dc-offset of 10% is superimposed on the supply voltage. The supply frequency estimated by both proposed MDSOGI-FLL and the conventional DSOGI-FLL are shown in Fig.9 (b). Just like simulation results, the experimental results also depict oscillations in the frequency estimated by the DSOGI-FLL, while MDSOGI-FLL is free from oscillations and is able to correctly estimate the frequency. The difference 'ΔV' , marked by the difference in the position of the two cursors in Fig.9(b), indicates the frequency change of 32 rad/s corresponding to change of 5Hz (2 x 3.14 x 5 = 31.4 rad/s) when a step change of frequency from 50Hz to 45Hz (and vice-versa) is applied. The minor variation in the magnitude is due to the limitation of the oscilloscope's resolution. It is clearly evident even from the experimental results that the effect of offset present in supply voltage is very effectively eliminated in the proposed scheme.

Fig. 10 shows the comparison of the proposed MDSOGI-FLL structure against the conventional DSOGI-FLL under the conditions similar to that shown in Fig. 6(a). Voltage sag of 50% is introduced in just one of the phases while the dc offset is present in all the three phases. The three-phase unbalanced voltage signals with above characteristics, used to study the performance of DSOGI-FLL and MDSOGI-FLL, are shown in Fig. 10(a). Fig. 10(b) represents the comparison of the estimated frequency by both these methods. Frequency obtained through DSOGI-FLL approach once again shows that

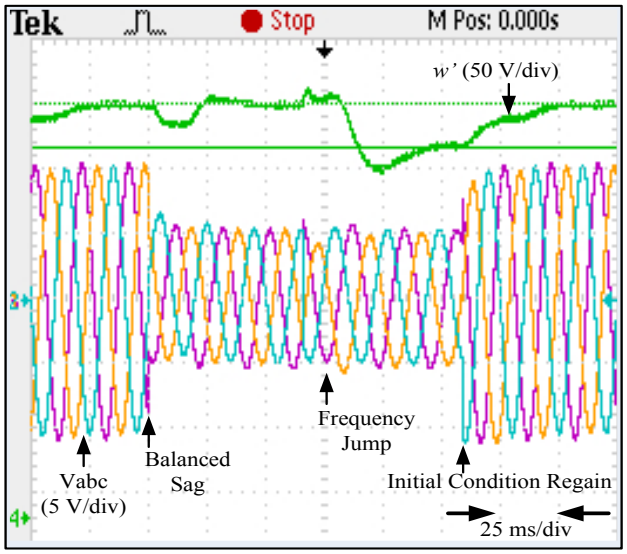

(a)

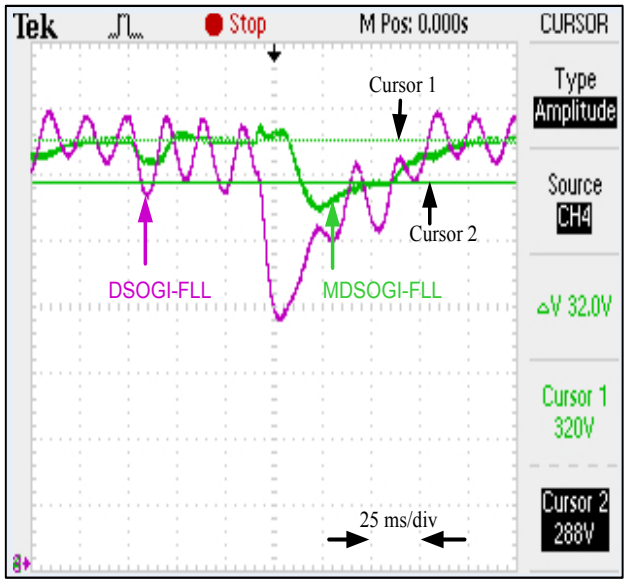

(b)

Fig. 9. Experimental results with balanced-sag and dc-offset in supply voltage: (a) Three-phase supply voltage signals (b) Estimated frequency with DSOGI-FLL and MDSOGI-FLL.

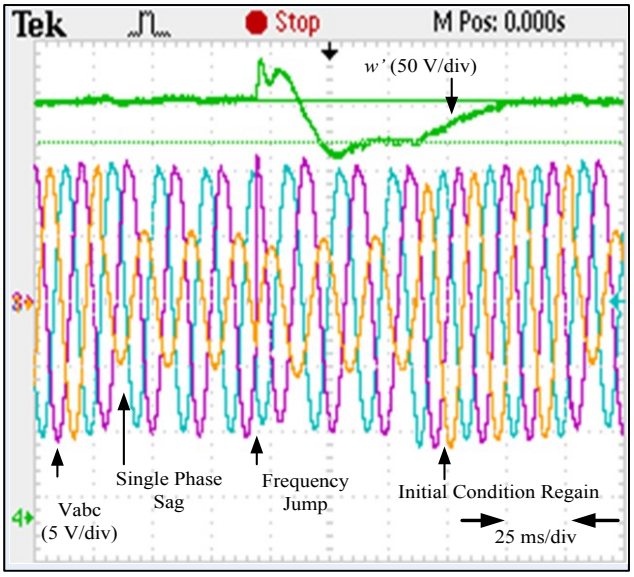

(a)

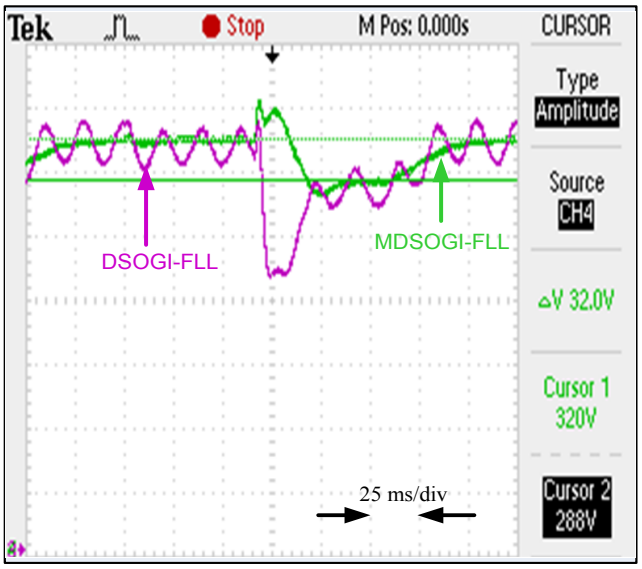

(b)

Fig. 10. Experimental results with imbalance and dc-offset in supply voltage: (a) Three-phase grid voltage (b) Estimated frequency with DSOGI-FLL and MDSOGI-FLL.

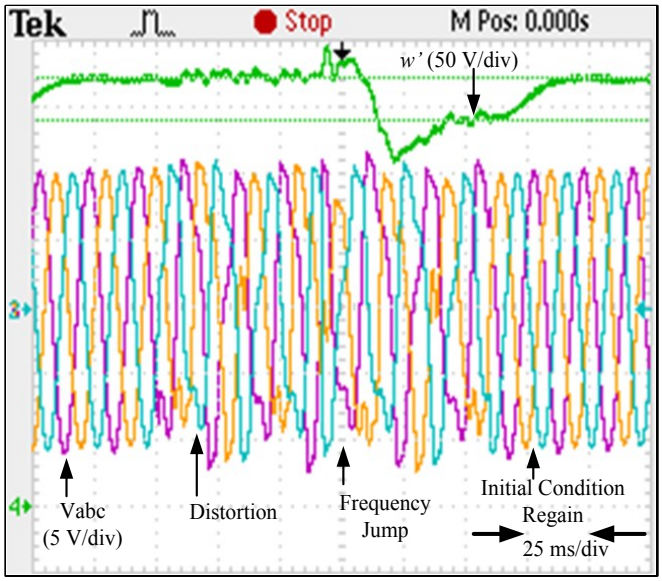

(a)

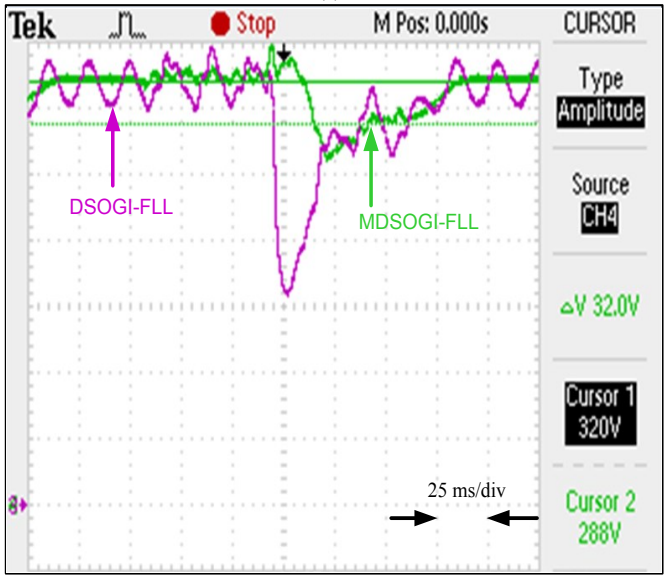

(b)

Fig. 11. Experimental results with dc offset and harmonics in supply voltage: (a) Three-phase supply voltage (b) Estimated frequency with DSOGI-FLL and MDSOGI-FLL.

the estimated frequency is characterized by an oscillatory response, with a 100Hz frequency ripple. Frequency estimated by MDSOGI-FLL not only is free from oscillations, but also has lower frequency dip corresponding to sudden frequency decrease. Thus, the overshoot with the step response with MDSOGI-FLL is less indicating a better transient response.

The immunity of the proposed scheme to the highly distorted signal is demonstrated through the experimental results shown in Fig. 11. As in Fig.7(a), the three-phase grid voltage signal shown in Fig. 11(a) is characterized by presence of 5^{th}, 7^{th}, 11^{th} and 13^{th} order harmonic components with amplitudes of 30%, 10%, 8% and 7% , respectively, with respect to the fundamental. Also, a frequency jump of 50Hz to 45Hz is introduced similar to that shown in Fig. 7(a). Both these variation in supply voltages are considered along with the presence of dc offset 10%. Fig. 11(b) shows that the estimated frequency of DSOGI-FLL not only has the 100Hz frequency component, but also shows the harmonic distortion due to the effect of harmonics present in the supply voltage. Unlike it, the estimated frequency of MDSOGI-FLL is once again free from the effect of dc offset and exhibits a superior performance with a very little deviation from the average value. The negligible high frequency ripple is due to the harmonics in the supply voltage.

The proposed technique works equally well even in case when the input voltage is characterized by multiple abnormalities. To illustrate the performance of the MDSOGI-FLL under such multiple abnormalities, a supply voltage having harmonics, voltage sag and dc-offset all together, is considered. Fig. 12(a) shows the input voltage signal, which is characterized by the presence of the 5^{th} , 7^{th}, 11^{th} and 13^{th} order harmonic components with the amplitudes of 30%, 10%, 8%

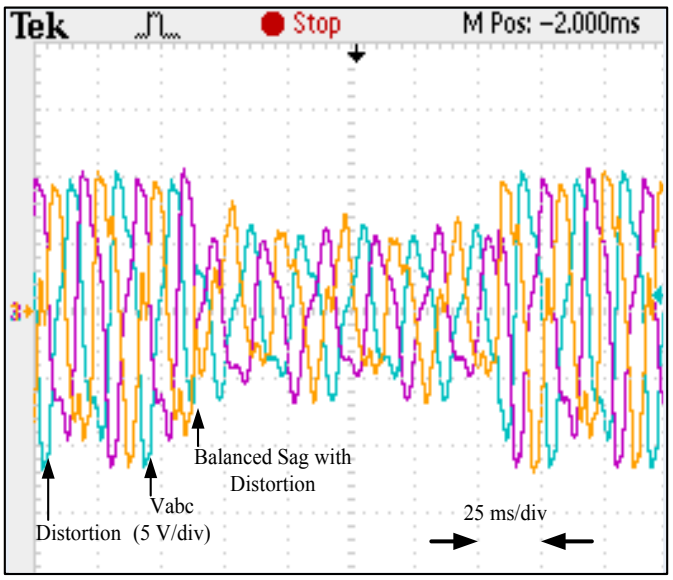

(a)

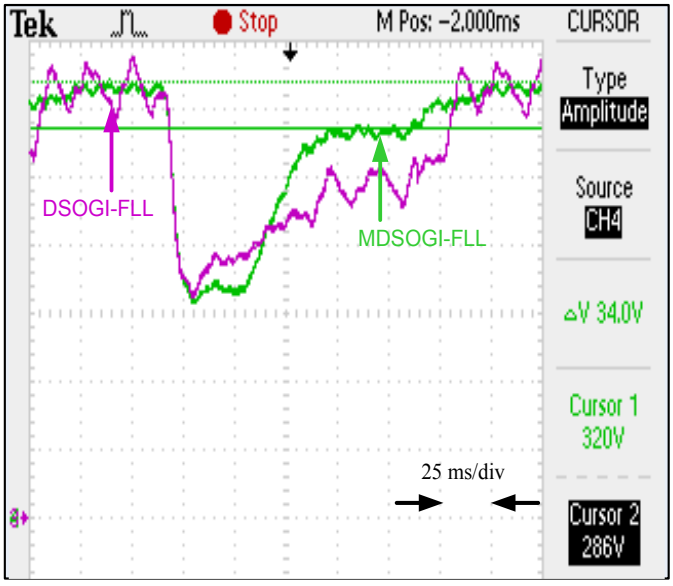

(b)

Fig. 12. Experimental results with input voltage characterized simultaneously by dc offset, harmonics and voltage sag: (a) Three-phase supply voltage (b) Estimated frequency with DSOGI-FLL and MDSOGI-FLL.

and 7% (with respect to fundamental component), respectively along-with the 10 % of dc offset error. Further a step change (decrease/sag) of 50% is applied in magnitude of supply voltage. Fig. 12 (b) highlights the performance of the proposed MDSOGI-FLL in estimating the grid voltage signal frequency and once again MDSOGI-FLL is found to be superior over DSOGI-FLL. With MDSOGI-FLL, the estimated frequency is not only estimated quickly but is also free from oscillatory nature, unlike that with the DSOGI-FLL technique.

V. Conclusion

DSOGI-FLL can accurately estimate the frequency of the grid signal under various abnormal conditions except the presence of dc offset. The presence of dc offset in grid voltage introduces a ripple of 100Hz low frequency component in the estimated frequency. This 100Hz ripple is further having the distortion when harmonics are present. This error in the estimation of frequency may affect the synchronization and control of DG based inverter.

The proposed MDSOGI-FLL structure, which consists of the three fundamental blocks: 1) basic SOGI-building block with third integrator; 2) FLL block to estimate the frequency adaptively and 3) PSC block to calculate the positive sequence components; eliminates the ripple present in the estimated synchronized frequency. In MDSOGI-FLL, the third integrator added to the standard SOGI-QSG structure attenuates the dc offset. As a result, in addition to the benefits of the conventional DSOGI-FLL, the proposed method exhibits the capability of rejecting dc offset and hence, can accurately track the frequency of fundamental component of grid-voltage effectively under all grid abnormalities. Simulation and experimental results justify that the proposed MDOSGI-FLL is accurate and shows better transient response than that of DSOGI-FLL.

References

[1] F. Blaabjerg, Zhe Chen, and S. Baekhoej Kjaer, "Power electronics as efficient interface in dispersed power generation systems, " *IEEE Trans. on Power Electron.*, vol. 19, no. 5, pp. 1184-1194, September 2004.

[2] F. Blaabjerg, Remus Teodorescu, Marco Liserre, and Adrian V. Timbus, " Overview of control and grid synchronization for distributed power generation systems", *IEEE Trans. on Ind. Electron.*, vol. 53, no. 5, pp. 1398-1409, October 2006.

[3] Se-Kyo Chung, "A phase tracking system for three phase utility interface inverters," *IEEE Trans. Power Electron.* , vol. 15, no. 3, pp. 431-438, May 2000.

[4] Benjamin Kroposki, Christopher Pink, Richard DeBlasio, Marcelo Simoes, Holly Thomas and Pankaj K. Sen "Benefits of power electronic interfaces for distributed energy systems," *IEEE Trans. on Energy Conv.*, vol. 25, no. 3, pp. September 2010.

[5] Maohai Wang and Yuanzhang Sun, "A practical method to improve phasor and power measurement accuracy of DFT algorithm," in *IEEE Trans. on Power Del.*, vol. 21, no. 3, pp. 1054-1062, July 2006.

[6] H. A. Darwish and M. Fikri, "Practical considerations for recursive DFT implementation in numerical relays," in *IEEE Trans. on Power Del.*, vol. 22, no. 1, pp. 42-49, Jan 2007.

[7] H. Wen, Z. Teng, Y. Wang and X. Hu, "Spectral correction approach based on desirable sidelobe window for harmonic analysis of industrial power system," in *IEEE Trans. on Ind. Electron.*, vol. 60, no. 3, pp. 1001-1010, March 2013.

[8] R. Teodorescu, M. Liserre and P. Rodriguez, "A thesis on grid converters for photovoltaic and wind power systems," 2011, ISBN: 978-0-470-05751-3.

[9] Md. Shamim Reza, Mihai Ciobotaru and V. G. Agelidis, "Accurate estimation of single-phase grid voltage parameters under distorted conditions," *IEEE Trans. Power Del.* vol. 29, no. 3, pp. 1138-1146, June-2014.

[10] Fengjiang Wu, Lujie Zhang, and Jiandong Duan, "A new two-phase stationary-frame-based enhanced PLL for three-phase grid synchronization," *IEEE Trans. Circuits Syst. II,* Express Briefs, vol. 62, no. 3, March 2015.

[11] Y. Han, M. Luo, X. Zhao, J. M. Guerrero and L. Xu, "Comparative performance evaluation of orthogonal-signal-generators-based single-phase PLL algorithms—A survey," in *IEEE Trans. on Power Electron.*, vol. 31, no. 5, pp. 3932-3944, May 2016.

[12] V. Kaura and V. Blasco, "Operation of a phase locked loop system under distorted utility conditions," *IEEE Trans. Ind. Appl.*, vol. 33, no.1, pp. 58–63, Jan 1997.

[13] P. Rodriguez, J. Pou, J. Bergas, J. I. Candela, R. P. Burgos and D. Boroyevich, "Decoupled double synchronous reference frame PLL for power converters control," in *IEEE Trans. on Power Electron.*, vol. 22, no. 3, pp. 1078-1078, May 2007.

[14] P. Rodriguez, A. Luna, I. Candela, R. Teodorescu, and F. Blaabjerg, "Grid synchronization of power converters using multiple second-order generalized integrators," in *Proc. 34th Annu. Conf. IEEE Ind. Electron*., pp. 755–760, November 2008.

[15] P. Rodrıguez, A. Luna, R. Santiago M. Aguilar, I. E. Otadui, R. Teodorescu, and F. Blaabjerg, "A stationary reference frame grid synchronization system for three-phase grid-connected power converters under adverse grid conditions," *IEEE Trans. Power Electron*., vol. 27, no. 1, pp. 99-112, January 2012.

[16] Saeed Golestan, Malek Ramezani, Josep. M. Guerrer, and Mohammad Monfared, *"dq*-Frame Cascaded Delayed Signal Cancellation- Based PLL: Analysis, Design, and Comparison With Moving Average Filter-Based PLL," *IEEE Trans. Power Electron.*, vol. 30, no. 3, pp. 1618-1631, March 2015.

[17] Md. Shamim Reza, Mihai Ciobotaru, and V. G. Agelidis, "Power system frequency estimation by using a Newton-type technique for smart meters," *IEEE Trans. Instrum. Meas.*, vol. 64, no. 3, pp. 615–624, March -2015.

[18] J. Matas, M. Castilla, J. Miret, L. Garcia de Vicuna, and R. Guzman, "An adaptive prefiltering method to improve the speed/accuracy tradeoff of voltage sequence detection methods under adverse grid conditions," *IEEE Trans. on Ind. Electron.*, vol. 61, no. 5, pp. 2139-2151, May-2014.

[19] M. Ciobotaru, R. Teodorescu and V. G. Agelidis, "Offset rejection for PLL based synchronization in grid-connected converters," *Proc. 23rd Annu. IEEE Appl. Power Energy Conf. Expo.*, pp. 1611–1617, February-2008.

[20] M. Karimi Ghartemani, S. Khajehoddin, P. Jain, and A. Bakhshai. "Comparison of two methods for addressing dc component in phase-locked loop (PLL) systems," in *Proc. IEEE ECCE*, pp. 3053-3058, September 2011.

[21] M. Karimi-Ghartemani, S. Khajehoddin, P. Jain, A. Bakhshai and M. Mojiri, "Addressing dc component in PLL and notch filter algorithms," *IEEE Trans. Power Electron*. , vol. 27, no. 1, pp. 78-86 January 2012.

[22] S. Hwang, L. Liu, H. Li, and J. M. Kim, "DC offset error compensation for synchronous reference frame PLL in single-phase grid-connected converters," *IEEE Trans. Power Electron*. , vol. 27, no. 8, pp. 3467-3471, August 2012.

[23] Fengjiang Wu, Dongyang Sun, Lujie Zhang and Jiandong Duan, "Influence of plugging DC offset estimation integrator in single-phase EPLL and alternative scheme to eliminate effect of input DC offset and harmonics," *IEEE Trans. on Ind. Electron.*, vol. 62, no. 8, pp. 4823-4831, May-2014.

[24] S. Golestan, Josep M. Guerrero and G.B. Gharehpetian, "Five approaches to deal with problem of DC offset in phase-locked loop algorithm: Design consideration and performance evaluation," *IEEE Trans. Power Electron*. , vol. 31, no. 1, pp. 648-661, January 2016.

[25] K. R. Patil and Hiren H. Patel, "Modified dual second-order generalised integrator FLL for synchronization of a distributed generator to a weak grid," in *Proc. 16th Annu. Conf. IEEE-EEEIC,* June 2016.

Kalpeshkumar Patil received the B.E. degree in electrical engineering from the Shri S.V. Mandal Institute of Technology, South Gujarat University, Surat, India, in 2003, and the M.Tech. degree in electrical engineering systems in 2009 from the S.V. National Institute of Technology, Surat, India.

He is currently working as an Assistant Professor in Department of Electrical Engineering at Sarvajanik College of Engineering & Technology, Surat and pursuing the part time Ph.D. degree course in electrical engineering affiliated to Gujarat Technological University, Ahmedabad, Gujarat, India. His current research interests include grid synchronization, active power filtering, power quality issues.

Hiren Patel received the B.E. degree in electrical engineering from the S.V. Regional College of Engineering and Technology (now S.V. National Institute of Technology), South Gujarat University, Surat, India, in 1996, and the M.Tech. degree in energy systems in 2003 from the Indian Institute of Technology—Bombay (IITB),Mumbai, India. He has received his Ph. D. degree from the Indian Institute of Technology. He is working as a Professor at Sarvajanik College of Engineering and Technology, Surat.

His current research interests include computer aided simulation techniques, distributed generation, and renewable energy, especially energy extraction from photovoltaic arrays. Mr. Patel is a Life Member of the Indian Society for Technical Education.

Multi-source energy networks for cargo Vessels

Sanjana Ahmed, Alberto Castellazzi, Arthur Williams
Electrical and Electronic Engineering
University of Nottingham
Nottingham, UK
Eexsa70@nottingham.ac.uk

***Abstract*— The paper discusses the feasibility of installing renewable energy generation technologies on sea-going transport, taking into account the additional weight and power consumption. This study in based on the power management of a 26,198 tonne commercial chemical tanker. The management system would aim at reducing the number of generators as well as the power required from burning fossil fuels. After a process of elimination of potential technologies based on feasibility of the project and shipboard application, the work is focused towards photovoltaic and wind energy generation in combination with fossil fueled engines and Li-ion battery storage covering the higher energy density needs, and the intermittent nature of renewables. The network architecture is optimized in order to have the highest efficiency, and reduced system weight. The results show that successful management of the system can lead to reduction in generator requirement, and energy despite the weight of extra installations of photovoltaic and wind energy generation systems. By reducing the number of generators and allowing each remaining one to operate near their maximum power, the specific fuel consumption is improved, the efficiency is increased, resulting in significant fuel and cost saving, along with the mass of fuel to be carried on-board.**

Keywords—ship, energy management, renewable energy, solar, marine, storage

I. INTRODUCTION

With an annual growth of 3.3% in world fleet, the international shipping industry contributes 3% to global Green House Gas (GHG) emissions, and a staggering 85% of global demand for transport [1]. Measures are therefore being taken to reduce emissions such as CO_2, NO_X, and SO_X etc. (MARPOL Annex VI), which defines specific limits per g/kWh for all diesel engine types. The current total fuel oil consumption by ships amount to an excess of 350 million tonnes per annum, with the cost taking up to 50-60% of total operating cost of individual ships [2]. With newer regulations on emission from marine transport coming into effect in certain parts of the world, the feasibility of harvesting renewable energy on-board marine vessels need to be carefully considered. Due to the portable nature of the application, the additional weight penalty of renewable system installation, and thereby the extra energy expended, needs to be carefully studied and work is to be done in order to cover the gap between generation/storage technologies applied on-shore, against those that are suitable for portability and operate off-shore. This study will investigate the feasibility of powering the ship auxiliary systems of a commercial tanker whose specifications are given in Table 1 [3]. The auxiliaries may include pumps, blowers, coolers, compressors, vent fans, boilers, thrusters, hotel loads etc. A range of renewable energy technologies including wind and solar energy is considered to assess their suitability for maritime applications. Harvesting energy from motion of the vessel due to wave energy has been considered but the power generated is deemed too small, from the mechanical devices that have been tested [4], and there has been no optimal technology for converting the kinetic energy from ship motions to electric energy yet. The intermittency of renewable energy sources, and their variability due to voyage routes, demands that multiple inter-dependent sources be employed as ship powering options. Calculations are made on solar and wind power profiles for representative days and locations, to be compared with the vessel's power profile. The results are used to find the best possible mix of energy storage and generation, with an aim to keep the cost and weight at a minimum. The unpredictable nature of energy generation from renewable sources calls for its combined operation with Energy Storage Systems (ESS) in order to optimally manage power from each unit. With the load demand, from e.g. maneuvering systems, auxiliary machinery, air conditioning etc. of tankers being more or less constant, spikes of instantaneous power demands are rare, and therefore the high energy density, slow discharging batteries will be considered for the system, with supercapacitor being a good supplement for transients.

In the rest of the paper, section II describes the different energy generation methods employed onboard the vessel supplementary to its existing diesel engines, and possible architectures of integrating them into the ship grid. Section III outlines the sizing of and energy capacities of each of the installed energy sources and storage systems based on the space constraints of the vessel. Section IV calculates the extra weight related consumption of the installed system and comments on its feasibility. Section V outlines the management of the overall

TABLE 1: PHYSICAL AND ELECTRICAL SPECIFICATIONS OF TANKER

Length(m) x Breadth (m)		159.03 x 27.1	
Maximum Auxiliary Demand (kW)		1453	
Generator	No.	Prime Mover (kW)	Output (kW)
Main Generator	3	660	600

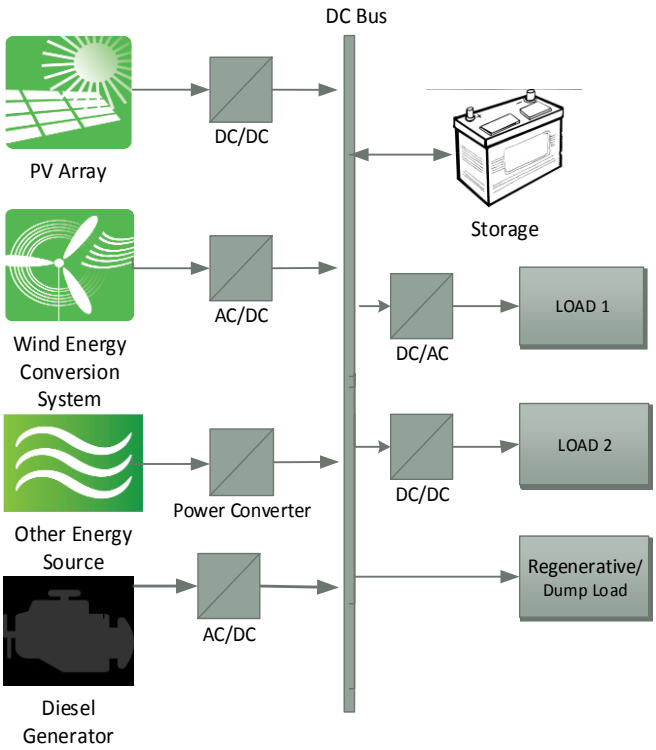

Figure 1a: Block diagram of potential multi-source renewable energy ship powering network with DC grid

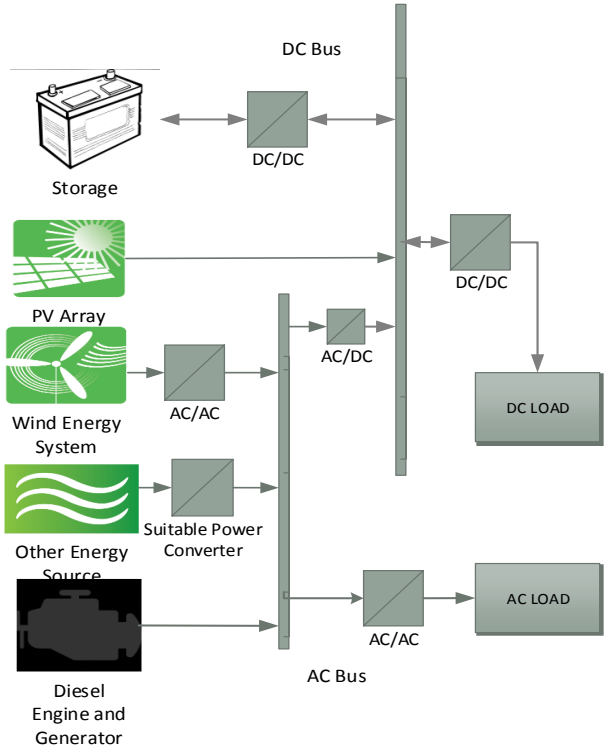

Figure 1b: Block diagram of alternative potential multi-source renewable energy ship powering network with parallel AC and DC grid

system along with a control strategy to finally tie all the generation and storage devices in an effective arrangement.

II. Energy Generation Methods

According to an amended report by DNV for Shipping 2020 [5], the uptake of hybrid systems in ship powering has been more rapid with batteries being placed in conjunction with fossil fueled engines resulting into a complex and efficient system of fuel mixture. The on-board integration of Distributed Generation (DG) such as PV systems, storage devices, and modern electronic loads, which are inherently DC, and the recent innovations in power electronics have created a drive towards replacing the traditional AC grid of commercial ships with their DC counterparts. The aim is to achieve higher efficiency through the reduction of conversion stages in incorporating the grid with DC sources and devices, lower emissions due to the higher efficiency system, attain more flexibility due to absence of AC switchboard and hence space utilization, and reduce weight, although with added complexity. Fig. 1 shows two alternative proposals for electrical power system architecture for the ship in relation to the energy storage system, as opposed to the conventional AC distribution. Fig. 1(a) contains a 1000 V DC bus, which can be stepped down to lower voltages. It is suitable for avoiding reactive power in high power levels and operating prime movers at optimal speed without the need for synchronization based on bus frequency, resulting in fuel savings. The need for bulky transformers are eliminated. Further space and weight saving due to the flexible arrangement of DC bus system has been reported in [6] and [7].

Fig. 1(b) incorporates a parallel AC/DC bus approach, with the AC bus at 690V, 60 Hz following conventional ship power systems. Further levels of 440 V and 220 V can be derived through transformers form the main AC bus. Each of the AC generators and loads are connected to the AC bus while the DC sources and loads are connected via converters to the DC bus. A few studies which have merged the two distribution technologies together for shipboard propulsion in order to further reduce conversion stages have come up with the conclusion that parallel AC-DC bus increases efficiency and reduces weight and volume of power converter equipment but increases that of cabling due to the installation of separate AC and DC busses instead of one [8]. Maintenance and labor cost would also increase due to the presence of two different systems. The management strategy is to be optimized in various ways including number of inverters and hence their combined efficiency, voltage of bus, and therefore the appropriate wiring and safety measures, weight and volume.

The fastest developing green technology, namely solar power, will be investigated in more detail to meet ship auxiliary demand. A few projects have successfully integrated photovoltaics into ship power system with results of emission reduction, where some system configurations contribute to auxiliaries alone and others assist towards propulsion [9] [10] [11]. Different modes of operation of the PV arrangement can be addressed to identify the best possible network architecture when combined with the ship grid or operating stand-alone.

TABLE 2: COMPARISON OF BATTERY TECHNOLOGY

Electro-chemistry	Life (years)	Monthly self-discharge at r.t.p. (%)	Energy Density (Wh/kg)	Cycle Efficiency (%)
Pb -acid	5-8	3-5	40	63-90
Li-ion	8-10	5-10	80-190	97
Na	15	~0	100	89-92
Ni-Cd	10-15	20-30	50	72-78
Ni-M-H	8-10	20-30	80	66
Flow Battery	>20	~0	40-70	75-85

Wind turbines mounted on ships require adequate differential wind speed over the turbine rotors and the design of turbine blades may need some alterations to optimize ship performance in presence of energy from wind sources [12]. It is however possible to carry out initial estimation using the data and characteristics of available Horizontal Axis Wind Turbine (HAWT) in the market, along with the meteorological wind speed data. The conclusions drawn in this study has utilized specifications of a market available HAWT. It can be considered that during times of high wind speed or facing a headwind which significantly increases the coefficient of drag C_D, the turbines can be folded down to avoid large backward drag force. In [13], Bockmann has proposed an optimized blade design for turbines installed on-board ships to maximize the net forward force of ships. Although the optimization is based on propulsion, it is also claimed to produce higher power than traditional wind turbines when the ship sails at half the wind speed, due to being designed for higher apparent wind speeds. This paper focuses on the power generation of the wind turbines as opposed to propulsion.

For storage, Li-ion battery technologies are chosen due to their high energy-to-weight ratio and their ability to undergo intensive charge and discharge cycles. Table 2 compares the longevity, energy-density, and efficiency of different battery technology to highlight the best possible option [14] [15] [16] [17]. It has also been noted that Li-ion batteries have a learning curve with a gradient of 21% which means their cost have fallen by 21% for every doubling of production. Due to their use outside grid, e.g. in electric vehicles and consumer items such as cell phones, the cost reduction for this technology of batteries has been faster and most prevalent hence likely to have further cost reductions in the future [18].

The network architecture and their integration into shipboard power system to supply an emission free powering option for the auxiliaries will be approached from a management perspective, since hybridization makes management more complex and diverse. Detailed energy management will be established through analyzing demand and availability of resources and imposing decision making algorithms on the operation scenarios of the network.

TABLE 3: SIZING OPTIONS OF PV ARRAY

Modules per string		**Number of strings**
Minimum	18	118
Maximum	25	85

III. SIZING THE NEW SYSTEM

The first stage of design involves the calculation of solar radiation data for the chosen area in order to be able to specify PV parameters. A fixed mounting is employed since adjustable or tracking types require mechanical bearings and design which would be complicated and costly. For calculating solar radiation on the panel, a solar constant value of 1367 W/m^2 is used, and the Clear Sky Index and Surface Albedo (Ground Reflectivity) values of the North Sea are taken from the NASA website using the appropriate Latitude and Longitude of 56°N and 3°E respectively [19].

For the photovoltaic system, the capacity of PV installation is limited by the useable area of the ship while the power output is dependent on solar insolation at that particular location [20]. Assuming 50% space availability for solar panel installations, due to the shape of the ship not being rectangular and avoiding areas near the shade of cranes, flagstaff, and radar dome etc., an approximate top surface area of 2155 m^2 can be utilized. Marine grade solar panels available in the market have been considered, narrowing on the standard 135 Watt module having an area of 1.01 m^2 with each panel weighing about 10 kg. It is thereby calculated that approximately 23 tonnes of panels can be accommodated on-board. Considering 5 hours of peak average daily sunlight, the panels could produce up to $1438\ kWh/day$ of energy. This can replace about 11% of auxiliary energy delivered by one 600 kW generator over a day.

The PV array is designed based on the known number of PV modules, with the minimum string length being enough to provide the required voltage to turn inverter ON and the maximum number providing lower voltage than maximum inverter input voltage. The following equations are used to determine the maximum and minimum number of modules for the array.

$$Maximum\ number\ of\ modules\ per\ string = \frac{V_{HI}}{V_{HM}} \quad (1)$$

$$V_{HM} = V_{OC} + V_{inc} \quad (2)$$

$$V_{inc} = -T_L \times Temperature\ coefficient\ of\ V_{OC} \quad (3)$$

TABLE 4: PV AND WIND ENERGY CONVERSION SYSTEM PARAMETERS

Area Available for Solar Panel Installation (m^2)	2155
No. of Panels	2130
Energy provided by PV over a day (MWh)	1.438
Wind Turbine Rated Power (kW)	85
No. of Turbines	8
Total Peak Power Provided (kW)	680
Combined weight of PV and Wind Installations (tonnes)	73

Where, V_{HI} = maximum acceptable inverter voltage which can be found from inverter specifications, V_{HM} is the highest voltage expected from each module, T_L is the difference of lowest ambient temperature from STC, and the open-circuit voltage, V_{OC} at STC and its temperature coefficient is obtained from the specification of the solar panel used.

$$Minimum\ number\ of\ modules\ per\ string = \frac{V_{LI}}{V_{LM}} \quad (4)$$

$$V_{LM} = V_{MP} + V_{dec} \quad (5)$$

$$V_{Dec} = T_H \times Temperature\ coefficient\ of\ V_{OC} \quad (6)$$

Where, V_{LI} = minimum acceptable inverter voltage, V_{LM} is the lowest voltage expected from each module, T_H = difference of highest ambient temperature from STC, and the voltage of the module at maximum power, V_{MP} at STC is obtained from the specification of the solar panel used.

The array is finally designed with maximum allowed modules in series to allow lower current flowing for the same watts. Table 3 shows two extreme options for the series-parallel arrangement of PV modules. A series of 25 PV modules in 85 parallel strings thereby make up the array of 2125 modules on-board the tanker.

Wind speed data in three hour intervals for is collected from an offshore location in the North Sea, using NASA online resource. Unlike solar irradiation, wind cannot be predicted to have certain trend depending on the time of the day or the day of the year. When wind speed changes by a factor of 1, the power generated changes by a factor of three. The mechanical power in the upstream wind entering the wind turbine blades is given by (7), and the output power of the turbine extracted by the rotor is given by (8), where ρ is the air density in kg/m^3 and A is the swept area of the rotor blades in m^2.

$$Power = {}^1/_2\,\rho A v^3 \quad (7)$$

$$Power = {}^1/_2\,C_P \rho A v^3 \quad (8)$$

The difference in the equations is due to the Coefficient of Performance (C_P) of the turbine which is essentially the fraction of upstream wind power that is extracted by the rotor, while the remaining energy passes into the downstream wind. This maximum limit of 59.3% energy which can be extracted from the mechanical energy of the upstream wind flowing through the turbine is given as the Betz's limit, although practical wind turbines achieve less than this value due to mechanical losses and aerodynamics. For slow-speed three-blade Horizontal Axis Wind Turbine (HAWT), C_P is in the range of 0.2 to 0.4 [21]. A constant value of 0.3 is therefore chosen for the calculations for the wind speeds giving the wind power and energy output of the turbines.

Eight 85 kW wind turbines are required to replace the peak power provided by one more 660 kW generator and would incur a further 50 ton to be added to the total weight of the ship. However, the excess energy requirement due to overcoming the drag force on a generic wind turbine system can significantly add to the value, unless specifically designed for ship-board application, which will be looked into detail at a later stage. The data for solar and wind energy system is summarized in Table 4.

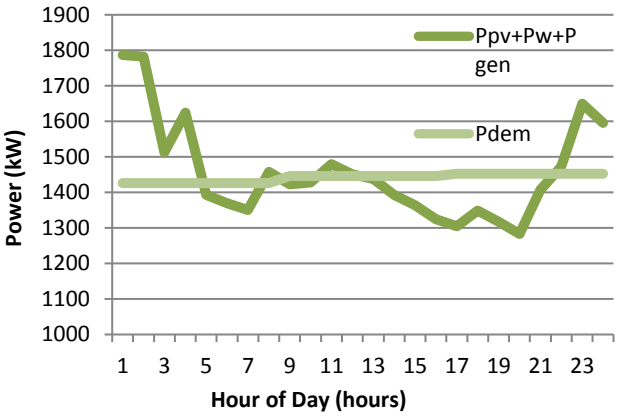

Figure 1: Generation and load profile for tanker operation during cargo unloading at port

The battery capacity must be determined from the maximum power deficit of the combined generation units in relation to load, which needs to be stored during generation for supplying at later times. It is therefore given by (9), where, P_{Gen} is the power supplied by the Diesel Generator Set, P_{PV} is the power generated by the PV Energy Conversion system, P_W is the power given by the wind energy conversion system, P_{dem} is the power demanded by the ship.

$$P_{net} = P_{Gen} + P_{PV} + P_w - P_{dem} \quad (9)$$

$$P_{TOTAL} = P_{Gen} + P_{PV} + P_w + P_{Batt} \quad (10)$$

Each generator will come into use only when P_{TOTAL}, i.e. the combination of the renewable sources and stored energy, and the previous generator, is unable to supply load demand. Fig. 2 shows the load profile of the tanker under the condition of cargo handling at port, when demand is at a maximum. Without renewable energy systems, all three diesel generators would be running to meet the load demand, giving an output power of 1,800 kW. However with the help of wind and PV generated power, and that drawn from the battery during the deficit hours, it would be sufficient for the tanker to operate with only 2 diesel generators for auxiliary electrification, in place of 3.

From Fig. 2, the energy deficit during the 14th to 22nd hour of the day is highest and the battery can be sized according to this requirement calculated to be approximately 867.7 kWh. Considering 3 days of autonomy and 50% depth of discharge, the required battery capacity is calculated to be, 5.21 MWh. With 12 V battery cells available in the market, the combination of 2066 batteries of 210 Ah rating will be able to supply the demand. As a rule of thumb, the battery pack will be able to take as input C/5 or 1 kW, where C is the Battery capacity in Wh. The largest power peak during excess generation is 360 kW; therefore no further energy storage device is required to absorb this power. The average weight of 210 Ah batteries can be taken as 61 kg each, giving an equivalent total of 126 tonnes for the storage system, and volume equal to that of one 30 foot container.

The combined generation and storage system therefore total approximately 200 tonnes. When compared with a case study of an A-Type container ship [22], it is seen that Waste Heat

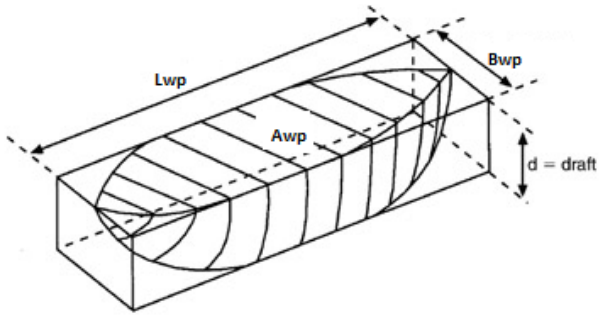

Figure 3: Ship dimension used for calculation of resistance acting upon ship

Recovery (WHR) and Exhaust Gas Recirculation (EGR) systems, when retrofitted into ships to meet current regulations, can have weight penalty of up to 900 tons, which is far greater than installation of the renewables.

A. Extra Weight Related Consumption

A method is detailed for the estimation of extra energy input required to propel the ship owing to the additional resistance imposed by the weight of the new renewable energy system. The extra weight *w* incorporates the weight of the wind turbine system, solar panels and auxiliaries and battery storage system, less the weight of the third generator which is now redundant. Resistance which acts upon the ship comprises of three main divisions, namely the Frictional or Skin Resistance (R_f), Wave Resistance (R_w) and Air Resistance (R_a) [23]. R_f is the resistance due to the viscous stresses that the water exerts on the hull of the ship, R_w is caused by waves generated by the motion of the ship and R_a is resistance caused by the flow of air over the ship. There will be a slight reduction in R_a due to the amount of the hull that dips down into water; however this quantity is very small, about 2%, and therefore can be ignored [24]. The R_w is also more heavily dependent on the hull shape and speed of ship, over displacement, and therefore will not be looked into detail in this study considering the hull shape and speed remains constant for both scenarios [25]. For R_f, using the specified Tonnes per Inch (TPI) of the tanker, it is possible to find the increase in the draught of the ship, given by *d*, and thereby the surface area of the ship pushing through water [26].

$$d = \frac{w}{TPI} \tag{11}$$

$$TPI = \frac{Weight\ to\ increase\ the\ draught\ one\ inch\ (LT)}{1\ in} \tag{12}$$

$$\text{Or, } TPI = \frac{A_{wp}}{420}\left(\frac{LT}{in}\right) \tag{13}$$

Where A_{wp} is the water plane area in ft^2, and is expressed by the following equation, in which, L_{wp} is the length of the water plane, B_{wp} is the hull's largest beam on water plane and C_{wp} is the water plane area coefficient, which is given as 0.95 for a typical tanker at an approximate cruise speed of 17 knots [24].

$$A_{wp} = C_{wp} \times L_{wp} \times B_{wp} \tag{14}$$

Putting the values in place, with L_{wp} of 147 m or 482 ft and the previous value for beam results in water plane area of 40590 ft^2, TPI of 97.63 LT/in and d = 2.07 inch. After conversions into suitable units, this gives an increment of 7.96 m^2 in wetted surface area (A_s), giving rise to higher R_f, which in turn will result in greater fuel consumption for propulsion, given the speed V of the ship remains constant.

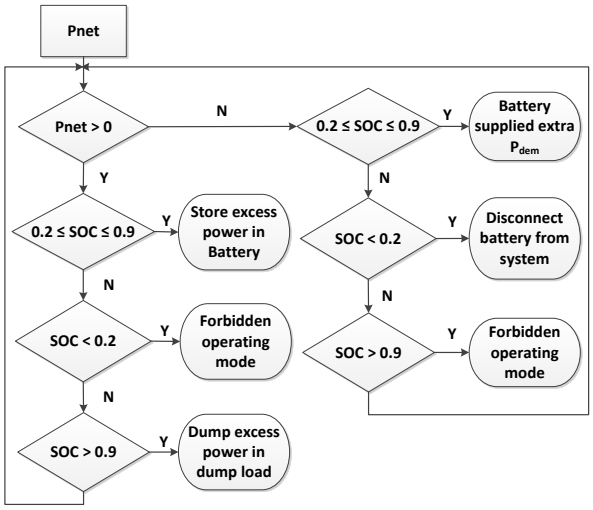

Figure 4: Flow chart of power flow management system

$$R_f = {}^1\!/_2\,\rho V^2 A_s \times C_f \tag{15}$$

Where C_f is specific frictional resistance coefficient and R_n is the dimensionless Reynold's number, given by the following equations [20] [25]. The kinematic viscosity of fluid, given by v, varies according to temperature for a specific fluid. At an average 10°C, the kinematic viscosity of water is given as 1.307 x 10^{-6} m^2/s [27].

$$C_f = \frac{0.075}{(\log R_n - 2)^2} \tag{16}$$

$$R_n = \frac{VL_{wl}}{v} \tag{17}$$

$$P_{ex} = R_f \times V \tag{18}$$

The resulting R_f is 467.3 N, which when multiplied by the speed of the ship gives the increase in effective towing power, P_{ex}, as 4089 W. Over a day, this equates to an added energy consumption of 98 kWh, which is much less in comparison to the extra 6155 kWh of energy given by the combined renewable energy system.

IV. MANAGEMENT

With multiple energy sources such as diesel engine, fuel cells, solar and wind turbines integrated into providing shipboard power, the presence of ESS allows reliability and redundancy by collective usage and management of the sources. A power management strategy has been developed to control the power flow in the hybrid system, and different modes of operation are assigned depending on the different generation and load conditions, as well as the state of the storage system. It is to be noted that when batteries are used as storage devices, their lifetime are sharply affected by their Depth of Discharge (DOD), i.e. there is only a certain range within which a battery can safely

charge and discharge while keeping a healthy lifetime. This range is given between 20% to 90% of the instantaneous state of charge (SOC) of a Lithium-ion battery, which is used in this design [28]. A flow chart of the management system is based on the instantaneous SOC of the battery and P_{net} at each instance, which are the two input and control variables to the system giving rise to six different modes of network operation, as shown in Fig. 4, and as described below.

1) Mode 1: When the sum of instantaneous power generated by renewable technologies is greater than the load which is unmet by the generator ($P_{net}>0$), and the SOC of the battery is within permissible range, the excess energy is stored in the battery for later use.

2) Mode 2: The second mode is similar to the first where there is excess power in the network but the battery SOC is lower than the permitted limit of 20%, hence this operating mode must be forbidden.

3) Mode 3: When there is surplus energy from renewables combined with a battery SOC which is higher than the upper limit, the excess power should be dumped through a load in order to avoid overcharging of batteries.

4) Mode 4: On the other hand, when load demand is greater than generation by renewables and generators, the battery storage system must provide the extra requirement, given the battery SOC is within permitted range to discharge.

5) Mode 5: During discharge of battery, if the SOC falls below its permitted lower limit of 20%, the storage system must be disconnected from load to prevent battery over-discharge. At this point, offline generators must come into operation to provide the load demand.

6) Mode 6: Similarly if demand is greater than generation but SOC of battery is higher than 90%, the system is in a forbidden operating mode again.

The entire process can be controlled through a set of switches, logic gates and control signals. The system thus alternates between modes 1, 3, 4, and 5. It operates at mode-1 to store excess power in the network in the battery until mode 3 is detected whereby the battery power becomes zero and the excess power is dissipated by dump load. When the system operates at mode 4, the battery discharges to provide the loads until it reaches its lower threshold value and the system moves into mode 5 in which diesel generators come online to retain the loads.

V. CONCLUSION

Calculations show that the large available area of the commercial vessel allows it to have substantial PV installations and thereby meet a high percentage of energy generation through PV. Although wind turbines require further investigation based on backward drag force, initial calculations are based on existing HAWT turbines which provides significant amount of renewable energy. The additional weight of the installations is also within reasonable limits to encourage potential investments in this less ventured for area. With multiple energy sources such as diesel engine, fuel cells, solar and wind turbines integrated into providing shipboard power, the presence of ESS allows attainment of efficiency and redundancy by collective usage and management of the sources. The reduction of one auxiliary generator in the chemical tanker studied in this paper allows the remaining generators to operate near their maximum power, allowing better Specific Fuel Consumption (SFC), and increased efficiency, which can result in significant fuel and cost saving, along with the mass of fuel to be carried on-board.

REFERENCES

[1] DNV, "Shipping 2020," Det Norse Veritas As, Hovik, 2012.

[2] Royal Academy of Engineering, "Future Ship Powering Options: Exploring ALternative Metohds of Ship Propulsion," Royal Academy of Engineering, London, 2013

[3] Marine Traffic, "Marine Traffic," Tokyo Marine, 2 April 2015. [Online]. Available: http://www.marinetraffic.com/ais/details/ships/shipid:713221/mmsi:538004002/imo:9490301/vessel:FUJI_GALAXY. [Accessed 2 April 2015].

[4] Yu-Jen Wang, "Harvesting energy from ship rolling using an eccentric disk revolving in a hula-hoop motion," 2014 International Power Electronics Conference (IPEC-Hiroshima 2014 - ECCE ASIA), Hiroshima, 2014, pp. 1420-1424.

[5] Det Norske Veritas AS, "Shipping 2020," Det Norske Veritas AS, Norway, 2012.

[6] J.F. Hansen, J.O. Lindtjørn, K. Vanska, "Onboard DC Grid for enhanced DP operation in ships," in Dynamic Positioning Conference, Houston, 2011.

[7] B. Zahedi and L. E. Norum, "Modeling and Simulation of All-Electric Ships With Low-Voltage DC Hybrid Power Systems," in IEEE Transactions on Power Electronics, vol. 28, no. 10, pp. 4525-4537, Oct. 2013.

[8] J. S. Chalfant, C. Chryssostomidis1 and M. . G. Angle, "Study of Parallel AC and DC Electrical Distribution in the All-Electric Ship," in *Grand Challenges in Modeling and Simulation (GCMS10)*, Ottawa, 2010.

[9] Kyoung-Jun Lee, Dong-Sul Shin, Jong-Pil Lee, Dong-Wook Yoo, Han-Kyu Choi and Hee-Je Kim, "Hybrid photovoltaic/diesel green ship operating in standalone and grid-connected mode in South Korea - Experimental investigation," 2012 IEEE Vehicle Power and Propulsion

[10] , Seoul, 2012, pp. 580-583.

[11] X. J. Tang, T. Wang, C. Zhi and Y. M. Huang, "The design of power management system for solar ship," Transportation Information and Safety (ICTIS), 2015 International Conference on, Wuhan, 2015, pp. 548-553.

[12] S. S. Eirik Bøckmann, "Wind Turbine Propulsion of Ships," in *Second International Symposium on Marine Propulsors*, Hamburg, Germany, 2011.

[13] Nippon Yusen Kabushiki Kaisha, "World's First Solar-Power-Assisted Vessel Further Developed -Car Carrier Auriga Leader to be Fitted with Hybrid Power Supply System and Ballast-Water Management System, and Adapted to Use Low-Sulfur Fuel," 25 May 2011. [Online]. Available: http://www.nyk.com/english/release/1414/ne_110525.html. [Accessed 2 12 2015].

[14] E. Bøckmann, S. Steen, "Wind Turbine Propulsion of Ships," in Second International Symposium on Marine Propulsors, Hamburg, Germany, 2011.

[15] Z. Zhou, M. Benbouzid, J. F. Charpentier, F. Scuiller, T. Tang, "A review of energy storage technologies for marine current energy systems," Renewable and Sustainable Energy Reviews, vol. 18, pp. 390-400, Feb. 2013.

[16] X. Luo, J. Wang, M. Dooner, J. Clarke, "Overview of current development in electrical energy storage technologies and the application potential in power system operation", Applied Energy, Volume 137, 1 January 2015, Pages 511-536

[17] Z. F. Hussien, L.W. Cheung, F.M. Siam, A.B. Ismail, "Modeling of Sodium Sulfur Battery for Power System Applications," Elecktrika, vol 9, no. 2, pp. 66-72, 2007.

[18] C. Ponce de León, A.F. Ferrer, J. González-García, D.A. Szanto, F. C. Walsh, "Redox flow cells for energy conversion," Journal of Power Sources, vol. 160, no. 1, pp. 716-732, 2006.

[19] M. Wilshire, "GLOBAL TRENDS IN CLEAN ENERGY," Bloomberg New Energy Finance, London, 2014.

[20] NASA Langley, "Surface meteorology and Solar Energy," POWER: Prediction of Worldwide Energy Resource Project, [Online]. Available: https://eosweb.larc.nasa.gov/sse/. [Accessed 1 2 2016].

[21] G. J. Tsekouras, F.D. Kanellos "Optimal Operation of Ship Electrical Power System with Energy Storage System and Photovoltaics: Analysis and Application," WSEAS TRANSACTIONS on POWER SYSTEMS, pp. 145-155, October 2013.

[22] M. R. Patel, Wind and Solar Power Systems: Design, Analysis and Operation, CRC Press, 2006

[23] B. Ø. Nielsen, 8500 TEU Container Ship Green Ship of the Future Concept study, Odense Steel Shipyard Ltd, 2009.

[24] D. G. M. Watson, Practical Ship Design, Gulf Professional Publishing, 2002.

[25] MAN Diesel & Turbo, "Basic Principles of Ship Propulsion," MAN Diesel & Turbo, Copenhagen, 2011.

[26] University of Strathclyde, "Basics of Ship Resistance," University of Strathclyde, Strathclyde, 2011.

[27] P.H. Miller, "Hull Form and Geometry: Intro to Ships and Naval Engineering (2.1)," United States Naval Academy, Annapolis, 1997.

[28] 26th ITTC Specialist Committee, "ITTC – Recommended Procedures Fresh Water and Seawater Properties," IITC, 2011.

[29] M. Stadler, M. Kloess, M. Groissböck, G. Cardoso, R. Sharma, M. C. Bozchalui and C. Marnay, "Electric Storage in California's Commercial Buildings," *Applied Energy,* vol. 104, pp. 711-722, 2013.

Sanjana Ahmed received the B.Sc. degree in electrical and electronic engineering from BRAC University, Dhaka, Bangladesh, in 2013 and the M.Sc. degree in electrical engineering for sustainable and renewable energy from University of Nottingham, Nottingham, UK, in 2014. She is currently pursuing the Ph.D. degree in electrical and electronic engineering at the Power Electronics, Machines and Control Group at the University of Nottingham, UK.

Her research interest includes renewable energy technologies, management of power network, energy storage and marine application of renewable energy.

Alberto Castellazzi received the M.S. degree in physics from the University of Milan, Milan, Italy, and the Ph.D. degree in electrical engineering from the Munich University of Technology, Munich, Germany. He is currently a Lecturer in power electronics with the Power Electronics, Machines, and Control Group, University of Nottingham, Nottingham, U.K. He has been engaged in research in power electronics circuits and devices for more than ten years and has been affiliated to some of the main European institutions in the field (Siemens Corporate Technology, TU Munich, ETH Zurich, ALSTOM-PEARL). His current research interests include the multi-domain multilevel abstraction modeling and simulation of power components and assemblies, novel packaging and integration approaches for semiconductor power devices, high-temperature electronics (SiC), dc–dc converters, and reliability investigations.

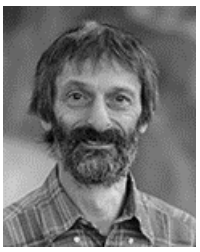

Arthur Williams received a B.A. in engineering science from St. John's College, Oxford and then worked for GEC Large Machines in Rugby in Electrical Machine Development. Later he began research into micro-hydro systems, often working in collaboration with the Intermediate Technology Development Group (now "Practical Action"). He completed a PhD at Nottingham Trent University in 1992. He has been involved in the development and dissemination of low-cost technologies for rural electrification, and has visited Nepal, Pakistan, Sri Lanka and Peru in connection with this work. He has been a lecturer in Electrical and in Mechanical Engineering at Nottingham Trent University before transferring to the University of Nottingham in 2007. He lectures in the field of sustainable energy and is course director for the interdisciplinary MSc in Sustainable Energy Engineering. His research is in Renewable Energy systems.

Power Sharing Strategy for Photovoltaic based Distributed Generators Operating in Parallel

Urvi N. Patel and Hiren H. Patel

Abstract— **In many countries, the grid-code or standards do not allow the Photovoltaic (PV) inverters to exchange reactive power with the grid. Recently, some countries have relaxed the standards. Hence, capacity of the inverters to control reactive power must be utilized. However, the reactive power that a PV inverter can supply is constrained by the maximum power that a PV array generates and changes with the environmental conditions. A reactive power sharing algorithm is proposed that not only ensures proper distribution of reactive power amongst the inverters, but also ensures that the maximum power generated by PV is supplied to the grid. In case of identical PV inverters, the algorithm operates all inverters at nearly equal apparent power leading to nearly equal percentage utilization of the inverters, thereby achieving uniform heating of the similar devices of the inverters. The algorithms are further investigated for power sharing amongst PV inverters of unequal ratings. It is highlighted that the proposed algorithm results into the least change in the utilization factor of a PV inverter, whose power changes due to the change in environmental conditions. The effectiveness of the algorithm over other algorithms in sharing power amongst inverters is displayed through MATLAB/Simulink simulations.**

Keywords — Photovoltaic, Reactive power, Power sharing.

I. Introduction

Last couple of decades have experienced significant rise in the electricity generation from non-conventional energy sources like wind and solar. It is attributed mainly by the increased environmental concern, fast depletion of conventional energy sources, increase in cost of conventional energy sources, and decrease in the cost of renewable based energy generation. In recent years, one of the renewable sources that has seen the fastest growth and penetration in the electrical grid is the solar photovoltaic (PV). The reason for the increase in penetration is the reduced cost of PV system and the encouraging feed-in-tariff policies by the governments. However, increased penetration of PV sources has also given rise to several challenges.

The challenges are mainly due to the dependence of PV source's performance on the environment, which makes it intermittent and uncertain in nature. PV source is connected to the grid through the static power converters [1]. Thus, it is inertia-less source of energy unlike the conventional rotational generators. Hence, if the energy generation in the grid is highly dominated by inertia-less PV (i.e. in a weak grid), the sudden change in output power of PV resulting from the sudden change in irradiation, may affect the stability of grid and the systems connected with the utility. Also, if the power electronic converters are not controlled appropriately in such weak electrical grid or a microgrid (MG), they are likely to create issues like harmonic injection, change in voltage levels and power flow, flicker, resonance, mal-operation of protection scheme etc.

On the contrary, if the power electronic converters are properly controlled [2]-[3], they can improve the voltage profile and performance of the MG. This can be achieved if PV systems, which are usually commissioned to supply active power, are allowed to inject desired reactive power into the grid. PV systems are usually designed with reasonable margins, and most of the times operate under lightly loaded conditions (in fact inactive at night time). Thus, there is a room for reactive power injection to keep the voltage at a desirable level. This objective, along with the transfer of maximum power generated by PV, can be achieved by controlling the amplitude and phase angle of the output voltage of the inverter. The task becomes challenging when several such PV based distributed energy generators are operating in a MG, which even comprises of other types of renewable energy sources.

PV inverters are commonly controlled as current controlled source using P-Q control strategy to exchange active and reactive P and Q respectively, with the microgrid [4]. In islanding mode i.e. when main grid is disconnected, the voltage V and frequency ω are controlled, using P-ω and Q-V droop control methods to share active and reactive power amongst the distributed generators (DG) [5]-[7]. Battery storage is essential in such system when islanded, in order to maintain power balance in the system.

Lasseter *et al.*, have presented flexible control and proper coordination amongst DG sources to overcome some problems associated with PV and other non-conventional sources operating simultaneously in a MG [3]. Local power management system for coordination of various DG sources to manage active and reactive power successfully is addressed in [8]-[10]. In [8], fundamental algorithm employing hierarchical droop control of power management is presented, where inverter control is considered as primary control whereas Microgrid Central Controller (MGCC) is under secondary control. Secondary control focuses on power management and optimization algorithm to optimize performance of MG.

Power management system plays very important role when MG is having many PV connected inverters, as rapidly varying irradiation condition may cause voltage sags and swells that result in degradation of power quality [16]-[20]. To regulate voltage under such transient condition, PV inverters must have

U. N. Patel is with Department of Electrical Engineering, C. K. Pithawala College of Engineering and Technology, Surat, India. (email: urvi.patel@ckpcet.ac.in).

H. H. Patel is with the Department of Electrical Engineering, Sarvajanik College of Engineering & Technology, Surat, India. (e-mail: hiren.patel@scet.ac.in).

the capability to match-up the VAR requirement quickly [11]. As active power delivered by inverter depends on maximum power that PV can generate under given (environmental) conditions, it is necessary to allocate reactive power amongst inverters in a proper way to have uniform loading of the inverters and to also avoid over loading of inverters [12]. An accurate reactive power sharing control that shares reactive power equally amongst inverters is presented [13]. Total reactive power of the system is calculated by MGCC and the information is passed to all inverters through communication link. Though this method shares reactive power accurately amongst the inverters, in case when active power varies with the change in irradiation, it fails to accurately share the reactive power amongst the PV inverters. It may also cause inverter to work beyond its nominal apparent power transfer capability.

In [14], reactive power algorithm is presented which takes into account apparent power limit of each PV connected inverter as well as active power delivered by each PV inverter. Optimal reactive power strategy [15] assigns reactive power to each inverter such that entire system can achieve maximum reactive power transfer capability. However, these algorithms are unable to uniformly utilize apparent power capability of each inverter.

The paper proposes an approach to overcome these drawbacks. The proposed reactive power algorithm first determines the active power that PV inverters are supplying under given conditions and based on the available margin it assigns the reactive powers to the inverters. Section II introduces system configuration and control scheme employed for operating PV inverters while the secondary control algorithm implemented in MGCC for accurate reactive power sharing is presented in section III. The results of the simulation study performed in MATLAB/Simulink are included in section IV to demonstrate the performance of algorithm for PV inverters operating in parallel for two different cases: (*i*) all inverters with equal ratings and (*ii*) inverters with unequal ratings.

II. System Description and Control

Fig.1 shows the system configuration considered for evaluation of the proposed algorithm. The microgrid comprises of four identical distributed energy generators that along with the main grid (or a relatively stiff source) supply the local loads. Each DG unit consists of PV as a primary energy source, a three phase inverter and an LC filter. The inverters not only extract the maximum power from the PV but also supply sinusoidal current to the load and grid. PV_i shown in Fig. 1 represents a PV array with its dc-dc converter operated with maximum power point tracking control. The DGs are connected to the PCC through a transformer, which for the sake of simplicity, is not shown in Fig.1.

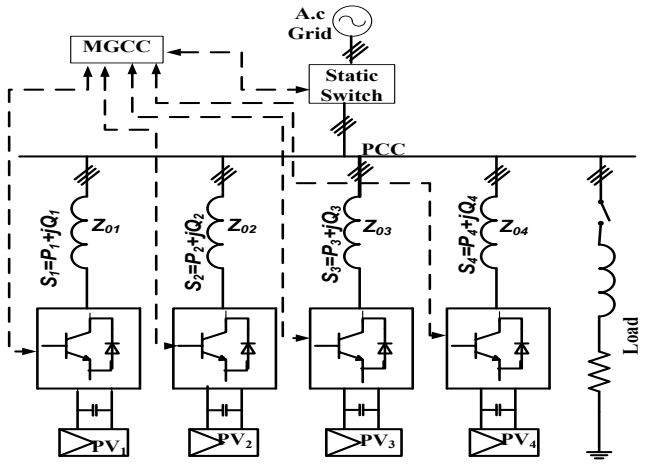

Fig.1. System configuration of a Microgrid having four DGs

The impedances Z_{oi}, where '*i*' represents i^{th} DG, takes into account the impedance of interfacing inductor, the impedance of cable and isolation transformer. Active and reactive power management task is performed by MGCC unit using low bandwidth communication links.

Microgrid hierarchical structure consists of mainly primary, secondary and tertiary control [10], [11]. Primary control covers inverters' control present in microgrid whereas secondary control consists of MGCC unit. Tertiary control provides interaction between multiple microgrid and utility grid. Primary and secondary controls are used in this paper while tertiary control is not required at this stage.

Inverter control is achieved by active-reactive power (*P-Q*) control method [4]. *P-Q* method is used to operate inverter as a controlled current source for desired active and reactive power transfer with grid. Inverter output current is tightly regulated by inner current control loop. Reference currents for current control loop are provided by outer power control loop according to power references provided by MGCC. Phase locked loop (PLL) used for grid synchronization provides desired angle (ρ) for *abc* to *dq* frame transformation. Fig.2 shows control circuit diagram for one of the inverters.

Fig.3 shows the details of the power and current control loops shown in Fig. 2. The voltage V_{dc}, across capacitor C is maintained at a desired voltage, V_{dcref} by a voltage control loop.

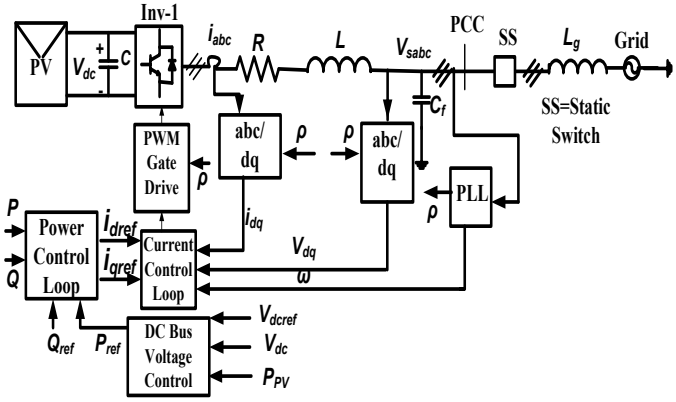

Fig. 2. Control scheme of PV inverter

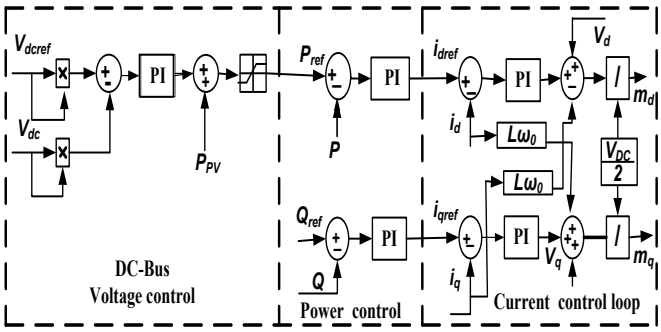

Fig.3. Active-reactive power control

To maintain this voltage constant it is ensured that the power obtained from PV array, P_{PV} is entirely transferred to the grid side. This is done through the power control loop, which compares actual DG output power *(P*) with reference power (P_{ref}). The reactive power reference (Q_{ref}) is obtained using the algorithm presented in the next section. P_{ref} and Q_{ref} are used to generate required current references i_{dref} and i_{qref} for the current control loop. The direct and quadrature axes components of the inverter output currents i_d and i_q, respectively, are obtained through *d-q* transformation. The current control loop finally determines the direct and quadrature components of the reference waveform from the direct and quadrature axes modulation indices, m_d and m_q, respectively.

III. Proposed Reactive Power Sharing Algorithm

As the active power that PV inverters supply is directly dependent on the environmental conditions (mainly irradiation), most of the times the inverters do not operate at their rating and hence, their capacity is not utilized fully. The available margin varies with the irradiation, with maximum at night or when irradiation is the least. The reactive power sharing algorithm shown in Fig. 4 relies on assigning the reactive power algorithm amongst the inverters based on the margin available with each of them.

The algorithm starts with initializing the number of inverters (m) and the apparent ratings of the inverters (S_{iN}), where 'i' stands for i^{th} inverter. The output power of the PV systems (P_i) is obtained from the maximum power point tracker (MPPT), which ensures that the PV system operates at its maximum (active) power point.

As the apparent power ratings (S_{iN}) of the inverters are known and as the inverter must be operated to deliver active power (P_i) to the grid side, the available reactive power (Q_i) is expressed as

$$Q_i = \sqrt{S_{iN}{}^2 - P_i^2} \tag{1}$$

The inverter is capable of supplying and drawing reactive power and it must match the load and grid requirements. Accordingly (2) and (3), assigns the reactive power limits for lagging and leading type of reactive demand, respectively.

$$Q_{i\max} = Q_i \tag{2}$$

$$Q_{i\max} = -Q_i \tag{3}$$

Hence, at a given instant, the total active power (P_T), reactive power (Q_T) and apparent power (S_T) capabilities that the inverters possess to match the reactive power demand of load and to supply the active power of PV systems to grid are represented by (4), (5) and (6), respectively.

$$P_T = \sum_{i=1}^{m} P_i \tag{4}$$

$$Q_T = \sum_{i=1}^{m} Q_i \tag{5}$$

$$S_T = \sqrt{P_T{}^2 + Q_T{}^2} \tag{6}$$

If output currents of all the inverters are equal, temperature of similar devices of the different inverters can be made equal. This can be realized if all the inverters operate with the same apparent power. Hence, the inverters are made to operate with the reference apparent power (S_{Tnew}) to have uniform utilization and heating.

$$S_{Tnew} = S_T \div [(m+1) - i] \tag{7}$$

The algorithm evaluates the condition expressed by (8), and if S_{Tnew} exceeds S_{iN}, the reference apparent and reactive powers are set to values S_{iN} and Q_{imax} (or Q_{imin}), respectively.

$$S_{Tnew} \le S_{iN} \tag{8}$$

The algorithm then assigns the reference reactive power Q_{iref} and P_i for each inverter, where the active power references (P_i) for the inverters are obtained from the MPPT. Once any inverter is assigned the reference active and reactive powers, the total unassigned active and reactive powers to be supplied by the remaining inverters are updated by subtracting the Q_{iref} and P_i assigned to the earlier inverters from P_T and Q_D, where Q_D is the reactive power demand of the load. The remaining active power (P_{Tn}) to be supplied and reactive power demand to be met (Q_{Tn}) is calculated as shown in (9), and (10), respectively.

$$P_{Tn} = P_T - \sum_{i=0}^{i-1} P_i \text{ where } P_0 = 0 \tag{9}$$

$$Q_{Tn} = Q_D - \sum_{i=0}^{i-1} Q_{iref} \text{ where } Q_{0ref} = 0 \tag{10}$$

Accordingly, the apparent power (S_i) that i^{th} inverter must supply is obtained by (11)

$$S_i = \sqrt{P_{Tn}{}^2 + Q_{Tn}{}^2} \,/\big((m+1) - i\big) \tag{11}$$

Hence, the reference reactive power for the i^{th} inverter is

$$Q_{iref} = \sqrt{S_i{}^2 - P_i^2} \tag{12}$$

IV. Simulation Results

To demonstrate the effectiveness of the above control strategy, microgrid system shown in Fig.1 is simulated in MATLAB/Simulink. In addition to the proposed control algorithm, two more control approaches: (optimal reactive power [15] and equal reactive power sharing [13]) are also evaluated and the results are compared with that obtained with the proposed control algorithm. Two different cases are considered for comparing the performance of this algorithm.

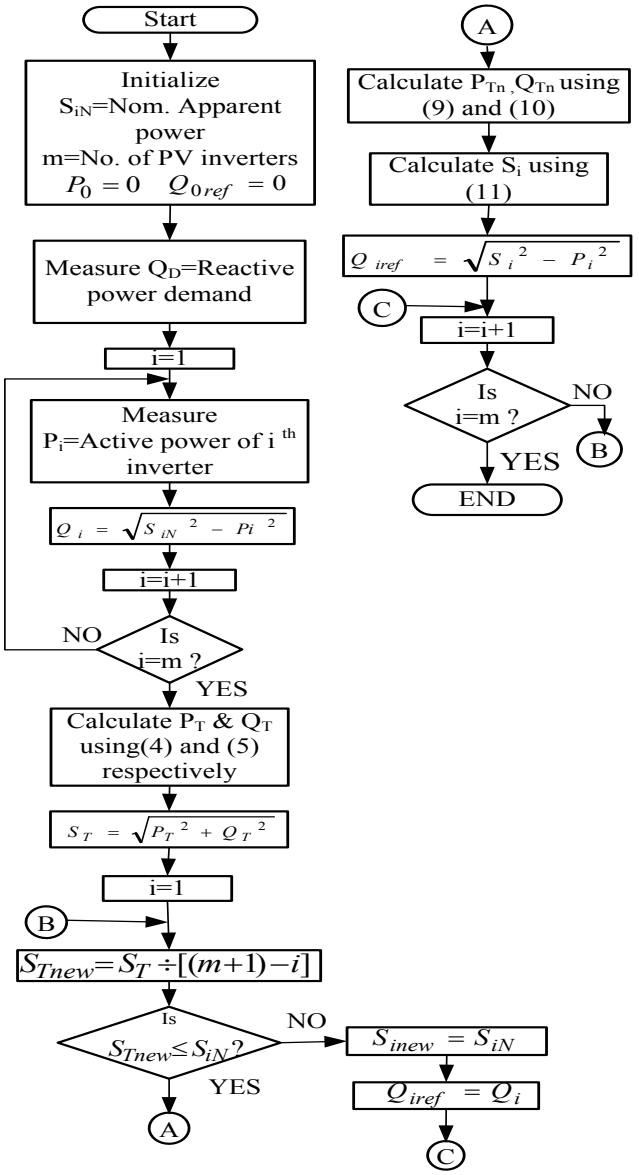

Fig. 4. Proposed reactive power sharing algorithm

In case (*i*), all the inverters are considered to have the equal ratings while in case (*ii*), inverters of unequal ratings are considered.

Case (i): Equal DG ratings

The parameters considered for evaluating the performance of the algorithms using the system of Fig. 1 are mentioned in TABLE I. As shown, all DGs are considered to have the equal nominal apparent power rating of 500 kVA.

TABLE I
RATINGS AND PARAMETERS FOR THE SYSTEM OF FIG.1

Nominal power rating of DG1 (S_{1N})	500 kVA
Nominal power rating of DG2 (S_{2N})	500 kVA
Nominal power rating of DG3 (S_{3N})	500 kVA
Nominal power rating of DG4 (S_{4N})	500 kVA
Grid voltage(V_g), Frequency(f)	415V, 50 Hz
Line parameter (Z_{01}=Z_{02}=Z_{03}=Z_{04})	L=100μH,R=2.07mΩ,C_f=2500μF
Load	1.92 MVA, 0.78 power factor (lag)
No of PV inverters (m)	4

Fig. 5 shows the results with the optimal reactive power sharing (ORPS) algorithm. Reactive power references for inverters shown in TABLE II are calculated using the ORPS algorithm of [15], while the active power references for the inverters are set at the value equal to the maximum power that the corresponding PV system generates at a given instant. The active power generated by PV arrays PV_1, PV_2, PV_3 and PV_4 till t=0.5s are 400kW, 300kW, 250kW and 450kW, respectively. A step change in irradiation on PV array PV_1 occurs at t=0.5s, which results in the output of PV_1 to decrease to 200kW. At t=1s, step change in irradiation on PV array PV_3 occurs, resulting into the change in the output power from 250kW to 400kW. Reactive power references for the inverters obtained with optimum reactive power control are mentioned in TABLE II. Fig. 5, shows active, reactive and apparent power of inverters 1 through 4.

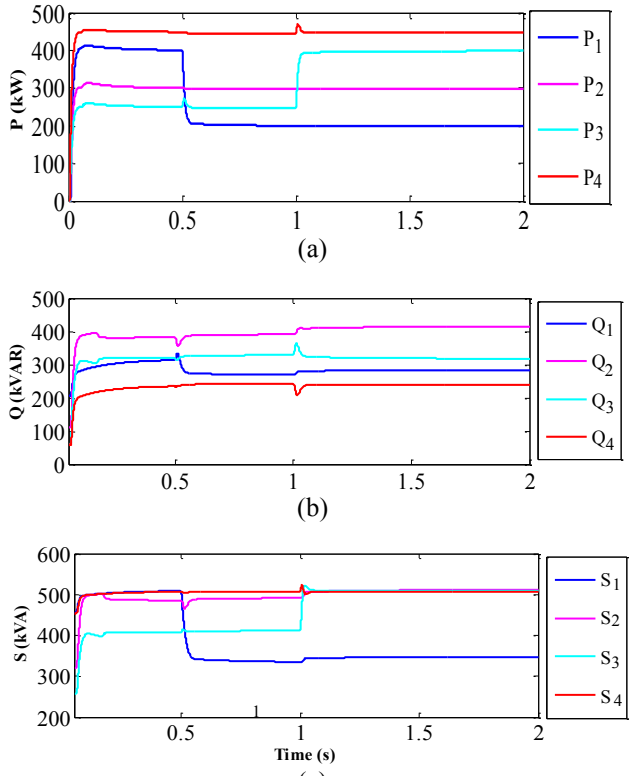

Fig. 5. Results with ORPS algorithm: (a) active power fed by DGs, (b) reactive power shared by the inverters, (c) apparent power of each inverter.

TABLE II
UTILIZATION FACTOR OF EACH DG FOR ORPS ALGORITHM

Time Interval (s)	P_i (kW)	Q_{iref} (kVAR)	S_i (kVA)	Uti. Fac. S_i/S_{Ni}
t=0-0.5	400	300	500	1.00
	300	373	478	0.95
	250	310	398	0.79
	450	218	500	1.00
t=0.5-1	200	262	329	0.65
	300	392	493	0.98
	250	325	410	0.82
	450	218	500	1.00
t=1-2	200	282	345	0.69
	300	400	500	1.00
	400	300	500	1.00
	450	218	500	1.00

It is observed from Figs. 5(a) and (b) that, when P_1 is decreased from 400kW to 200kW at t=0.5s, Q_1 changes from 300kVAR to 262kVAR. Not only Q_1, but Q_2 through Q_4 also changes. Similarly at t=1s, when P_3 increases to 400kW, Q_1 through Q_3 changes. Thus, if power generated by any one of the PV array changes, the reactive power references and hence, the reactive power supplied by all the inverters change (except those which are operating at their limits S_{iN}). Fig. 5(c) shows that inverters 1 and 4 operate at their maximum apparent power limits (S_{1N} and S_{4N}, respectively) till t=0.5s. At t=0.5s, when P_1 reduces, Q_1 also reduces simultaneously and hence, from t=0.5s to t=0.1s only inverter 4 operates at its full capacity. It is observed that the change in P_i and Q_i is such that the ratio P_i/Q_i remains equal for all the inverters that do not reach the rated capacity. An index defined as utilization factor (S_i/S_{iN}) is used to indicate the extent to which the capacity of the inverter is utilized. It is also observed from the TABLE II that all the inverters are operating at different utilization factors. The utilization factors vary greatly showing that some of the inverters operate much below their rated capacity when some others have already hit their limits. For example, inverter-1 operates with the lowest utilization factor (0.65 from t=0.5s till 1s and 0.69 from t=1s till 2s) while inverter-4 is operating at its limit. The unequal utilization of the inverters, not only results into unequal losses, efficiency and heating of different inverters, but may damage the inverters that continuously operate at their apparent power limits.

Fig. 6 shows the results obtained with equal reactive power sharing (ERPS) algorithm [13], according to which reactive power demand is equally shared amongst the inverters. The

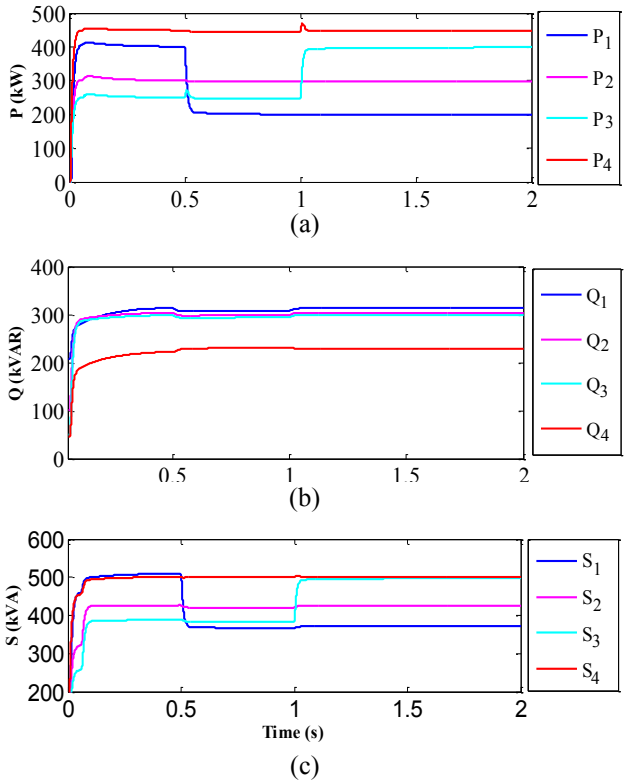

Fig. 6. Results with ERPS algorithm: (a) active power fed by DGs, (b) reactive power shared by the inverters, (c) apparent power of each inverter

irradiation pattern on the PV array is considered the same as that considered for the evaluation of ORPS approach. Fig. 6

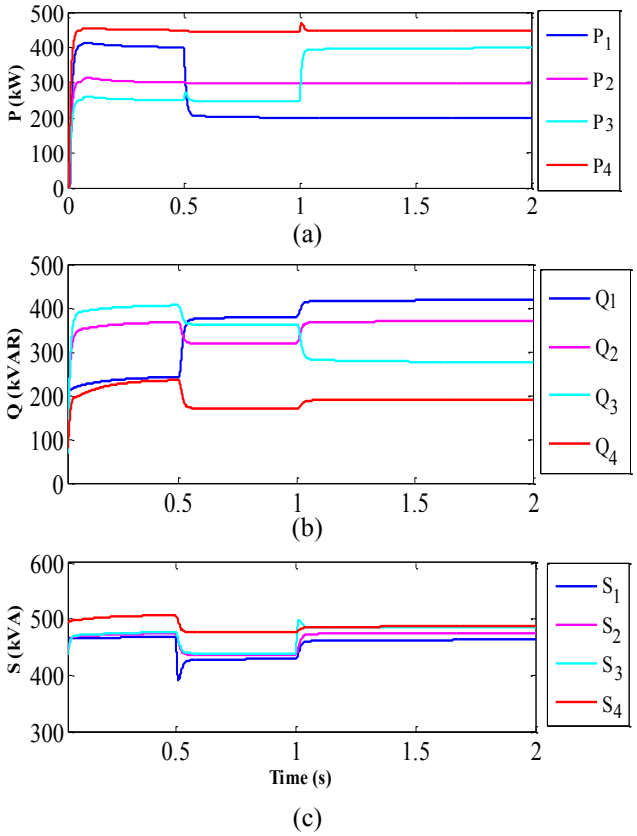

Fig. 7. Results with Proposed algorithm: (a) active power fed by DGs, (b) eactive power shared by the inverters, (c) apparent power of each inverter

shows active, reactive and apparent powers respectively, of inverters 1 through 4.

If it is intended to meet the total reactive power demand of the load mentioned in TABLE I (1200kVAR) through the inverters 1 through 4 using ERPS control, each inverter must output 300kVAR. Hence, the reference reactive power for inverter 1,2 and 3 are set equal to 300kVAR (reactive power demand of load = 1200kVAR) while for inverter- 4 which hits its apparent power limit, it is restricted to 218 kVAR. It is observed from Figs. 6(a)-(c), and TABLE III that, even if the active power supplied by the PV array changes, the effect is not observed in the reactive power sharing. It is also evident from Fig. 6(c) that inverter-4 continuously operates at its rated capacity of 500kVA. Inverters 1 and 3 also operate at their rated capacities for some time. It is also observed that S_i (for i=1, 2 and 4) remains almost constant for t=0.5s to 2s inspite of the change in P_3 at t=1s. The reason being no change in P_i and Q_i (for i =1, 2 and 4) for this period. Unlike ORPS the reactive power demand of the load is not met fully inspite of the fact that many inverters still operate below their rated limits. Thus, the inverters are not utilized optimally and also the percentage utilization of all the inverters varies greatly.

Fig.7 shows performance with proposed algorithm when same pattern of irradiation on the PV array as that considered for ORPS and ERPS is maintained. At t=0.5s, when the irradiation of PV_1 decreases resulting into the decrease in the

TABLE III
UTILIZATION FACTOR OF EACH DG FOR ERPS ALGORITHM

Time Interval(s)	P_i (kW)	Q_{iref} (kVAR)	S_i (kVA)	Uti. Fac. S_i/S_{Ni}
t=0-0.5	400	300	500	1.00
	300	300	424	0.84
	250	300	390	0.78
	450	218	500	1.00
t=0.5-1	200	300	360	0.72
	300	300	424	0.84
	250	300	390	0.78
	450	218	500	1.00
t=1-2	200	300	360	0.72
	300	300	424	0.84
	400	300	500	1.00
	450	218	500	1.00

output power of inverter 1, the reactive power of inverter 1 increases. Simultaneously, the reactive powers of all other inverters decrease in spite of the fact that there is no change in the power output from PV arrays PV_2, PV_3 and PV_4. This results into minimizing the gap of percentage utilization of different inverters. Similarly, at t=1s when P_3 changes from 250kW to 400kW, reactive power of all the inverters changes to achieve better sharing of the active and reactive power amongst them. TABLE IV shows the active, reactive and apparent powers shared by the inverters over the different periods. Unlike ORPS and ERPS, the utilization factors vary little for all the DGs indicating uniform loading of the inverters.

The three algorithms are tested even with a different load having a leading power factor (PF). TABLE V shows the results obtained with a load of 1.16 MVA, 0.86 power factor (lead). It is observed that even with leading power factor, proposed algorithm performance is superior. Standard deviations of the utilization factors of the various inverters are calculated, to quantify the effectiveness of the algorithm to distribute the apparent power equally amongst the inverters. Standard deviations of the utilization factors for the three schemes for the case represented by TABLE V are 0.204, 0.147 and 0.055. The least the standard deviation better is the performance.

TABLE IV
UTILIZATION FACTOR OF EACH DG FOR PROPOSED ALGORITHM

Time Interval(s)	P_i (kW)	Q_{iref} (kVAR)	S_i (kVA)	Uti. Fac. S_i/S_{Ni}
t=0-0.5	400	229	460	0.92
	300	354	464	0.92
	250	393	466	0.93
	450	222	500	1.00
t=0.5-1	200	374	424	0.85
	300	311	432	0.86
	250	355	434	0.86
	450	159	477	0.95
t=1-2	200	405	452	0.90
	300	356	465	0.93
	400	262	478	0.95
	450	175	482	0.96

TABLE V
COMPARISON OF THE VARIOUS ALGORITHM FOR LEADING PF LOAD

Algorithms	P_i (kW)	Q_{iref} (kVAR)	S_i (kVA)	Uti. Fac. S_i/S_{Ni}
ORPS	300	-180	350	0.70
	200	-120	233	0.46
	150	-90	175	0.35
	350	-210	408	0.82
ERPS	300	-150	335	0.67
	200	-150	250	0.50
	150	-150	212	0.42
	350	-150	380	0.76
Proposed	300	0	300	0.60
	200	-233	307	0.61
	150	-271	309	0.61
	350	-96	362	0.72

Case (ii): Unequal DG ratings

The three algorithms are also evaluated for the case when all DGs of the system shown in Fig. 1 have unequal ratings. The nominal ratings for the DGs are mentioned in TABLE VI. The load, line parameters, capacitance C and the grid voltage are considered same as that of case (*i*).

In this case the active power generated by PV arrays PV_1, PV_2, PV_3 and PV_4 are 200kW, 300kW, 400kW and 500kW, respectively. A step increase in irradiation on PV array PV_1 occurs at t=0.5s, which results in the output of PV_1 to increase to 300kW. At t=1s, irradiation on PV array PV_3 decreases suddenly, resulting into the change in its output power from 400kW to 200kW. The active, reactive and apparent power sharing by inverters 1 through 4 with ORPS control are displayed in Fig. 8 and the results are quantified in TABLE VII.

Figs. 8(a) and (b) shows that when PV_1 is increased from 200kW to 300kW at t=0.5s, Q_1 also increases from 171kVAR to 240kVAR. Hence its apparent power increases, leading to its utilization factor of 0.96. The reactive powers of inverters 2 through 4 decrease with their active powers still at the same values. Thus, S_2 through S_4 decrease lowering the utilization of inverters 2 through 4. This increases the miss-match in the utilization factors. The miss-match further increases after t=1s, when the output power of PV_3 decreases from 400kW to 200kW. The decrease in P_3 at t=1s is associated with the simultaneous decrease in Q_3. Hence, to meet the reactive power demand of the load, more reactive power needs to be supplied by inverters 1, 2 and 4. Hence, while the utilization factor of inverter-3 decreases, utilization factor of other inverter increases .Thus, inverter-3 is the least utilized inverter with utilization factor of 0.45 while inverter-1 is fully utilized with the utilization factor of 1.00. Fig. 5(c) also highlights that after t=1s, inverter-1 operates at its apparent power limit (S_{1N}). It is observed from TABLE VII that the percentage change (decrease) in utilization factor of inverter-3 in response to the decrease in output power P_3 of inverter-3 is -47%.

Fig. 9 shows the power shared by DGs (having ratings mentioned in TABLE VI) when operated with ERPS algorithm. The same shading pattern, adopted earlier for ORPS of case (*ii*), is considered. The reference reactive power for all the inverters is set equal to 300kVAR to meet the load's reactive power demand (TABLE VIII). Fig. 9(c) shows that after t=0.5s, inverter-1 continuously operates at its rated capacity 400kVA and hence, is unable to meet its desired reactive power share of 300kVAR. Like earlier case with ERPS control, the reactive

TABLE VI
Ratings Of Dg Of The System Of Fig.1 For Case (ii)

Nominal power rating of DG1 (S_{1N})	400 kVA
Nominal power rating of DG2 (S_{2N})	500 kVA
Nominal power rating of DG3 (S_{3N})	600 kVA
Nominal power rating of DG4 (S_{4N})	700 kVA

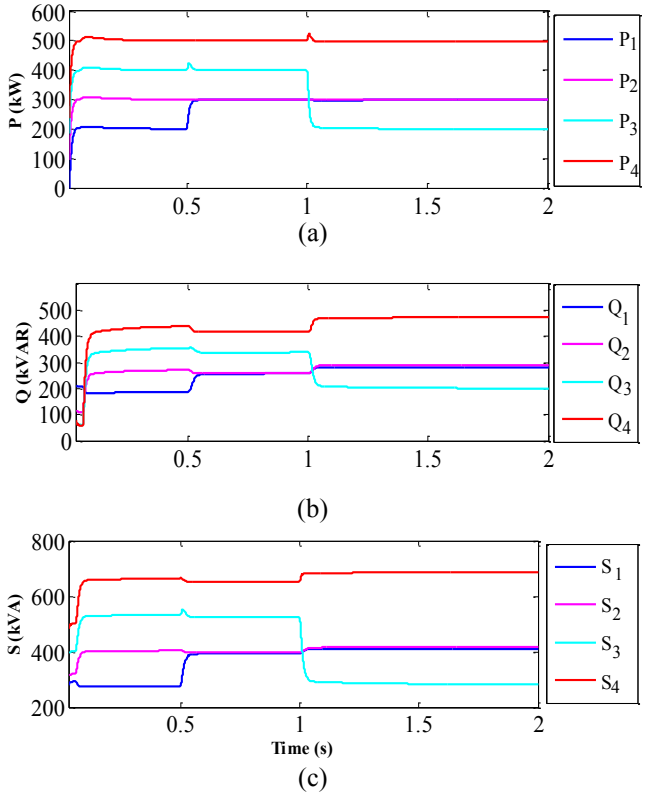

Fig. 8. Results with ORPS algorithm: (a) active power fed by DGs, (b) reactive power shared by the inverters, (c) apparent power of each inverter

power demand of the load is once again not met fully. Thus, the inverters are not utilized optimally. Significant variation in utilization factors is observed. Also the percentage change in the utilization factor of inverter-3 due to change in P_3 at t=1s is -27.7%. The power sharing, the utilization factors and the variation in the utilization factors are highly dependent on the nominal ratings of the inverters and the load.

Fig. 10 shows performance of proposed algorithm with same pattern of irradiation on the PV array as considered earlier for ERPS and ORPS algorithm of case (ii). It is observed from TABLE IX that during t=0s to t=0.5s, the proposed algorithm tries to share the apparent power equally amongst all the inverters. Hence, as the inverter-1 reaches its limit, it is operated at 400kVA (100% capacity), while inverters 2, 3 and 4 are operated around 500kVA demonstrating the tendency of equalizing the reactive power sharing. At t=0.5s, when the irradiation of PV_1 increases resulting into the increase in the output power of inverter 1, the output reactive power of inverter 1 decreases. Simultaneously the reactive powers of all other inverters increase.

TABLE VII
UTILIZATION FACTOR OF EACH DG FOR ORPS ALGORITHM

Time Interval(s)	P_i (kW)	Q_{iref} (kVAR)	S_i (kVA)	Uti. Fac. S_i/S_{Ni}
t=0-0.5	200	171	263	0.65
	300	257	395	0.79
	400	342	526	0.87
	500	425	656	0.93
t=0.5-1	300	240	384	0.96
	300	240	384	0.76
	400	320	512	0.85
	500	400	640	0.91
t=1-2	300	276	407	1.00
	300	277	408	0.81
	200	185	272	0.45
	500	462	680	0.97

TABLE VIII
UTILIZATION FACTOR OF EACH DG FOR ERPS ALGORITHM

Time Interval(s)	P_i (kW)	Q_{iref} (kVAR)	S_i (kVA)	Uti. Fac. S_i/S_{Ni}
t=0-0.5	200	300	360	0.90
	300	300	424	0.84
	400	300	500	0.83
	500	300	583	0.83
t=0.5-1	300	265	400	1.00
	300	300	424	0.84
	400	300	500	0.83
	500	300	547	0.78
t=1-2	200	265	400	1.00
	300	300	424	0.84
	200	300	360	0.60
	500	300	547	0.78

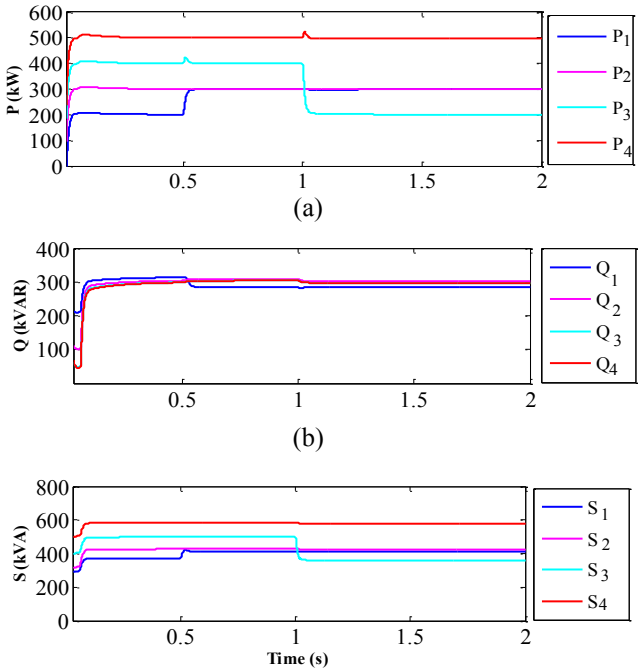

Fig.9. Results with ERPS algorithm (a) active power fed by DGs, (b) reactive power shared by the inverters, (c)apparent power of each inverter

This results into minimizing the miss-match in the reactive powers of the inverters and hence, reduces the gap of percentage utilization of different inverters. Thus, the algorithm inherently has the feature of minimizing the mismatch. But still the mismatch is relatively large. This is due to the equal apparent power sharing principle of the algorithm, which inspite of the unequal nominal kVA rating of the inverters, tries to allocate the apparent power equally amongst the DG inverters. Hence, it results into the unequal utilization factor of the DGs. At t=1s when P_3 changes from 400 kW to 200kW, Q_3 increases and Q_4 and Q_2 decrease to achieve better power sharing amongst the inverters. The least utilization factor of 0.6 is observed for inverter-3. It is observed from TABLE IX that percentage decrease in utilization factor for inverter-3 (due to

change in P_3 at t=1s) is -13.8%, which is relatively smaller than that observed with ORPS (-47%) and ERPS (-27.7%).

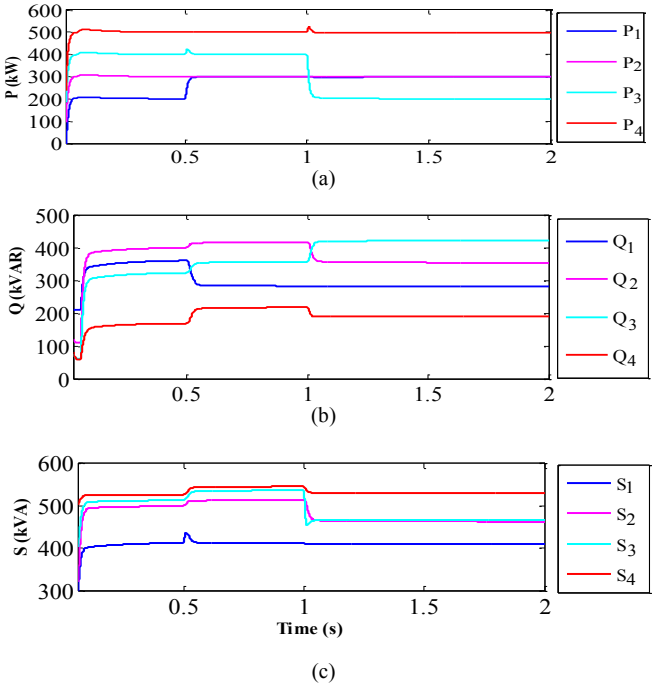

Fig.10. Results with proposed algorithm (a)active power fed by DGs, (b) reactive power shared by the inverters, (c)apparent power of each inverter

TABLE IX
UTILIZATION FACTOR OF EACH DG FOR PROPOSED ALGORITHM

Time Interval(s)	P_i (kW)	Q_{iref} (kVAR)	S_i (kVA)	Uti. Fac. S_i/S_{Ni}
t=0-0.5	200	346	399	0.99
	300	388	500	0.98
	400	310	500	0.83
	500	154	520	0.74
t=0.5-1	300	265	399	0.99
	300	400	500	0.99
	400	338	523	0.87
	500	197	537	0.76
t=1-2	300	265	399	0.99
	300	344	450	0.90
	200	412	450	0.75
	500	179	500	0.75

V. CONCLUSION

In case of renewable energy source (PV or wind) based DG, the reactive power that it can supply varies as the active power supplied by it changes. The conventional algorithm, which relies on the sharing of equal reactive power amongst the inverters, fails under such case. Not only the inverter gets overloaded but also the distribution of the total apparent power amongst the inverters vary greatly leading to uneven percentage utilization of the inverters. The optimal reactive algorithm also suffers from similar drawbacks. It is observed that the proposed algorithm maintains operation of all inverters within their nominal ratings and yet they are able to match the total reactive power demand of the load. As the reactive power assigned to the inverters is linked with the available reactive power capabilities, the inverter that supplies lesser active power is controlled to share a greater amount of reactive power. If the DG inverters have equal kVA ratings, then with the proposed algorithm, not only the apparent power sharing is better than other algorithms but the utilization factors of the inverters are also nearly similar. However, as the algorithm tries to share the apparent power equally amongst the inverters, the utilization factors are not the same for the inverters of unequal kVA ratings. But the algorithm always operates to minimize the miss-match in the utilization factors. Hence, with the proposed approach, comparatively better apparent power sharing is observed leading to reduction in the variation of percentage utilization of the inverters.

REFERENCES

[1] Y. Huang, F. Z. Peng, J. Wang and D. Yoo "Survey of power conditioning system for PV power generation*," Power Electronics Specialist Conference,* PESC 2006, pp.1-6, June 2006.

[2] Y. Riffonneau, S. Bacha, F. Barruel, and S. Ploix "Optimal power flow management for grid connected PV systems with batteries" *IEEE Trans. Sustainable energy*, vol. 2, no. 3, pp.309-320 July 2011.

[3] R. H. Lasseter and P. Paigi, "Microgrid: A conceptual solution," presented at the *IEEE Power Electron. Spec. Conf*. Aachen, Germany, 2004.

[4] N. Eghtedarpour and E. Farjah, "Power control and management ina hybrid AC/DC microgrid," *IEEE Trans. Smart Grid*, vol. 5, no. 3,pp. 1494–1505, May 2014.

[5] C.T. Lee, C.C. Chu, and P.T. Cheng, "A new droop control method for the autonomous operation of distributed energy resource s interface converters," *IEEE Trans. Power Electron.*, vol. 28, no. 4, pp. 1980–1993, April 2013.

[6] Q. Zhong, "Robust Droop Controller for Accurate Proportional Load Sharing Among Inverters Operated in Parallel," *IEEE Trans. Ind. Electronics,* vol. 60, no. 4, pp. 3747-3459, April 2013.

[7] I. U. Nutkani, P. C. Loh, and F. Blaabjerg, "Droop scheme with considering of operating cost," *IEEE Trans. Power Electron.*, vol. 29, no. 3,pp. 1047–1052, March 2014.

[8] A. Bidram and A. Davoudi, "Hierarchical structure of microgrids control system," *IEEE Trans. Smart Grid*, vol. 3, no. 4, pp. 1963–1976, December 2012.

[9] J. He, and Y Li" An accurate reactive power sharing control strategy for DG units in a microgrid" 8th International Conference on Power Electronics - ECCE Asia,the Shilla Jeju, Korea. May 30-June 3, 2011.

[10] A. Milczarek, *M. Malinowski and* J. M. Guerrero*"* Reactive power management in islanded microgrid—proportional power sharing in hierarchical droop control" *IEEE Trans. Smart grid,* vol. 6, no. 4, pp. 1631-1638, July 2015.

[11] K. Turitsyn, PetrS˙ulc , S. Backhaus, and M. Chertkov " Options for control of reactive power by distributed photovoltaic generators" Proceedings of the IEEE, vol. 99, No. 6,pp 1063-1073, June 2011.

[12] F. Olivier, P. Aristidou, D. Ernst, and T. V. Cutsem, "Active management of low-voltage networks for mitigating over voltages due to photovoltaic units" *IEEE Trans. Smart grid,* vol. 7, NO. 2, pp. 926-93, March 2016.

[13] A. Micallef, *M. Apap, J. M. Guerrero, and J. C. Vasquez,"* Reactive power sharing and voltage harmonic distortion compensation of droop controlled single phase islanded microgrids" *IEEE Trans. Smart grid,* vol. 5, no. 3, pp. 1149-1158, May 2014.

[14] S. Duan, Y. Meng, J. Xiong, Y. Kang and J. Chen. "Parallel operationc techqnique of voltage source inverters in UPS," IEEE International Conference on Power Electronics and Drive Systems, , Hong Kong, 883 –887, PEDS'99.

[15] Z.Wang. K.M.,Passino, J.Wang, "Optimal reactive power allocation in large scale grid connected photovoltaic system", Journal of optimization theory and application, November 2015.

[16] A. Micallef, M. Apap and C. SpiteriStaines, J. M. Guerrero Zapata" Secondary control for reactive power sharing and voltage amplitude restoration in droop-controlled islanded microGrids " 3rd IEEE International Symposium on Power Electronics for Distributed Generation Systems (PEDG) 2012.

[17] T. L. Vandoorn, B. Renders, L. Degroote, B. Meersman, and L. Vandevelde, "Controllable harmonic current sharing in islanded microgrids: DG units with programmable resistive behavior toward harmonics, "*IEEE Trans. Power Del.,* vol. 27, no. 3, pp. 1405–1414,July 2012.

[18] Adhikari and Fangxing Li, "Coordinated V-f and P-Q control of solar photovoltaic generators with MPPT and battery storage in microgrids" *IEEE trans. on smart grid*, vol. 5, no. 3,pp 1270-1281,May 2014.

[19] H. Mahmood,, *D. Michaelson, and J. Jiang, "*Accurate reactive power sharing in an islanded microgrid using adaptive virtual impedances" *IEEE Tran. Power electron*.vol. 30, no. 3, pp. 1605-1617,March 2015.

[20] J. W. Smith, W. Sunderman, R. Dugan, Brian Seal, "Smart inverter Volt/Var control functions for high penetration of PV on distribution Systems "Power system conference and Exposition (PACE) 2011..

Urvi Patel received B.E degree in electrical engineering from the S.V. Regional College of Engineering and Technology (now S.V. National Institute of Technology), South Gujarat University, Surat, India, in 2000, and the M.E. degree in Electrical engineering in 2009 from the M. S. University, Baroda, India

She is currently working as an Assistant Professor in the Department of Electrical Engineering at C. K. Pithawalla College of Engineering and Technology, Surat and pursuing Ph.D. in electrical engineering. Her current research interests include distributed generation, renewable energy and microgrid issues. She is a Life Member of the Indian Society for Technical Education and a member of IEEE.

Hiren Patel received the B.E. degree in electrical engineering from the S.V. Regional College of Engineering and Technology (now S.V. National Institute of Technology), South Gujarat University, Surat, India, in 1996, and M. Tech. in energy systems and PhD in Electrical Engineering degree from the Indian Institute of Technology Bombay (IITB), Mumbai, India in 2003 and 2009, respectively. He is working as a Professor and Dean, R&D at the Sarvajanik College of Engineering and Technology, Surat.

His current research interests include computer aided simulation techniques, distributed generation, and renewable energy, especially energy extraction from photovoltaic arrays. He has to his name several publications in international and national journals and conferences. He is a Life Member of the Indian Society for Technical Education and the Institute of Engineers.

Towards a High Reliable Enforcement of Safety Regulations - A Workflow Meta Data Model and Probabilistic Failure Management Approach

Heiko Thimm

***Abstract*—Today's companies are able to automate the enforcement of Environmental, Health and Safety (EH&S) duties through the use of workflow management technology. This approach requires to specify activities that are combined to workflow models for EH&S enforcement duties. In order to meet given safety regulations these activities are to be completed correctly and within given deadlines. Otherwise, activity failures emerge which may lead to breaches against safety regulations. A novel domain-specific workflow meta data model is proposed. The model enables a system to detect and predict activity failures through the use of data about the company, failure statistics, and activity proxies. Since the detection and prediction methods are based on the evaluation of constraints specified on EH&S regulations, a system approach is proposed that builds on the integration of a Workflow Management System (WMS) with an EH&S Compliance Information System. Main principles of the failure detection and prediction are described. For EH&S managers the system shall provide insights into the current failure situation. This can help to prevent and mitigate critical situations such as safety enforcement measures that are behind their deadlines. As a result a more reliable enforcement of safety regulations can be achieved.**

Keywords— Environmental Health and Safety, workflow management, workflows, failure detection, failure prediction;

I. INTRODUCTION

Multiple legal authorities with different responsibility levels obligate companies to follow environmental, health, and safety (EH&S) regulations [1] [2]. Due to the enormous size of this ever growing and frequently revised set of EH&S regulations companies are required to establish an efficient and an effective practice for the enforcement of new regulations and of revisions of existing regulations [3]. Ideally, this enforcement duty is performed trough carefully selected measures such as employee instruction and training, the use of additional safety devices and facilities, and even product revisions in order to reduce the potential of harm [3].

Although there exists a great awareness about the need for a reliable and effective EH&S enforcement practice, often in companies deficiencies can be found in this area [4] [5]. The organizational deficiencies and inappropriate use of Information and Communication Technology (ICT) can create substantial EH&S risks and losses in efficiency and effectiveness. That the use of a Workflow Management System (WMS) [6] will lead to a reliable, effective, and efficient EH&S enforcement in companies seems to be a promising approach.

Traditional WMS are designed to enact and manage the execution of workflow instances according to given workflow models. Typically, the system notifies participants about assigned activities and provides access to information artifacts. However, traditional WMS are not designed to cope with problems that can occur in the context of the enforcement of EH&S regulations. This can lead to an unreliable enforcement of these regulations (i.e. non-compliance) because of activity failures within the execution of EH&S enforcement workflows. As a result critical situations can happen in which the company is threatened by financial losses, by health risks for humans, and by risks for damages to the environment. Activity failures can emerge due to a variety of different reasons. First of all, activity failures can be men made. For example, individuals who are expected to complete EH&S activities can be over-challenged by what is demanded from them. They can also be insufficiently experienced/qualified or suffer from human factors. Activity failures can also be caused by problems inherent to group work such as a bad group atmosphere and group thinks effects. Malfunctioning and defects of components of the corporate technical infrastructure also have to be considered as potential sources for activity failures.

The reliability of EH&S workflow completions can significantly be improved through the use of a WMS that is capable to detect in realtime activity failures that occurred already or that are likely to occur (i.e. prediction) in the near future. Such an enhanced system approach can help companies to prevent and/or mitigate the potential harm resulting from the failures. This consideration presents the overall research objective of the project described in this article. The research is part of a broader project that investigates the integrated use of both WMS and EH&S Compliance Information Systems in order to improve reliability of EH&S regulation enforcement. The focus of the article is on the foundation of this integrated approach which is a domain-specific workflow management meta data model. The modelling concepts of this model are specialized to the detection and prediction of activity failures. The modeling concepts are directed at the company specific organizational context, failure statistics, and proxy templates for real world activities. In the article the modelling concepts are exemplified through a concrete workflow example. Furthermore, an overview of prototypical implementation is presented.

The remainder is organized as follows. An overview of related work is contained in Section 2. The domain-specific meta data model is described in Section 3. Examples of some major modeling concepts of the model are presented in Section 4.

Section 5 describes the main principles of the detection and prediction of activity failures and Section 6 gives an overview of a prototypical implementation. Concluding remarks are contained Section 7.

II. RELATED WORK

In the literature several projects are described that target the monitoring of workflows in order to detect compliance violations [7] [8]. An overview of the work in this field is given in [9]. It seems however that the core issue investigated in our research which is the prediction of workflow activity failures - that may lead to compliance violations - has not been addressed before.

Domain specific modelling has gained considerable attention in the research community. Recommendations about when and how to develop domain-specific languages are given by Mernik et al. [10]. An example of such a language is the extended Compliance Rule Graph (eCRG) language [11]. An overview of domain-specific extensions of the popular BPMN modelling notation is contained in [12]. Several research teams proposed domain-specific extensions for process modelling including extensions for the modelling of clinical pathways in the healthcare domain [13] and extensions to capture specific process requirements of the maintenance management domain [14]. Conformance validation through traditional database technology has been the subject of several research teams. Snodgrass et al. proposed to store additional information in the database in order to enable a separate audit log validator [15]. Another approach is the use of Event-Condition-Action Rules. Experience with this approach for support of clinical protocols is reported in [16]. Various rule-based approaches addressing process monitoring and failure detection have been proposed. The REALM approach developed by IBM Research [17] is especially directed at compliance automation. Regulations are first expressed based on logical models and then automatically mapped into processible rules.

A comprehensive survey of online failure prediction methods and a proposal of a respective taxonomy is given in an article of a research group from the Humboldt University in Berlin [4]. In general, the failure prediction method of our work belongs to the so-called 'classifiers' that are one of several specializations of the so-called 'symptom monitoring approaches'. The classifier approaches evaluate values of system variables directly in order to classify whether the current situation is failure-prone or not. For our system approach a more refined classification scheme has been devised with the categories 'non-failure-prone', 'failure-prone', and 'highly failure-prone'.

III. DOMAIN SPECIFIC WORKFLOW META DATA MODEL FOR THE DETECTION OF ACTIVITY FAILURES

Companies are often advised to address EH&S regulations by establishing a corresponding management system according to the international norm ISO 14001 [18]. A set of clearly defined processes that are oriented at a set of goals such as compliance to EH&S regulations serves as foundation of many management systems. The focus of the research reported in this article is on ICT-supported processes to enforce EH&S obligations. In particular the research is focused on three EH&S obligations that require the existence of an EH&S Regulation Management Database referred in the following by RM-DB [3]. The three obligations are: 1. the obligation to systematically establish and maintain a central registry of relevant regulations as a part of the RM-DB, 2. the obligation to carefully complete routine regulation management activities according to defined procedures (e.g. business processes and workflows, respectively), and 3. the obligation to record regulation management specific information in the RM-DB. This documentation obligation includes the recording of context information and status information about workflow activities as well as results of completed activities. A main reason for this documentation task is that through logging of activities valuable persistent data is established. This data is of high importance when internal and external EH&S audits are performed.

The above mentioned three central EH&S obligations require from companies to frequently perform EH&S regulation enforcement activities. A correct and careful completion of these activities requires to observe context-specific aspects such as specific organizational characteristics of the company (e.g. number of organizational units and decision boards). Another context-specific aspect concerns the set of relevant regulation areas (e.g. occupational safety, waste, fire, air pollution, chemical, transportation safety).

Only in an ideal world never will required activities be missed and never will they fail the required outcome. For the non-ideal real world, however, one has to consider the possibility that actually required activities will not take place and that executing activities will not lead to the required outcome. We generally refer to such situations by activity failures which may tamper an organization's efforts to enforce safety regulations with utmost reliability.

A workflow management meta data model is proposed that is specialized on the above EH&S obligations. The meta data model is directed especially at activity failures. The model considers activity failures that may occur when EH&S workflows are performed. The model is intended to serve as a foundation of an approach to detect already occurred activity failures and to predict activity failures that are likely to occur.

A concept diagram of the meta data model given in the popular Martin Notation [19] is shown in Figure 1. The boxes denote real world phenomena of the universe of discourse that possess an identity of their own. The semantic relations between the modelled phenomena are denoted by labelled edges. The concepts at the top of Figure 1 address the company specific EH&S context. The concepts at the middle layer are oriented at template data defined by modelers at workflow modelling time. The concepts at the bottom are directed at monitoring data about executing activities and also failure tracking data. One can envision that the concrete instances of the concept of Activity are created (i.e. instantiated) from the corresponding activity templates (i.e. Activity Type). The activity instances serve as proxies for real world activities that are controlled and monitored for example on the basis of a WMS.

Concepts for company-specific context data. The top part of the model in Figure 1 models the EH&S specific company context. The concepts Regulation Area, Organizational Unit,

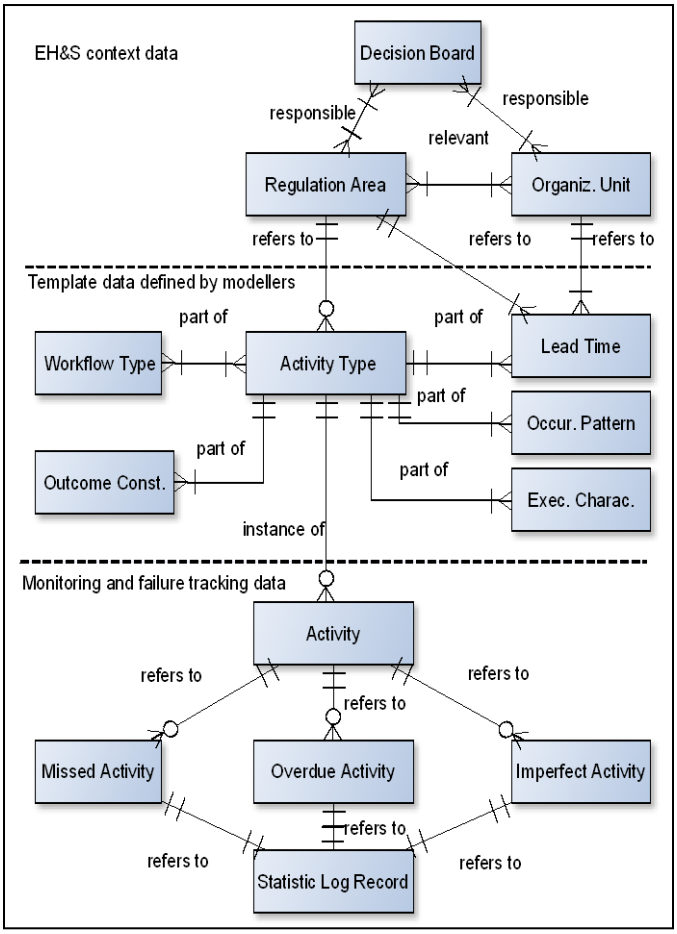

Fig. 1. Proposed workflow meta data model.

and Decision Board are addressed. That companies are usually structured into different organizational units for which different sets of the regulation areas are relevant is the first intention addressed by these concepts. The second intention is to reflect that for each relevant regulation area of an organizational unit one may assign an individual set of decision boards that are responsible for decisions in the given area. For example, the decision boards might be responsible for the selection of measures to enforce EH&S regulations [20]. One of the motivation for data modelling of the EH&S specific company context is that the data can be used to obtain indicators about the complexity of activities. It is possible to obtain from these indicators lead times of activities that are useful for failure management.

Concepts for template data defined by workflow modelers. Similar to other workflow data models the proposed model considers the concepts Workflow Type and Activity Type that serve as templates for concrete workflows and activities. That in companies with a good EH&S practice a set of pre-specified types of workflows and a set of corresponding types of activities are specified is the intention of these modelling constructs. Several modelling concepts are considered in order to model specific details of activity types as concepts of their own. The construct Occurrence Pattern reflects the occurrence characteristics of activities such as if the activity is repeatedly executed during a given time period or if the activity is triggered by a specific events. The concept Execution Characteristics reflects the execution characteristics of activities such as if the activity is completed iteratively in several steps or in an all in one approach. The concept Outcome Constraint refers to the set of conditions by which the completeness and correctness of the activity result can be validated. For most of the activities these conditions specify the set of data values to be contained in the RM-DB. The Lead Time concept is oriented at lead time specifications (i.e. minimum, average, and maximum lead time) per type of activity. Note that every lead time specification refers exactly to one particular regulation area and one particular organizational unit. Through this specification it is possible to check if given activity deadlines are met.

The specification of the lead time of an EH&S activity in the form of an educated guess requires to consider three activity-specific aspects: 1. the type of regulation area that the activity deals with, 2. the characteristics of the business activity of the referred organizational unit (e.g. is hazardous material involved in manufacturing processes), and 3. the number of involved decision boards. Consequently, per activity type a set of variants with individual lead times is considered. Every variant is associated with an individual combination of regulation areas and organizational units.

Concepts for monitoring data and failure tracking data. The concept Activity stands for activities that are performed according to the referring Activity Type. Failures that already occurred during the activity completion and failures that are likely to occur are addressed through the following three modelling concepts. The concept of Missed Activity is oriented at activity failures that emerge when an activity that is required according to its occurrence pattern has not been considered until the given deadline. That is, not even a corresponding activity instance has been created. The concept of Overdue Activity refers to individual activity instances that have been initiated according to their occurrence pattern but that missed their deadline (already). In addition, activity instances are also treated as overdue activities when these activities are likely to miss their deadline. The concept of Imperfect Activity refers to initiated activity instances that fail to meet the set of outcome constraints at the given deadline. The Statistic Log Record models a comprehensive event log about detected and predicted activity failures. The event log also contains accumulated statistical data such as the failure frequencies for the various different activity types.

IV. Exemplification of the Meta Model

Workflows models in general correspond to formal or semiformal specifications of a set of activities that serve the goal to partially or completely automate business processes [6]. To this end workflow specifications result from a refinement of business processes in terms of concrete activities and of the dependencies between activities such as temporal dependencies and input/output dependencies. The work flow specifications of our research are extended by domain-specific data, i.e. data specific to the domain of EH&S enforcement management. It is the target of this extension to establish a data foundation for the detection and prediction of missed activities, overdue activities, and imperfect activities that constitute activity failures as described above. The acquisition of the domain-specific data, for

example, can be performed by a corresponding extension of the tracking and logging system component of a WMS.

On the basis of the proposed meta data model, it is possible to complement information about completed and still executing workflows and activities by further data. It is possible to use the resulting rich data in order to detect occurred activity failures and to predict activity failures. By executing proper counter-acting measures to mitigate and compensate the activity failures, it is possible to enforce EH&S regulations with a high reliability.

For the now following description of sample data for activity failure detection and prediction an essential regulation enforcement process is considered. In accordance with its main objective this considered process is sometimes referred by New Regulation Management (NRM) process [3]. The main tasks of the NRM process are: 1. to ensure that new regulations which are potentially relevant for the company are recognized, 2. to evaluate new regulations in terms of the company specific relevance, and 3. to accordingly enforce new regulations through a careful selection and implementation of proper measures. Like for all processes in the field of EH&S regulation management it is also a major task of the NRM process to comprehensively document the actions and the progress.

From industry partners we learnt that workflow modelers are advised to establish an NRM workflow that is composed of six activities [3]. These subsequent activities are:

A1: Monitor, filter, and capture new regulation. The relevant information channels (e.g. EH&S information services) of the EH&S rule setters are monitored. The announcements that pass a first rough relevance check are registered in the RM-DB.

A2: Judge the regulation relevance for the company. An evaluator judges the relevance of a new regulation for the company by assigning a relevance category to the regulation.

A3: Specify decision schedule for enforcement measures. When a new relevant regulation that requires enforcement measures is observed then a plan is defined for (collaborative) decisions about the set of required measures. Among others, one needs to specify who is in charge of the decision and when is the deadline of the decision.

A4: Organize and complete measure decision(s). A decision manager organizes and controls the completion of the decision plan.

A5: Implement set of measures. An implementation manager organizes and controls the implementation of the set of measures according to the given implementation plan.

A6: Evaluate effectiveness of measures. A reviewer checks the effectiveness of the implemented set of measures. When the review result meets given success criteria then a confirmation entry is made in the RM-DB. Otherwise, another workflow is initiated in order to deal with the problem of the failing measures.

When no new announcement of a new regulation was detected for a certain monitoring period – for example a calendar month – then only a very short version of the workflow is executed. The short version consists of the monitoring action of activity A1, the "closing" of the monitoring period, and the documentation that no new announcement was detected during the closed monitoring period. Through this approach a coherent and traceable activity documentation for all monitoring periods is established.

Recall from earlier that the proposed meta data model contains specific concepts to model company-specific context data. The modelled context data can be used to determine the complexity of workflow activities. Based on this complexity data and further data about executing workflows one can predict if activity failures are likely to occur.

The sample data used to demonstrate company-specific context data correspond to the specific characteristics of a real company referred by the fictive name CExperts [3]. For competitive reasons the real name of the company behind CExperts is not disclosed in this article. The company is a globally acting German mid-sized manufacturer of industrial alcohol, chemicals, and polymer with two different production sites in Germany. The EH&S workflows of CExperts are directed at 10 regulation areas that include water, occupational safety, waste, fire, radiation, and chemical. In the end of year 2015 the total body of regulations stored in CExperts' corporate RM-DB comprised roughly 2000 regulations in these 10 areas from several different rule setters at all different levels (world, world region, country, state, community). Because, CExperts develops among others special chemical substances the potential enforcement measures include a) product revisions, b) infrastructure and compound revisions, c) manufacturing process revisions, d) workforce trainings and education, e) workforce instructions, f) workforce information. The EH&S organization of CExperts needs to deal with three different corporate organizational units. Every unit is assigned to each of its relevant regulation areas a set of four decision boards. The people of these four decision boards possess complementary expertise in the fields of product management, logistics and transportation, occupational safety, and quality management.

Of the above described activities of the NRM process for three activities sample template specifications are given and are explained in the following. According to our meta data model these templates result from a business process modelling and workflow specification activity. A modelling environment such as the open source environment Camunda BPM [21] which is able to derive processible workflow specifications from graphical process models can ease this activity. Since the sample templates are intended to exemplify the meta data model in the following the specifications are stated in verbal form. The data values in these verbal specifications reflect the specific characteristics of the sample company CExperts. Obviously, in a system implementation the verbal explanations are replaced by respective predefined and thus machine processible codes.

Table 1 contains the specification data for activity A1 (i.e. monitor, filter and capture new regulations) of the NRM process. The specification data of the occurrence pattern describes the conditions that trigger the execution of activity A1. As given by the sample data activity A1 is triggered when a new regulation announcement is recognized. The execution characteristics state that the activity is typically performed in a single step that requires only little time. That upon completion of activity A1 the RM-DB has to contain a description of the new regulation is

specified by the outcome constraint. A general rule for the deadline of activity A1 is specified by the deadline component. The lead times specification data correspond to the minimum, the average, and the maximum lead time of activity A1.

TABLE I. DETAILS OF ACTIVITY A1- MONITOR, FILTER, AND CAPTURE NEW REGULATION.

Concept	Specification data
Occurrence pattern	Activity is started by an individual NRM workflow that is triggered by a new regulation.
Execution characteristics	Execution is typically performed in a single step that only requires a negligible duration.
Outcome constraint	RM-DB contains a description of the new regulation including the deadline for the relevance evaluation performed in activity A2.
Deadline	Activity completion is required within one day.
Lead Times	All regulation areas: 1/1/1

In Table 2 and Table 3 the template data for the activity A3 and A4 are given, respectively. The interpretation of the specification data is strait forward and thus not explicitly described in this article.

TABLE II. DETAILS OF ACTIVITY A3- SPECIFY DECISION SCHEDULE CONCERNING ENFORCEMENT MEASURES.

Concept	Specification Data
Occurrence pattern	Activity is triggered by a preceding activity A2 when measures are required to enforce a new relevant regulation.
Execution characteristics	Execution is typically performed in several steps that require non-negligible durations. The larger the number of organizational units the more complex the decision schedule to be defined and the larger the time demand.
Outcome constraint	The decision schedule that can be composed of a set of sub-decisions is fully described in the RM-DB.
Deadline	Completion is required within 3 days after the new regulation has been registered
Lead Times	All regulation areas: 1/3/5

TABLE III. DETAILS OF ACTIVITY A4 – ORGANIZE AND COMPLETE MEASURE DECISION(S).

Concept	Specification data
Occurrence pattern	Activity is triggered by a preceding activity A3.
Execution characteristics	Execution is typically performed in several steps that require a substantial duration. The more complex the decision schedule the more time is needed to complete the activity.
Outcome constraint	The decision results (i.e. measures) are fully described in the RM-DB.
Deadline	Completion deadline is given by the decision schedule.
Lead Times	Water: 4/8/15; Safety: 6/10/18; Chemical: 10/21/34

V. PROBABILISTIC FAILURE MANAGEMENT APPROACH

Today's workflow management systems (WMS) usually perform many tasks in order to execute workflows according to specifications given in the form of workflow models. This includes that for new workflow instances to be executed in the physical world, internal workflow proxy objects are created and maintained [6]. A specific WMS component referred to by "Workflow Engine" usually performs these runtime proxy management tasks. The corresponding workflow models are specified through the use of a workflow modelling environment that is often an integrated component of WMS.

Every proxy object represents and mirrors a referring real world workflow. Similarly, workflow engines instantiate and maintain activity proxy objects for the constituent real world activities of workflows. In order to enforce that the execution of workflows and activities conforms to the referring workflow models, WMS track workflows and activities in realtime and maintain a corresponding data log.

In the following it is described how the proposed workflow meta data model can be used for a new approach to predict and to detect failures of executing safety enforcement workflows. This approach draws on an extension of the traditional workflow management data log by failure management specific data items as considered in the workflow meta data model. Based on the extended logging data, a system instance is able to obtain the current failure status of ongoing workflows. The following Section A gives an overview of the major principles of the proposed approach. The major considerations for the detection and prediction of activity failures are described in Section B. Section C contains a brief scientific evaluation of the proposed approach.

A. Major Principles

In general, the capabilities of WMS to support workflow modeling and runtime execution management of proxy objects are based on a corresponding meta data workflow model. The majority of the existing workflow meta data models do not address domain specific concepts because WMS are primarily developed as general purpose systems. As opposed to that, the proposed failure management approach builds on a WMS that uses the workflow meta data model described above. That is, the concepts of the meta data model serve as basis for the specification of workflow models by the users and also for the runtime management of proxy objects (workflow instances and activity instances) by the workflow engine.

The major principles of the failure detection and prediction approach are illustrated in Figure 2. For every activity proxy object that refers to an enforcement activity, there is a comprehensive data set for failure detection and prediction supplied by the corresponding activity template. Additionally, EH&S context data specified by the workflow modeler is considered for failure detection and prediction. Also used are the statistic failure data and further logging data that are continuously maintained by the WMS. The three types of activity failures addressed in the meta data workflow model (i.e. missed activities, overdue activities, and imperfect activities) are

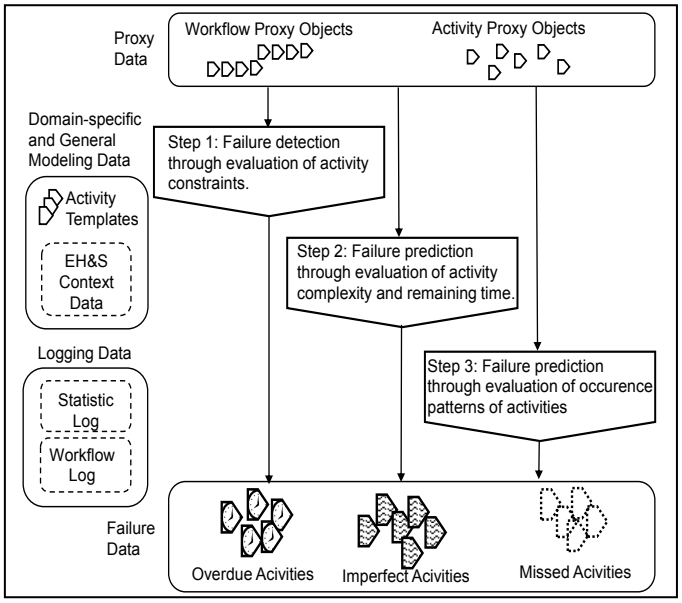

Fig. 2. Principles of failure detection and prediction approach.

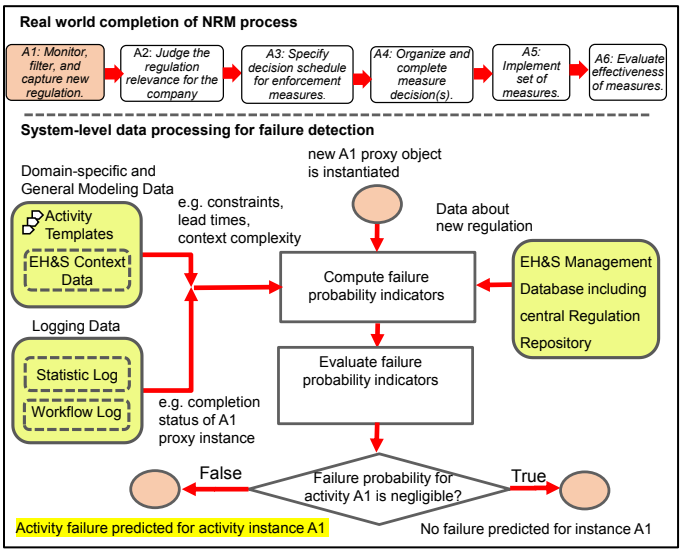

Fig. 3. Prediction of overdue activities and imperfect activities.

the target of the processing steps shown in Figure 2. In the next section these steps are described in more detail. The failures that are identified in the steps are indicated in the form of activity failure objects.

B. Detection and Prediction of Activity Failures

The three processing steps that are shown in Figure 2 are oriented at activity failures. Step one targets the detection of occurred (i.e. evident) failures that are imperfect activities and overdue activities. The failures are detected by evaluating the constraints that are specified in the activity templates. Obviously, the individual data available at runtime for every activity proxy are used for a corresponding constraint check. To give a concrete example, consider the above specification of the NRM process's activity A1 (*A1: Monitor, filter, and capture new regulation)*. The outcome constraint requires that a description of the new regulation has to be available when the activity is finished. When this constraint is not met, an activity failure of type imperfect activity needs to be handled. Similarly, by a comparison of corresponding proxy data with the individual activity deadline, it is possible to obtain activity failures that are overdue activities. Note that the individual activity deadlines are computed from the generally specified deadline constraint of the referring activity template.

It is the goal of step two to make use of available modelling data and runtime data in order to predict activity failures. In particular, the prediction step targets activity failures that did not yet occur but that are expected to happen in the future when no attention is paid to the potential failure cause. Figure 3 gives a high-level overview of step two using activity A1 of the workflow described in Section 4 as an example.

At first a corresponding proxy object for activity A1 is instantiated. Next, the set of failure probability indicators for the proxy object is computed based on data generally defined in the indicator formulas using the corresponding current data values. This data includes modeling data of the relevant activity template such as the deadline, the complexity, and the lead times. Also logging data such as the completion status of the activity and data about new EH&S regulations are processed in order to obtain the failure probability indicators. The use of the complexity indicators reflects the general fact that usually there exists a direct positive correlation between an activity's complexity and the likelihood of activity failures. Moreover, also taken into account by the failure prediction methods are actual failure statistic data and data about the current status of the activities.

The obtained failure probability indicators serve as basis for a decision step that follows next. In general, in this next step it is focused on two questions: 1. How likely is it that the activity will be completed until the given deadline? 2. How likely is it that the results expected from the activity will be achieved? In the decision step, based on the failure probability indicators, a qualitative prediction measure is obtained. This measure determines whether an activity failure for the investigated activity instance has to be considered or not.

The activity failures that are predicted by the methods may either correspond to an overdue activity or an imperfect activity. An overdue activity is predicted when the given deadline will most likely be failed by the activity. When it is likely that the activity will not fulfill the specified outcome constraints, then an imperfect activity will be predicted.

Also in the third step a prediction of activity failures is performed targeting failures that are missed activities. The prediction method for missed activities makes use of the occurrence pattern and execution characteristics that are supplied by the activity templates. It is checked if the specified pattern and execution characteristics imply the existence of an activity. Recall that these activities correspond to real world activities that are expected to be performed. In turn, it is checked if a corresponding activity proxy object exists, indeed. When two conditions hold true, 1. no proxy object is found and 2. the

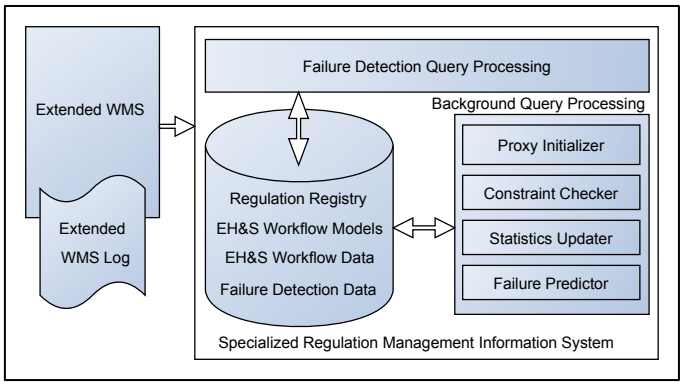

Fig. 4. High-level architecture of prototype.

temporal conditions of the activity and the workflow require the activity to be started, then a missed activity is predicted.

C. *An Initial Evaluation*

To our knowledge the approach to use a meta data workflow model that is specialized on failure detection and failure prediction in the domain of EH&S workflows is a new approach. In the next section it is described how this approach can be implemented leading to an integrated information system solution. The implementation of a corresponding research prototype is an ongoing project. It is planned to use the resulting prototype for comprehensive evaluation studies with the real world data of CExperts described in this work. The lab studies will provide validation data for our approach and insights about possibilities for improvement. Looking at the "bigger picture" of our approach, one can already at this early research phase state, that the proposed solution bears promising potential to improve the reliability of safety regulation enforcing workflows. The enforcement workflows are actively monitored with respect to their temporal constraints and outcome constraints. Also, the proposed solution provides the capability to detect missing workflows. When occurred failures are detected and failures that are likely to occur are predicted, corresponding failure data is made available for further failure handling actions. One can consider especially the failure handling action to actively provide users with alerts, failure data, and background data to effectively cope with the situation. It can be expected that this kind of active assistance being offered to safety managers for coping with failures in EH&S management tasks will promote reliability of regulation enforcement tasks.

VI. Prototype Implementation

A research prototype to demonstrate and evaluate the above probabilistic failure management approach has been devised. The prototype builds on an integrated information system that combines an extended WMS with a specialized Regulation Management Information System (RM-IS). The extension of the WMS concerns the support of workflow models that are augmented with detailed failure management data such as outcome constraints, occurrence patterns, and execution characteristics of activities. The RM-IS is specialized towards the processing and storage of failure monitoring and tracking data such as data about missed activities and overdue activities.

Figure 4 illustrates the high-level architecture of the prototype. The database stores among other data the Regulation Registry with all regulations and corresponding relevance information, the EH&S workflow models (i.e. templates for workflow instances), data about ongoing and completed workflow instances and activity proxies, and data for the detection of activity failures that already occurred or that are likely to occur in the near future. Failure detection query processing against the database is performed on request by interactive users who perform ad hoc queries. Additionally, this query processing is also triggered by scheduled query batch jobs such as the generation of failure reports.

In order to further clarify the notion of "extended WMS" consider that today's WMS usually maintain an online log in order to track the states of ongoing workflows [19] in realtime. Based on the status information, the WMS determines and manages actions such as requests for completion of activities that are issued to workflow actors. For our approach, an extended WMS is envisioned that performs a very fine grained logging of both, workflows and workflow activities, as specified in the workflow meta data model. Especially, it is assumed that the begin time and completion time of every activity is logged through corresponding time stamps.

The architectural model defines four components that periodically update database objects for failure management purposes. The *Proxy Initializer* assigns to each new created activity proxy the corresponding set of initial values such as the individual activity deadline, the appropriate lead time values, and failure probabilities. Note that these initial values are copied from the respective activity type. The *Constraint Checker* checks the set of outcome constraints of activity proxies and reports the result in the respective activity property (oc_passed). The query set of a proxy that specifies the outcome constraints is executed until one of the following two termination conditions is reached. 1. When all outcome constraints are satisfied (i.e. all queries result to true), then the checking task is completed. 2. When the activity is completed and the query set was executed one more time after the activity completion, then the checking task is finished, too. The *Statistics Updater* component maintains data about failures stored in a failure occurrence log. The component also computes from this log statistical failure data in order to keep the corresponding attribute values of activity types up-to-date. That is, the *Statistics Updater* periodically updates the database with the latest statistical data about failures. This updating ("learning") mechanism contributes to a proper degree of precision of predicted activity failures.

At the level of activity instances, failure prediction is performed based on a symptom monitoring approach [4]. A set of activity-type specific indicators is periodically evaluated in order to classify whether the current activity execution status is 'non-failure-prone', 'failure-prone', or 'highly failure-prone'. The indicators include failure statistical data stored at the respective activity type (e.g. failure history) and relevant facts about the activity instance such as the complexity of the activity and the tightness of timing constraints. The resulting classification

decision is reported in the respective activity instance's attributes (p_iact, p_oact, and p_mact) with values 'unlikely', 'likely', or 'highly likely'. The processing according to these principles is performed by the component *Failure Predictor*. Note when a new activity instance is created the failure probability failures are copied from the respective activity type. These values are periodically updated in every processing cycle of the *Failure Predictor* in order to reflect the evolving individual execution situation of the activity instance.

In a first implementation step the RM-IS has been implemented. The interfacing of the developed RM-IS with the extended WMS is simulated through corresponding data files. So far, the use of traditional relational database technology for the prototype implementation did not lead to any "dead ends" or extraordinary "workaround approaches". The latest versions of the popular SQL standard [20] supports language extensions by user-defined concepts such as user-defined data types and user-defined functions. For example, for several properties of EH&S activities user-defined datatypes have been developed according to the workflow meta data model. It is expected that with the further advancement of the demonstrator this SQL extensibility feature will even be more exploited.

The database tables ACTIVITY and FAILURE-LOG-ENTRY that store data about activities and failure monitoring data are described in Table IV and V, respectively. Data about activity failures are stored in the tables FAIL-OVERDUE-ACT, FAIL-IMPERFECT-ACT, and FAIL-MISSED-ACT. The outcome constraints of activities are encoded into SQL queries which evaluate if the database contains all of the data items that are required by the outcome constraints.

In order to give an overview of the proposed approach for the detection and prediction of activity failures, several sample queries are described next. For the graduation of activity failures with respect to the indication of failure occurrence four categories are used. The category "occurred" refers to evident failures that already occurred. Whereas, failure prediction results are classified into the three categories "highly likely", "likely", and "unlikely".

TABLE IV. DATABASE TABLE 'ACTIVITY'

Field	Type	Description
aid	int	Unique identifier of activity
act_type	int	Type of activity (foreign key)
deadline	date	Absolute deadline of activity
lt_min	int	Minimum lead time
lt_avg	int	Average lead time
lt_max	int	Maximum lead time
ts_start	datetime	Time stamp of start of activity
ts_end	datetime	Time stamp of end of activity
oc_passed	bool	Result of outcome constraint check performed by the Constraint Checker
ts_oc_chec	datetime	Time stamp of constraint check
p_iact	char	Probability of imperfect activity with possible values 'unlikely', 'likely', 'highly likely'
p_oact	char	Probability of imperfect activity with possible values 'unlikely', 'likely', 'highly likely'
p_mact	char	Probability of imperfect activity with possible values 'unlikely', 'likely', 'highly likely'

TABLE V. DATABASE TABLE 'FAILURE-LOG-ENTRY'

Field	Type	Description
lid	int	Unique identifier of log entry
ts_entered	datetime	Time stamp of log entry
activity	int	Activity concerned (foreign key)
fail_type	char	Type of failure with possible values overdue, imperfect, missed
fail_occat	char	Occurrence category of failure with possible values 'occurred', 'highly likely', 'likely', 'unlikely'
fc_before	int	No. of failures before the failure
fc_after	int	No. of failures after the failure
fr_before_	int	Failure rate before the failure
fr_after	int	Failure rate after the failure

The following two sample queries are directed at the detection of failures that are overdue activities and imperfect activities, respectively:

```
Select aid, "occurred"
Into FAIL-OVERDUE-ACT
From ACTIVITY
Where NOT ISNULL(ts_end) and ts_end > Deadline;

Select aid, "occurred"
Into FAIL-IMPERFECT-ACT
From ACTIVITY
Where NOT ISNULL(ts_end) and NOT oc_passed;
```

The next two sample queries predict (i.e. search for) activity failures that are highly likely:

```
Select aid, "highly likely"
Into FAIL-OVERDUE-ACT
From ACTIVITY
Where ISNULL(ts_end) and
lt_min > (deadline – Now());

Select aid, "highly likely"
Into FAIL-IMPERFECT-ACT
From ACTIVITY
Where ISNULL(ts_end) and NOT oc_passed and Now() <
deadline and p_iact = "highly likely"
```

The third query checks for overdue activities by selecting activities for which the remaining time is smaller than the minimum lead time. The fourth query predicts highly likely failures that are imperfect activities through respective conditions in the where-clause. Of the set of not yet terminated activities that did not exceed the deadline, those activities are selected, that did not yet pass the outcome constraint check. Recall that the outcome constraints of all currently executing activities are frequently evaluated by the *Constraint Checker* in parallel to the other query processing activities. When all defined constraints are fulfilled, then the Boolean value 'true' is assigned to the property 'oc_passed' of the respective activity instance. The clause 'p_iact = "high likely"' is directed at restricting the selection to activities for which a high failure likelihood was assessed by the *Failure Predictor*.

VII. CONCLUSION

The research being described in this article aims on a new domain-specific approach for the real time detection and prediction of failures of workflow activities. The context of the failures are activities to enforce EH&S regulations. It seems to be possible to achieve a more reliable enforcement of safety regulations through a timely detection and prediction of activity failures including missing activities.

The proposed failure detection methods and failure prediction methods make use of a diverse data set. This data set includes complexity indicators of activities, failure statistic data, and status data about activity proxy objects. The use of company specific organizational context data in order to obtain an indication of the complexity of activities is one of the novel ideas of the proposed approach.

A standalone prototype version of a probabilistic failure detection system is under development that follows the above described approach. The prototypical implementation builds on experience gained with the CCPro system. CCPro is a research prototype of an Environmental Compliance Management Information System [20]. Traditional relational database technology is used for the prototype in order to make sure that the proposed failure detection and prediction approach can easily be adopted by existing EH&S management systems. It appears that through user-defined functions and active capabilities such as triggers, relational database technology offers sufficient support for the implementation of the intended failure detection and failure prediction methods. In the next phase the prototype will be integrated with a WMS that supports the definition of domain-specific modelling concepts such as the YAWL system [22].

REFERENCES

[1] AberdeenGroup, "Compliance Management in Environment, Health and Safety, White Paper 6991," AberdeenGroup, Boston, MA, 2011.

[2] N. Gunningham, "Enforcing Environmental Regulation," *Journal of Environmental Law,* vol. 23, no. 2, pp. 169-201, 2011.

[3] H. Thimm, „IT-Supported Assurance of Environmental Law Compliance in Small and Medium Sized Enterprises," *Int. Journal of Computer and Information Technology,* pp. 297-305, 2015.

[4] J. Petts, "Small and medium sized enterprises and environmental compliance: attitudes among management and non-management," in *Small and medium sized enterprises and the environment*, R. Hillary, Ed., Sheffield, Greenleaf Publishing, 2000, pp. 49-60.

[5] B. Walker, J. Redmond, L. Sheridan, C. Wang and U. Goeft, "Small and medium enterprises and the environment: barriers, drivers, innovation and best practice. A review of the literature," Edith Cowan University, Australia, 2008.

[6] W. Van der Aalst and K. Van Hee, Workflow Management: Models, Methods, and Systems, Cambridge, MA: MIT press, 2004.

[7] M. Weidlich, H. Ziekow, J. Mendling, O. Guenther, M. Weske and N. Desai, "Event-based monitoring of process execution violations," *Proc. Business Process Management (BPM 2011), Clermont-Ferrand, France,* vol. LNCS 6896, pp. 182-198, 2011.

[8] A. Rozinat and W. Van der Aalst, "Conformance Checking of Processes Based on Monitoring Real Behavior," *Inf. Syst.,* vol. 1, pp. 64-95, 2008.

[9] M. Kharbili, A. de Medeiros, S. Stein and W. Van der Aalst, "Business process compliance checking: Current state and future challenges," *Proc. MobIS'08, Saarbrücken, Germany,* pp. 107-113, 2008.

[10] M. Mernik, J. Heering and A. Sloane, "When and How to Develop Domain-Specific Languages," *ACM Computing Surveys,* vol. 37, no. 4, pp. 316-344, 2005.

[11] D. Knuplesch, M. Reichert and A. Kumar, "Visually Monitoring Multiple Perspectives of Business Process Compliance," *Proc. 13th Int. Conference on Business Process Management (BPM 2015), Innsbruck, Austria,* vol. LNCS 9253, pp. 263-279, 2015.

[12] R. Braun and W. Esswein, "Classification of Domain-Specific BPMN Extensions," *Proc. 7th IFIP WG8.1 Working Conference, PoEM 2014, Manchester, UK,* vol. LNBIP197, pp. 42-57, 2014.

[13] R. Braun, H. Schlieter, M. Burwitz and W. Esswein, "Extending a Business Process Modeling Language for Domain-Specific Adaptation in Heathcare," *Proc. 12th Int. Conference Wirtschaftsinformatik (WI2015), Osnabrück, Germany,* pp. 468-481, 2015.

[14] M. Lopez-Campos and A. C. Marquez, "Modelling a Maintenance Management Framework Based on PAS 55 Standard," *Quality and Reliability Engineering International,* vol. 27, no. 6, pp. 805-820, October 2011.

[15] R. Snodgrass, S. Shilong and C. Collberg, "Tamper Detection in Audit Logs," *Proc. 30th VLDB Conference, Toronto, Canada,* pp. 504-515, 2004.

[16] K. Dube, B. Wu and J. Grimson, "Using ECA Rules in Database Systems to support Clinical Protocols," *Proc. Database and Expert Systems Applications (DEXA2002), Aix-en-Provence, France,* vol. LNCS 2453, pp. 226-235, 2002.

[17] C. Giblin, S. Müller und B. Pfitzmann, „From Regulatory Policies to Event Monitoring Rules: Towards Model-Driven Compliance Automation," IBM Rüschlikon, Switzerland, 2006.

[18] International Standards Organization (ISO), *ISO 14001:2015 environmental management system,* 2015.

[19] J. Martin, Information Engineering: Planning & Analysis, Book II, Englewood Cliffs, NJ: Prentice-Hall, 1990.

[20] H. Thimm, "ICT Support for Collaborative Environmental Compliance Management in SMEs - The CCPro Approach," *IEEE Int. Conf. Collaboration Technologies and Systems,* pp. 295-301, 2015.

[21] A. Fernandez, "Camunda BPM Platform Loan Assessment Process Lab," 2013. [Online]. Available: http://fundamentals-of-bpm.org/wp-content/uploads/2013/11/Camunda-BPM-Loan-Assessment-Process-Lab-v1.0.pdf. [Accessed 22 January 2016].

[22] W. van der Aalst, L. Alfred, M. Dumas and A. H. t. Hofstede, "Design and implementation of the YAWL system," in *Advanced Information Systems Engineering*, vol. 3084, Springer, 2004, pp. 142-159.

Heiko Thimm has been a Full Professor for Information Technology and Quantitative Methods since 2008 at the School of Engineering of Pforzheim University in Germany. In 2004 he joined Kiel University of Applied Sciences as a Full Professor for Business Information Systems after working 6 years for Sun Microsystems and SAP, respectively, as IT Solution Architect and System Analyst. From 1991-1998 he was a researcher at the German National Research Centre for Information Technology (GMD) where he was involved in various pioneering Internet and database research projects. He earned a PhD degree from the Technical University in Darmstadt and a MSc degree from New Jersey Institute of Technology both in Computer Science.

In his current research he investigates the use of recent IT technology advancements such as sensor networks, machine learning, and big data approaches for the development of next

generation environmental compliance management and sustainability management information systems. He is especially focusing on supporting corporate environmental compliance and EH&S managers with active and smart assistance systems that are able to provide, among others, risk management information. Prof. Thimm is also involved in various Industry 4.0 / CPPS projects with partners from the German car/automotive manufacturing industry.

A multiperiodal management method at user level for storage systems using artificial neural network forecasts

G. Belli, G. Brusco, A. Burgio, D. Menniti, *Member*, IEEE, A. Pinnarelli, *Member*, IEEE, N. Sorrentino, *Member*, IEEE, and P. Vizza, *Student Member*, IEEE

***Abstract* – The increase of renewable non-programmable production and the necessity to locally self-consume the produced energy led to utilize ever more storage systems. To correctly utilize storage systems, an opportune management method has to be utilized. This paper implements a multi-period management method for storage systems, using different management strategies. The method aims to minimize the total absorbed and supplied energy or the peak power exchanged with the grid. The results show the effectiveness of the method in diminishing the energy exchanged with the grid and also the possibility to optimize the performance of the storage systems.**

Keywords — Storage management, multi-pediod scheduling, prosumer, optimal energy management

I. INTRODUCTION

The common tendency to produce on site the necessary energy to the end user by means of small size plants, generally from non-programmable renewable sources, led to a rapid increase of installed photovoltaic (PV) power. Although PV generation offers economic and environmental benefits, its non-programmability can reduce these benefits. To increase the possibility to self-consume the produced energy and increase the profit for the user, storage systems should be utilized.

Otherwise, it is worth to underline that storage systems have a limited lifetime, related to their charge and discharge cycles. For this reason, it is opportune to manage storage systems with a specific strategy that can ensure them a long lifetime [1-2].

In order to better manage storage systems, realizing an accurate scheduling, generation and load forecasting systems would be useful to help the management of the grid.

Several methods carrying out storage management, considering different strategies, have been proposed in literature [3-7]. Such methods focus on an economical optimization, or a real time management without considering the optimization of storage lifetime. In [3] the "economical" optimal management of a storage system is carried out in a single period (24 hours ahead); if the optimization is not required 24h ahead, the method utilizes a real time approach. In [4] an appropriate management to reduce losses and increase distribution grid capacity is implemented and to this aim, a distributed storage is utilized; such a method allows to improve the utilization of renewable energy resources minimizing the energy adsorption from the grid.

Both methods [3,4] are implemented on a 24h period and they consider an economical optimization, moreover a multi-generation/multi-storage scheduling is realized.

It would be interesting to observe the benefits for a single user equipped with a PV generation system and a storage system, if the considered period is greater than 24h and a multi-period optimal management method is adopted.

In [5] users equipped of energy storage systems are considered; it explains how the interaction of different storage systems can be harmful for the grid, although such storage systems have been introduced to protect it. So a novel management technique for distributed storage systems is implemented. The utilization of this technique led to saving up to 13% of the electricity bill for each consumer with a 4-kWh storage system.

In [6] a day ahead optimization algorithm is implemented to provide the optimal storage and/or production scheduling strategy for a single user. The real load profile is considered exactly as the programmed 24h ahead profile.

At the user level, that is a prosumer level, it is advantageous to know generation and load profiles forecast to choose the better storage power scheduling.

Indeed, a goal for the user should be to make "himself-sustainable", satisfying his total energy demand by means of local energy production, minimizing the exchanges of energy with the grid.

This paper presents a multi-period storage management method and considers a prosumer equipped with a storage system. In particular basing on weather forecast, generation and load forecasts are obtained; Artificial Neural Networks are utilized to implement the two forecasting models. Starting from these load and generation forecasts, different simulations are performed: the method minimizes the overall energy exchanged with the grid, the power peaks between prosumer

This work was financed by the Italian Ministry of Economic Development (MISE) and the Ministry of Education, University and Research (MIUR) through the National Operational Program for Development and Competitiveness 2007-2013, Project DOMUS PON 03PE_00050_2.

G. Belli, G. Brusco, A. Burgio, D. Menniti, A. Pinnarelli, N. Sorrentino, and P. Vizza are with Department of Mechanical, Energy and Management Engineering (DIMEG) University of Calabria Via Bucci 42C, Arcavacata di Rende - CS, Italy (e-mail: name.surname@unical.it).

and grid or the energy in a particular time interval; moreover, a limit for the power exchanged with the grid is considered. Worth noting that the benefits of the storage systems have been also demonstrated by the same authors in [8]; in particular, they underline the suitability of the Li-Ion batteries compared with lead-acid batteries. Indeed, in this paper the economic aspects concerning the storage systems and in particular the management of the storage system are not examined. In this paper, an energetic and power analysis is carried out.

The rest of the paper is structured as follows: in the second section, the implemented forecasting models are illustrated; in the third part, Storage Management Method is described; in the last part, simulation results are shown and the benefits in the use of the method are underlined.

I. PV AND LOAD FORECASTING MODELS

The Multi-Period Storage Management (MPSM) Method has for input the renewable production profile and the load profile of a user. To generate these profiles, the MPSM method uses renewable production and load forecasting models. Several production and load forecasting models exist in literature; they present different accuracy which depends on several factors, such as utilized input data, utilized methodology, and so on. Independently from the used method, the results of the generation and load power forecast can be evaluated in different way.

A. Accuracy Estimation

Many performance parameters are used according to forecast purpose. In general, all these parameters represent the error between the forecasted and the actual value.

The Mean Absolute Error (MAE) [9] measures how close forecasts are to the outcomes. It is more sensitive to high value of the discrepancy between the forecasted and the actual power profiles, so it is used to underline the presence of discrepancy peaks (emphasizing the high error). It allows to know the consequent average power imbalance; the MAE is given by:

$$\mathrm{MAE} = \frac{1}{\mathrm{N}}\sum_{\mathrm{i}=1}^{\mathrm{N}}|\mathrm{f_i} - \mathrm{y_i}| = \frac{1}{\mathrm{N}}\sum_{\mathrm{i}=1}^{\mathrm{N}}|\mathrm{e_i}| \quad (1)$$

where fi is the forecast value, yi is the real value. Moreover, the evaluation of the Maximum Absolute Error (MaxAE) is important to know the maximum difference between fi and yi, in particular it is useful to know the maximum power imbalance resulting from the forecast; it is given by:

$$\mathrm{MaxAErr} = \mathrm{Max}(|\mathrm{f_i} - \mathrm{y_i}|) \quad (2)$$

The Mean Squared Error (MSE) [9] measures the mean square discrepancy between fi and yi. The MSE is more sensitive than the MAE to high error value. The MSE square root provides another statistical quantity, that is the Root Mean Squared Error (RMSE). The MSE and the RMSE are defined as:

$$MSE = \frac{1}{N}\sum_{i=1}^{N}(\mathrm{f_i} - \mathrm{y_i})^2 \quad (3)$$

$$RMSE = \sqrt{MSE} = \sqrt{\frac{1}{N}\sum_{i=1}^{N}(\mathrm{f_i} - \mathrm{y_i})^2} \quad (4)$$

Another important statistical quantity is the Mean Absolute Percentage Error (MAPE) [9]. It measures the forecasting accuracy and expresses this accuracy as a percentage. It is calculated by:

$$MAPE = \frac{1}{N}\sum_{i=1}^{N}\left|\frac{\mathrm{f_i} - \mathrm{y_i}}{\mathrm{f_i}}\right| \quad (5)$$

Moreover, the Maximum Percentage Error (MAxPE) allows knowing what the maximum percentage discrepancy between the forecasted and the actual value is:

$$\mathrm{MaxPE} = \max\left(\left|\frac{\mathrm{f_i} - \mathrm{y_i}}{\mathrm{f_i}}\right|\right) \quad \forall\, \mathrm{i} = 1 \ldots \mathrm{N} \quad (6)$$

Such statistical parameters allow to estimate the accuracy of the several forecasting models, to find the best suited to the case under estimation.

B. PV forecasting model

Referring to renewable production forecasting model, it is supposed that the power source is a photovoltaic (PV) plant.

Several PV forecasting models exist in literature: they often present accurate results. However, such models are very sophisticated and require information not always available, as those presented in [10-12]; the PV forecasting model implemented by the authors uses available input data and for this reason it is defined a "practical" forecasting model.

Such a PV generation forecasting model is implemented by an Artificial Neural Network (ANN).

For the implementation of the ANN, the Neural Network Toolbox of Matlab is utilized. The chosen ANN typology is a Multi-Layer Perceptron (MLP), with a supervised training algorithm; in particular, the back-propagation algorithm is used. Moreover, only a hidden layer is utilized, the activation function of all the neurons is tan-sigmoidal, while the training function is the Levenberg-Marquardt method [13].

Chosen the ANN typology, it is necessary to provide to the method historical input data and historical output (target) data (in the case under examination the collect of the PV power production data really generated by the PV plant).

The number of neurons of the input layer is chosen considering the input data, while the number of neurons of the hidden layer has been determined empirically. In fact, a sensitivity analysis has been conducted: the input data are kept constant and the number of neurons of the hidden layer are changed; under this condition, several tests to calculate the MAPE have been made. The optimum number of neurons for the hidden layer, to minimize the MAPE is 30, as shown in Figure1.

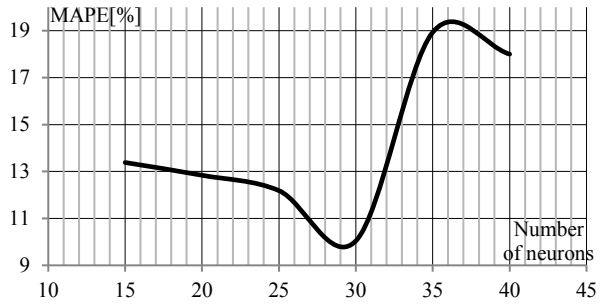

Fig. 1. Sensitivity analisys

So, summarizing, the implemented ANN consists in (Fig. 2):

- 5 input neurons (meteorological condition of the considered hour h, meteorological condition of the hour h+1, meteorological condition of the hour h-1, the hourly irradiance, the considered hour);
- 30 hidden layer neurons;
- 1 output neuron (hourly forecasted power production).

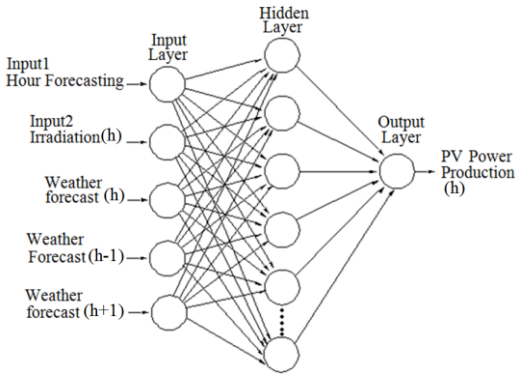

Fig. 2. ANN PV Forecasting Representation

Meteorological data about sky conditions are transformed to be used as input data for the ANN, in a number. A "1" to "5" scale has been used to represent the increasing of cloudiness. The minimum value ("1") indicates "clear-sky" condition while the maximum value ("5") indicates "storm" (Tab.1).

TABLE I. WEATHER CONDITIONS CODING

Code	***Weather condition***
1	Clear sky
2	Nearly cloudless, scattered clouds
3	Few clouds
4	Partly cloudy
5	Covered, Storm

The model has been tested on a specific a PV plant and good results are obtained both for clear and non-clear sky conditions.

Indeed, the results show that: in clear sky conditions the MAPE is less than 10%, while in non-clear sky conditions the MAPE is about 42%. The MAE, compared to PV power plant, is equal to 2.6% for clear sky conditions and 6.8% for non-clear sky conditions.

Figure 3 depicts the results of the PV forecast for the days from 30 August to 2 September; for these days, clear-sky conditions were predicted. The MAPE is calculated for all the four days: it is equal to 9.8%. Whereas, the percentage error is maximum and equal to 45% in the hours close to sunrise and sunset; while the percentage error becomes minimum (less than 1%) for the hours of higher production.

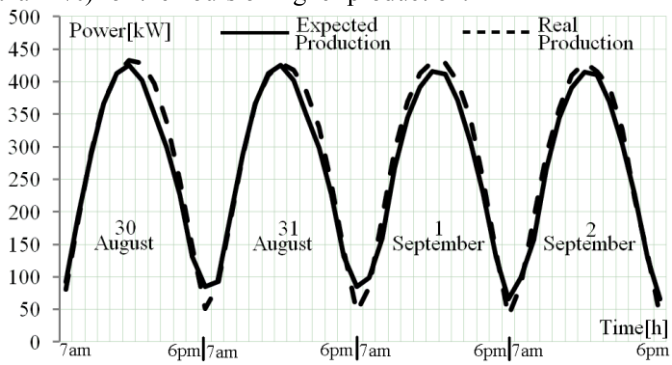

Fig. 3. Clear-Sky Days Results

C. *Load forecasting model*

Referring to the load forecasting model, in [14] the relevance to use load forecast for several purposes is underlined, especially for islanded operation, because it is necessary to guarantee grid stability, in addition to allow generation programmable system to work at a maximum efficient point.

In literature, there are a large number of load forecasting models as those presented in [15]. Reference [16] highlights that is more difficult to predict the individual load than an aggregate of loads. Nevertheless, in this paper a predictive model for an individual load is implemented.

The load forecasting model implemented in this paper utilizes accessible data; such a model predicts also individual and aggregate loads. Although its simplicity the results demonstrate the good performances of the model.

A feed-forward Multi-Layer Perceptron (MLP) ANN, supervised by a back-propagation algorithm, has been implemented (Fig. 4). For ANN training, the collection of consumption data of the considered user is necessary. Similarly than PV forecasting model, also for load forecasting model a sensitivity analysis has been carried out, so to detect the number of the hidden layer neurons which lead to a better accuracy of the model.

The implemented ANN consists in:

- 7 input neurons (month, day, day type, hour, daily maximum temperature, daily minimum temperature and daily average temperature);
- 30 hidden layer neurons;
- 1 output neuron (hourly forecasted power consumption).

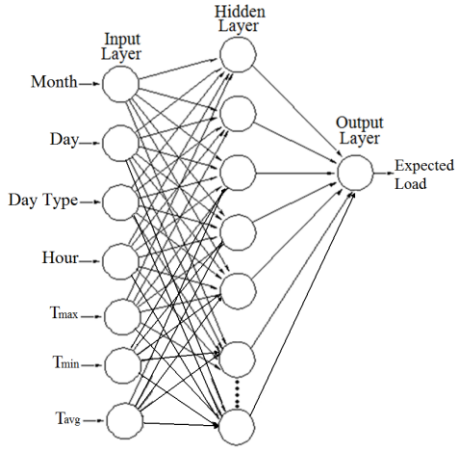

Fig. 4. ANN Load Forecasting Representation

The input data are so defined: the day, month and hour identify the period which the forecast is required; the day type identify if the considered day is a workday or a holiday, if it is a day before or after a holiday. Moreover, the minimum, maximum and average temperature are utilized; these are useful specially if the electric air conditioning is utilized, in particular maximum temperature is useful for cooling, whereas minimum temperature is useful for heating.

The load forecasting model has been tested on real data of a typical residential user. In Fig. 5, the forecasted and the real load profiles are shown, for three days (Thursday, Friday and Saturday). The obtained Mean Absolute Error (MAE), compared to the rated power of the considered user's contract is less than 6%, that is an acceptable error for the purpose of the method.

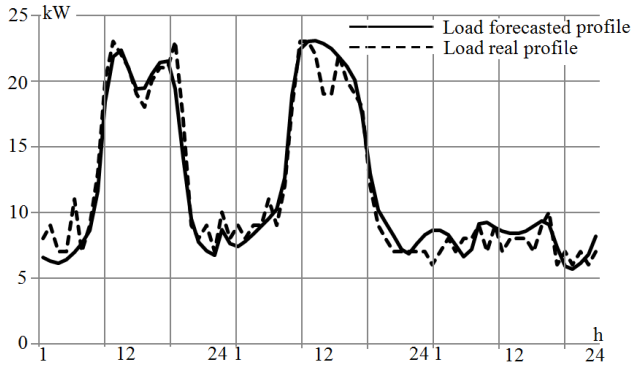

Fig. 5. Forecasted load profile and real load profile

Figure 5 depicts the results of the load forecast model; the MAPE is calculated and it is less than 20%. Whereas, the percentage error is maximum in the hours and day with a low consumption, and the minimum percentage error occurs for the workdays, when the consumption is high, and it is less than 1%.

II. Storage Management Method Description

The most important variables used in the Multi-Period Storage Management (MPSM) method are reported in Table 2.

TABLE II. MPSM Method Variables

Nomenclature	
$P_{g_t}^{\ d}$	Grid Transferred Power; (time t, day d)
$P_{L_t}^{\ d}$	Load Power; (time t, day d)
$P_{S_t}^{\ d}$	Storage Transferred Power; (time t, day d)
$E_{S_t}^{\ d}$	Storage Energy Level; (time t, day d)
$E_{S_{min}}, E_{S_{max}}$	Minimum and maximum Storage Energy Level
$P_{S_{min}}, P_{S_{max}}$	Minimum and maximum Storage Power
$E_{S_{Init}}$	Initial Energy stored

The main equations which describe the MPSM method are as follow:

$$OF: \min\left(\sum_{\substack{t=1\\d=1}}^{\substack{D\\T}} f(P_{g_t}^{\ d})\right) \tag{7}$$

s.t.

$$P_{g_t}^{\ d} = P_{L_t}^{\ d} - P_{PV_t}^{\ d} - P_{S_t}^{\ d} \tag{8}$$

$$E_{S_{t+1}}^{d} = E_{S_t}^{d} + P_{S_t}^{d} * \Delta t \tag{9}$$

$$E_{S_{min}} \le E_{S_t}^{\ d} \le E_{S_{max}} \tag{10}$$

$$P_{S_{min}} \le P_{S_t}^{\ d} \le P_{S_{max}} \tag{11}$$

$$sign\left(P_{S_t}^{\ d}\right) = sign(P_{PV_t}^{\ d} - P_{L_t}^{\ d}) \tag{12}$$

$$E_{S_{t=1}}^{d=1} = E_{S_{Init}} \tag{13}$$

The MPSM method can be utilized for more days (d) and every day is divided in more time intervals (t); such time intervals are the same of that used in the forecasting models.

In Objective Function (OF) (7), $f(P_{g_t}^{\ d})$ indicates different goals of energy exchange optimization. Indeed, the user can require to: minimize overall the energy exchanges with the grid, minimize the power peaks or minimize the energy exchanged for a particular time period with the grid

The MPSM method is subjected to the constraints from (8) to (13). Constraint (8) is used to calculate the power exchanged with the grid, $P_{g_t}^{\ d}$. The constrains (9), (10), (11), (12) and (13) concern the storage. In (9) the variation of the stored energy (between two time intervals) is calculated, in (10) the stored energy is limited between a minimum and maximum value (depending on the used storage); in (11) the charge and discharge storage power is limited, (12) indicates that the storage can charge only if there is a power surplus (PV power $P_{PV_t}^{\ d}$ is greater than the load power $P_{L_t}^{\ d}$), vice versa storage can only discharge. In (13) the initial stored energy is defined as $E_{S_{Init}}$.

Once load and PV production power forecasts for the user are obtained, the difference between the two profiles is calculated. This difference profile represents the input of the

MPSM method, which solves the Objective Function (OF), taking into account the constraints. The method returns the storage power exchange profile and the consequent grid power exchange profile.

III. Simulation

To test the effectiveness of the MPSM method, some simulations are carried out, considering as prosumer a build of University of Calabria: this is a business user, equipped with photovoltaic plants.

The considered build has a maximum power consumption of 25 kW and the installed PV plants power is 45 kW.

The test considers a time period of 7 days, from the 10th to 16th October 2015. In Fig. 6, load and PV power forecast profiles of the considered 7 days are reported.

After determining load and PV power profiles, it is necessary to sizing storage system for the required function.

A. Non optimized PV power

First of all, the storage capacity is calculated to supply loads and limit the exchange of energy with the grid.

Storage capacity will be the smallest between the resulting average daily energy purchased and supplied to the grid, which are calculated as the difference between PV production and load profiles. This analysis is carried out for profiles of a typical day. In the present case, the daily purchased energy is almost 170 kWh, whereas the energy supplied to the grid is 80 kWh; so the storage would have a capacity of 80 kWh.

After calculating storage capacity, an overestimation to be conservative will be necessary: an increase of 20% will be considered. In addition, in order to safeguard the storage useful life, a residual state of charge (SOC) of 40% has to be considered as a further increase of the estimated storage capacity.

Considering the previous estimated storage capacity (80 kWh) and the increases of 20% and 40%, the obtained storage capacity is about 140 kWh.

Starting from the calculation of the difference between load and PV power forecasts, it is used for two groups of simulations. The first group of simulation aims to minimize the total exchange of energy with the grid, trying to make the prosumer self-sustainable and to avoid congestions on the grid. Instead, the second group of simulations aims to minimize only the peaks of energy during the day, trying to reduce the costs of energy supply and to avoid worthless oversize of the generation plants. For both the groups of simulations, the comparison is made between the condition with storage working in "real time", that is no storage management is taking into account, and the condition with storage managed by MPSM method.

The starting point is the value of the overall energy exchanged between the user and the grid without using a storage system: this value is equal to 1.68 MWh, where 1.13 MWh is the energy adsorbed by the user and 0.55 MWh is the energy left to the grid.

For the first groups of simulations, when none management method is utilized, the total energy exchange with the grid decreases until 0.69 MWh, where 0.60 MWh is the purchased energy by the user and 0.09 MWh supplied to the grid. If the storage is managed by MPSM method, the total energy exchanged with the grid is equal to 0.68 MWh. Respect the previous case, the difference is very limited. Although this difference is only of 0.01 MWh, the positive effect of the MPSM method consists in the possibility to maximize the performances of the storage. Indeed, using a "real time" operation strategy, the charge and discharge cycles are not optimized because they are partial cycles, while with MPSM method, the storage executes always full cycles of charge and discharge (Fig.7). Only in a few hours, a distorted trend is visible in Fig. 7, due to the high variability of weather conditions on the 5th day, that involves to have a partial cycle of charge and discharge.

For the second group of simulations, minimizing only the peaks of power exchanged with the grid, the power exchanged in "real time" reaches 23 kW, while using MPSM method, it is about 8 kW. In Fig. 8 the exchanged energy profile with and without MPSM method are depicted.

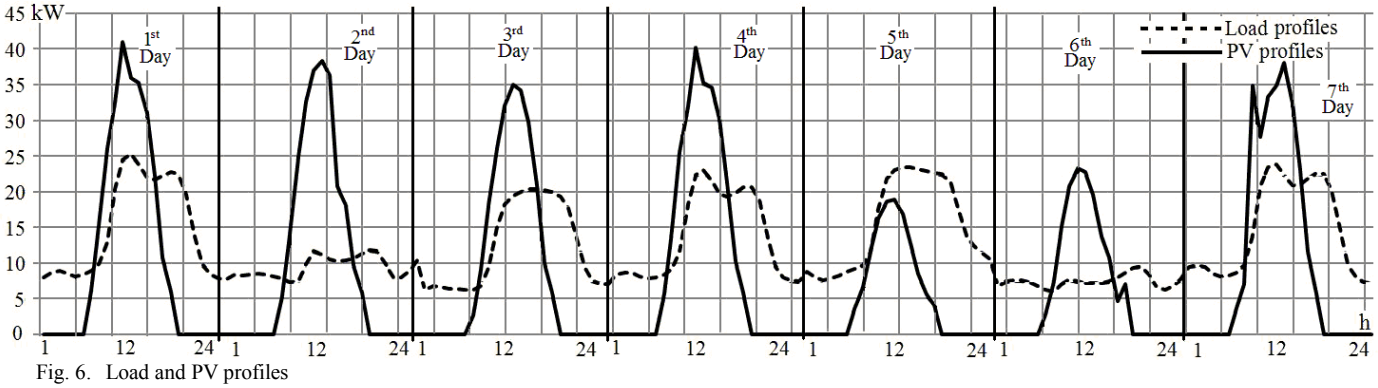

Fig. 6. Load and PV profiles

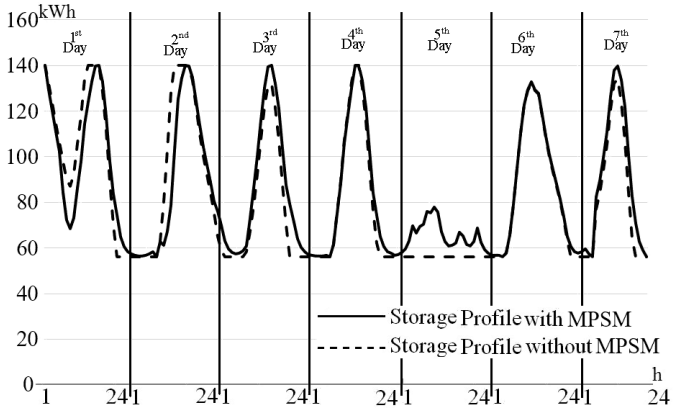

Fig. 6. Stored Energy Profile with and without MPSM

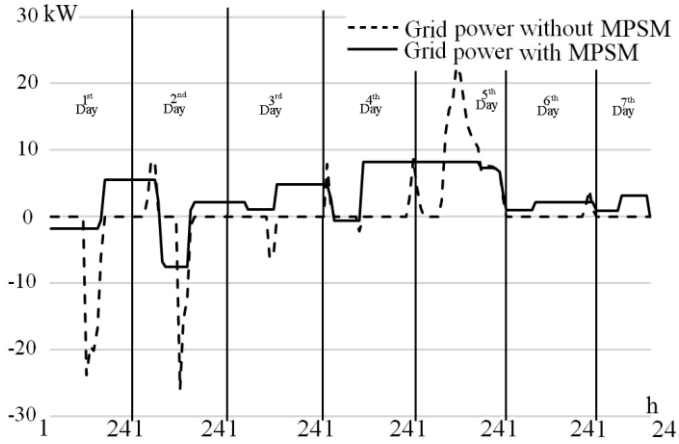

Fig. 7. Exchanged power profiles with and without MPSM

B. *Optimized PV power*

In this section, starting from the average daily load profile and the monthly average daily PV production profile, to minimize the exchange of energy with the grid, the PV plant is sized to cover the daily energy demand. Considering this, the obtained rated PV power is about 56 kW.

Similarly to the previous subsection A, the storage system is properly sized and the obtained capacity is about 240 kWh. With such data the method is utilized to carry out the same test of the previous case.

First of all, the MPSM method is utilized to minimize the exchange of energy with the grid; the obtained result of the total energy exchanged with the grid is equal to 0.41 MWh, where 0.25 MWh is the purchased energy by the user and 0.16 MWh is the energy supplied to the grid.

In this case, as the rated PV power and the storage capacity are optimized, the use of the MPSM method, compared to the real time management, does not contribute to many advantages in the management of the charge/discharge storage cycles.

The real advantage would occur in the management of the exchanged energy with the grid for the days with non-clear sky conditions. In Fig. 9 the exchanged energy profile with the grid, with and without the MPSM method is depicted.

Moreover, referring to Fig. 9, it is possible to observe that the energy supplied to the grid is greater than the energy purchased from the grid; only the 5th day the purchased energy is greater than the supplied one, because it is not a clear sky day.

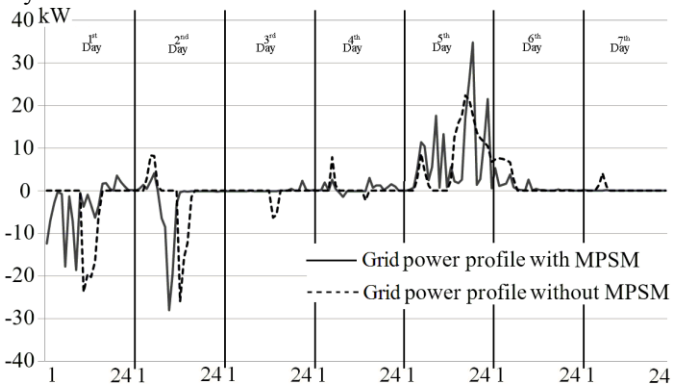

Fig. 8. Exchanged grid power profile with and without MPSM

Worth noting that the PV power is sized to cover the daily energy demand; so if the rated PV power increase, obviously the produced energy increase and as a consequence the total energy exchanged with the grid increases. In fact, for example, if the rated PV power is 60 kW the total exchanged energy is 0.49 MWh, instead of 0.41 MWh. This shows that before to use the MPSM method, optimal PV and storage sizing is necessary.

C. *Grid Power Restriction*

In this section, it is supposed that the considered prosumer has a limit for $P_{g_t}^{\ d}$. This can be due to different reason, for example if the prosumer has a contract with the energy provider for a reduced power, or if the power line is designed for a limited power.

In fact, this kind of optimization allows to reduce the problems due to the congestion problem and any restrictions of the power interface devices.

In particular two cases are examined: in the first case the maximum $P_{g_t}^{\ d}$ (Pg_max) is 10 kW, in the second case Pg_max is 7 kW. Worth noting that the limit for the power is both for the supplied and delivered energy. The MPSM method is completed using the sequent equations:

$$|P_{g_t}^{\ d}| \leq P_{g\_max} \tag{14}$$

The OF is implemented to minimize the entire energy exchanged with the grid, as implemented above. It is worth to underline that this test is different to the previous minimization of the peak power, in fact in the previous case a restriction for $P_{g_t}^{\ d}$ is not utilized but solely the peaks of $P_{g_t}^{\ d}$ are reduced.

In the first test Pg_max is equal to 10 kW and the constraint (12) is relaxed, in this way the storage can be charged also by the grid and can discharge also if there is a surplus of energy, this is limited only through the OF.

The utilized storage capacity is 240 kWh and the rated PV power is 56 kW; the load profile is reported in Fig. 6.

In this first case, the obtained result of the total energy exchanged with the grid is equal to 0.41MWh, where 0.26 MWh is the purchased energy by the user and 0.15 MWh is the energy supplied to the grid.

In the second case, Pg_max is equal to 7 kW, the total energy exchanged with the grid is also equal to 0.41MWh, and the purchased energy is equal to 0.26 MWh whereas the supplied energy to the grid is equal to 0.15 MWh.

Such results demonstrate that the constrains on $P_{g_t}^{\ d}$ are almost irrelevant for the OF, in fact the quantity of energy exchanged with the grid is the same of the previous case. The only difference is for the profile of $P_{g_t}^{\ d}$: in Figs. 10 and 11 the profiles of power exchanged with the grid for either cases are reported.

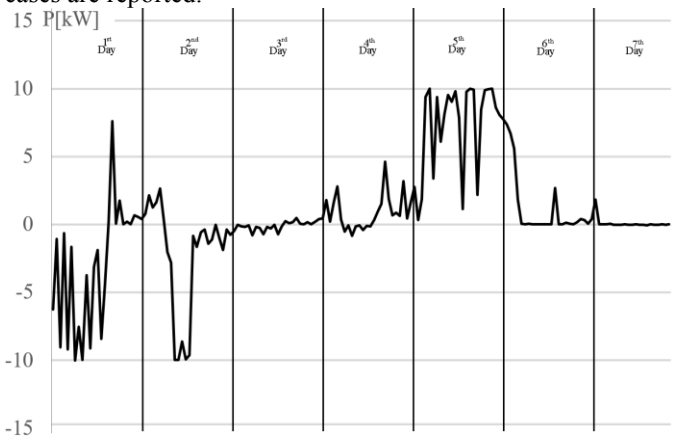

Fig. 9. Exchanged grid power profile with the constrain P_{g_max}=10 kW

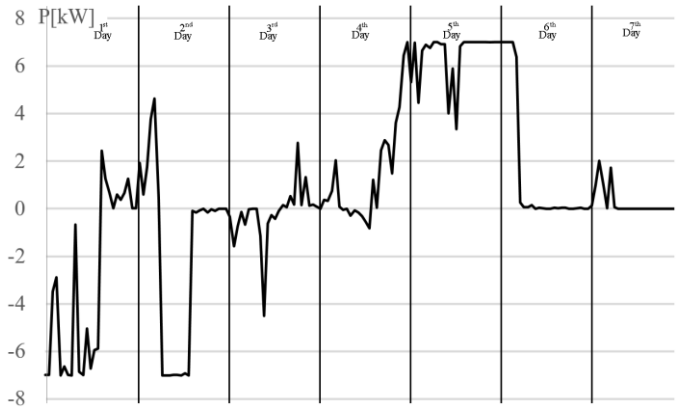

Fig. 10. Exchanged grid power profile with the constrain P_{g_max}=7 kW

The figures show that the trend of $P_{g_t}^{\ d}$ is constant in the area where the power peak occur, this means that for those time and day the bonds are achieved; this is particularly observable for Pg_max is 7 kW.

Moreover, worth noting that the maximum power Pg_max (7 kW), obtained in this case, is less than the maximum power obtained with the minimization of the peak of power (in Subsection A) where Pg_max is 8.2 kW.

It is important to observe the behaviour of the storage system when Pg_max is equal to 7 kW compared to the case when there is not a constrain for $P_{g_t}^{\ d}$: in figure 12 this comparison is reported.

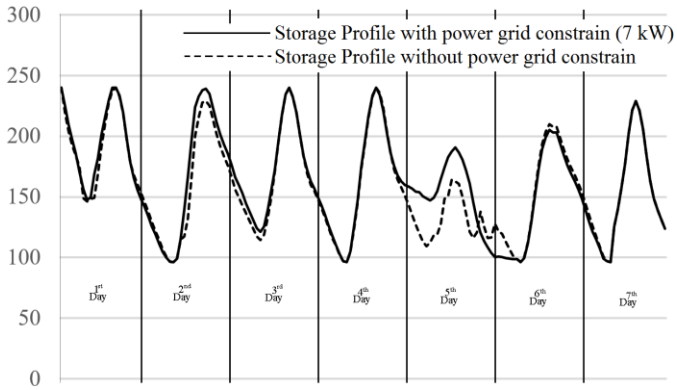

Fig. 11. Stored Energy Profile with and without P_{g_max} constrain

It is possible to observe the differences between the two profiles, especially for the fifth day. In fact, to limit the power exchanged with the grid, in particular the power drawn from the grid, the stored energy is maintained as long as it is not used to decrease $P_{g_t}^{\ d}$: the battery is not discharged just when there is a deficit of energy but when this energy is utilized to limit the maximum $P_{g_t}^{\ d}$.

Thanks to the MPSM method the prosumer can employ a reduced power contract with consequent less costs for the prosumer. At the same time the Distribution System Operator (DSO) can design the line for a reduced power, with further savings.

IV. Conclusion

The paper shows the importance of an opportune management method for storage devices. In fact, the positive effect resulting from the use of storage systems, particularly in relation to non-programmable resources, can be increased if an appropriate management strategy is utilized. One of the feature of the implemented method is its multi-periodicity. In fact, if the management is made on more days, there are more data input and the storage can be managed in a better way.

The presented storage management method implements different management goals.

First of all, the method minimizes the total energy exchanged with the grid to make users self-sustainable. This implies the use of opportune PV and load forecast models. Secondly the method is also utilized to reduce the peak of power exchanged with the grid, decreasing from 23 kW to about 8 kW.

Moreover, it is underlined that an accurate sizing of PV and storage systems is necessary before to implement and utilize a management strategy.

The results are compared with the real time storage management; such a comparison shows the effectiveness of the method. The results show also the possibility to optimize the performance of the storage device in terms of charge and discharge cycles.

At the end, the behaviour of the management method, if a constrain for the maximum $P_{g_t}^{\ d}$ is utilized, is evaluated. Simulations are carried out; they demonstrate that despite a further constrain is utilized, the entire energy exchanged with the grid is minimized. This can be a good result both for the

prosumer and for the DSO, indeed they can respectively reduce the contract power and reduce the line capacity, with consequent savings.
Moreover, it would be interesting evaluate the behaviour of the method if a schedulable load is adopted.

REFERENCES

[1] D. Menniti, A. Pinnarelli, N. Sorrentino, A. Burgio, and G. Brusco, "Energy Management System for an Energy District With Demand Response Availability", Smart Grid, IEEE Transactions on, vol. 5(5), 2014, pp. 2385-2393.

[2] D. Menniti, A. Pinnarelli, N. Sorrentino, G. Belli, A. Burgio, "Demand Response Program in an Energy District with storage availability", International Review of Electrical Engineering, in press.

[3] A. Nottrott, J. Kleissl, and B. Washom, "Energy dispatch schedule optimization and cost benefit analysis for grid-connected, photovoltaic-battery storage systems", Renewable Energy, vol. 55, 2013, pp. 230-240.

[4] N. Jayasekara, P. Wolfs, and M.A.S. Masoum, "An optimal management strategy for distributed storages in distribution networks with high penetrations of PV", Electric Power Systems Research, vol. 116, 2014, pp. 147-157.

[5] P. Vytelingum, T.D. Voice, S.D. Ramchurn, A. Rogers, and N.R. Jennings, "Agent-based micro-storage management for the smart grid", in Proc. of the 9th International Conference on Autonomous Agents and Multiagent Systems, vol. 1, International Foundation for Autonomous Agents and Multiagent Systems, pp. 39-46, May 2010.

[6] I. Atzeni, L.G. Ordóñez, G. Scutari,D.P. Palomar, and J.R. Fonollosa, "Demand-side management via distributed energy generation and storage optimization", Smart Grid, IEEE Transactions on, vol. 4(2), 2013, pp. 866-876.

[7] A. Mohamed, and O. Mohammed, "Real-time energy management scheme for hybrid renewable energy systems in smart grid applications", Electric Power Systems Research, Vol. 96, 2013, pp. 133-143.

[8] D.Menniti, A. Pinnarelli, N. Sorrentino, A. Burgio, G. Brusco, "The economic viability of a feed-in tariff scheme which solely awards the self-consumption for promoting the use of integrated photovoltaic-battery systems", Applied Energy, in press.

[9] S. Makridakis, and M. Hibon, "Evaluating accuracy (or error) measures", Working paper 95/18/TM, INSEAD, (1995) France.

[10] Y. Zhang, M. Beaudin, Raouf Taheri, H. Zarcipour, and D. Wood, "Day-Ahead Power PV power production Output Forecasting for Small Scale Soar Photovoltic Electricity Generators", IEEE Transactions on Smart Grid, Vol. 6, no. 5, September 2015

[11] C. Chen, S. Duan, T. Cai, and B. Liu, "Online 24-h solar power forecasting based on weather type classification using artificial neural network", Solar Energy, Vol. 85, no. 11, 2011, pp. 2856-2870.

[12] C. W. Chow, B. Urquhart, J. Kleissl, M. Lave, A. Dominguez, J. Shields, and B. Washom, "Intra-hour forecasting with a total sky imager at the UC San Diego solar energy testbed", Solar Energy, Vol 85, no. 11, 2011, pp 2881–2893.

[13] J. J. Moré, "The Levenberg-Marquardt algorithm: Implementation and theory", in Lecture Notes in Mathematics, No. 630–Numerical Analysis, Springer-Verlag, 1978, pp. 105–116.

[14] N. Hatziarg, Microgrids: Architectures and Control, Wiley-IEEE Press, February 2014.

[15] H. S. Hippert, C. E. Pedreira, and R.C. Souza, "Neural networks for short-term load forecasting: A review and evaluation", Power Systems, IEEE Transactions on, vol. 16(1), 2011, pp 44-55.

[16] H. Chitsaz, H. Shaker, H. Zareipour, D. Wood, and N. Amjady, "Short-term electricity load forecasting of buildings in microgrids", Energy and Buildings, vol. 99, 2015, pp. 50-60.

Grazia Belli (Italy, 1985) received her degree in Energetic Engineering in 2011 and her Ph.D in Science of Complex Systems in 2016 from the University of Calabria. Her current research interests concern renewable energy sources, distributed generation, smart grid technologies and electricity local market.

Giovanni Brusco (Italy, 1980) received his degree in Electronics Engineering from the University of Calabria, Italy, in 2007 and his Ph.D. in Computer and system Engineering in 2013 at the Electronic, Computer and Systems Science Department of the University of Calabria, Italy. His current research interests concern renewable energy sources, distributed generation, harmonic analysis and smart grid technologies.

Alessandro Burgio (Italy, 1973) received his degree in Management Engineering from the University of Calabria in 1999 and his Ph.D. in Computer and system Engineering in 2006 at the Electronic, Computer and Systems Science Department of the University of Calabria, Italy. His current research interests include electrical power systems, distributed generation, renewable energy, power electronics and harmonics, electronic ballast.

Daniele Menniti (Italy 1958) received his degree in Electrical Engineering from the University of Calabria, Cosenza, Italy and his Ph.D. degree in Electrical Engineering from the University of Naples, Italy, in 1984 and 1989 respectively. He is an Associate Professor at the Mechanical, Energetic and Management Department of the University of Calabria, Italy. His current research interests concern electrical power system analysis, real-time control and automation.

Anna Pinnarelli (Italy, 1973) received her degree in Management Engineering from the University of Calabria in 1998 and her Ph.D. in Electrical Engineering in 2002 from the Electrical Engineering Department of the University of Naples, Italy. She is an Assistant Professor at the Mechanical, Energetic and Management Department of University of Calabria, Italy. Her current research interests concern FACTS technology, harmonic analysis, electrical system automation, decentralized control and smart grid technologies.

Nicola Sorrentino (Italy, 1970) received his degree in Management Engineering in 1994 and a Ph.D. in Computer and system Engineering in 1999 at the Electronic, Computer and Systems Science Department of the University of Calabria, Italy. He is a Researcher at the Mechanical, Energetic and Management Department of the University of Calabria, Italy.

Pasquale Vizza (Italy, 1990) received his degree in Energetic Engineering in 2014 from the University of Calabria; he is currently attending the PhD school at the same University. His current research interests include renewable energy sources, smart grid technologies, energy storage economics, generation and load forecasting.

Adjusting output impedance using a PI controller to improve the stability of a single-phase inverter under weak grid

Jiao Jiao and R. M. Nelms

Abstract— **Explored in this paper is the grid impedance effect on the stability of a single-phase grid connected inverter with an *LC* filter based on an analysis of the inverter output impedance. For a single-phase grid connected inverter, a PI controller is often used to regulate the current injected into the grid. However, the control performance can be influenced when the inverter is connected to a weak grid. Also, the utility grid has background harmonic noise, which can make the injected current distorted. Therefore, analysis of the output impedance of a single-phase grid connected inverter is important for the robustness and stability of the system. By modeling the output impedance of inverter, it can be determined that the proportional gain and integral gain of the controller have an effect on the output impedance. Analytical results show that by adjusting the PI controller parameters, the ability for harmonic reduction and stability of the system can be improved. Simulation and experiments using a 1 kW single-phase grid connected inverter verify the effectiveness of the theoretical analysis.**

Index Terms— **Grid impedance, inverter output impedance, LC filter, PI controller, single-phase inverter**

I. Introduction

DISTRIBUTED generation technologies such as solar panels and wind turbines are being investigated because they are environmentally friendly. The voltage source inverter, which is the connection interface between distributed generation and the utility grid, plays an important role and has received more and more attention. An *LC* filter or an *LCL* filter is commonly used to reduce the pulse width modulation (PWM) switching harmonics. Generally, the *LCL* filter has better performance in attenuating higher order harmonics and smaller component size and weight compared to an *LC* filter. However, the *LCL* filter is third order, which can introduce a resonant peak into the system that will cause an oscillation. For a small power inverter (a few kW), an *LC* filter is a better choice for the harmonic attenuation. In this paper, we employ an *LC* filter for the single-phase grid connected inverter.

In the case of long distribution lines and lower power transformers in a distribution system, the grid can have a large impedance, which is a typical weak grid. However, the controller design for a grid-connected inverter usually doesn't take the grid impedance into consideration. When a voltage source inverter is connected into a weak grid, the inverter control performance can be influenced [1]. The variation of the grid impedance may decrease the current controller bandwidth. In order to find the effect of grid impedance on the stability of the system, the external characteristics of the inverter need to be explored. Generally, it can be modeled by the output impedance of the inverter. The relationship between the output impedance of the inverter and the grid impedance has been studied by many researchers [2-4]. For stability analysis, the impedance-based stability criterion can be used to examine the ratio of the inverter output impedance to the grid impedance [2]. However, it doesn't mention a way to improve the stability of the system. In order to reduce the effect of grid impedance, the output impedance can be regulated accordingly. The output impedance depends on the design of the *LC* filter and the control structure and parameters. To improve the stability of the system and the ability for harmonic rejection, the output impedance can be changed by adjusting the controller parameters. Therefore, the output impedance based method is explored under a weak and distorted grid.

In this paper, a 1 kW single-phase grid connected inverter is used to investigate the output impedance of the system. By analyzing the output impedance in the frequency domain, the controller parameters can be adjusted to regulate the output impedance. By increasing the proportional gain of the PI controller, the magnitude of the output impedance can be increased to improve the ability for harmonic rejection. By increasing the integral gain of the PI controller, the phase of the output impedance can be increased to improve the stability of system. Experimental results are in agreement with simulation analysis.

II. Stability Analysis of A Single-Phase Inverter Considering Grid Impedance Variation

A. Modeling of the single-phase inverter

The structure of a single-phase grid connected inverter with an *LC* filter is presented in Fig. 1. V_{dc} is the input DC link voltage, v_{inv} is the output voltage of the H-bridge inverter and

Submitted on: 27 Sep. 2016. Accepted on: 30 Oct. 2016.

Jiao Jiao is with the Electrical and Computer Engineering Department, Auburn University, Auburn, AL 36849 USA. (e-mail: jzj0034@auburn.edu).

R. M. Nelms is with the Electrical and Computer Engineering Department, Auburn University, Auburn, AL 36849 USA. (e-mail: nelmsrm@auburn.edu).

v_g is the utility grid voltage. The *LC* filter consists of inverter side inductances L_1 and L_2 and a filter capacitance *C*. The inductances L_1 and L_2 are two equal inductances used for attenuating the common mode noise current in the circuit. In addition, the electromagnetic interference (EMI) effects are alleviated. L_g is the grid impedance. The inductor current i_L, is used for current control to regulate the injected current with lower harmonics and unity power factor. The utility grid is sensed using a phase loop lock (PLL) to make the single-phase inverter synchronize with the grid voltage.

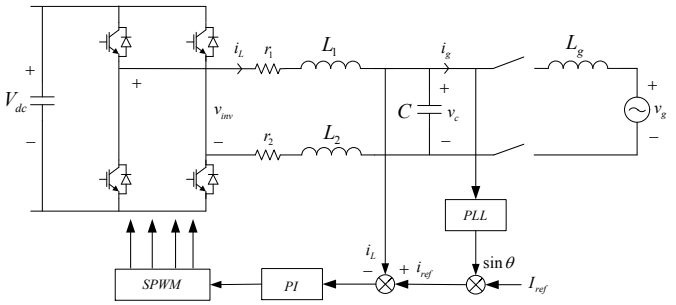

Fig. 1. Single-phase grid connected inverter with *LC* filter

According to Kirchhoff's voltage law, we can get the circuit equation shown as follows:

$$(L_1 + L_2)\frac{di_L}{dt} + (r_1 + r_2)i_L = v_{inv} - v_c \tag{1}$$

Where r_1 and r_2 are the parasitic resistances of the inductors. By transforming to the frequency domain, the transfer function between inductor current and the difference between the inverter output voltage and the capacitor voltage can be derived.

$$G_p(s) = \frac{I_L(s)}{V_{inv}(s) - V_c(s)} = \frac{1}{Ls + R} \tag{2}$$

Where $L = L_1 + L_2$, $R = r_1 + r_2$.

B. Output impedance of a single-phase inverter

Many power converters are digitally controlled which will introduce sampling and computational delays into the system. Also, the PWM process will introduce delay due to a zero-order hold [5]. Therefore, the total delay can be approximated by one and a half sampling period, which can be expressed by $G_d(s)$ shown below.

$$G_d(s) = e^{-1.5Ts} \approx \frac{1}{1 + 1.5Ts} \tag{3}$$

The variable *T* is the sampling period. A PI controller is applied for current control in this inverter. The transfer function of a PI controller is shown as follows:

$$G_c(s) = k_p\left(1 + \frac{1}{\tau_i s}\right) \tag{4}$$

Here k_p is the proportional gain and τ_i is the integral gain. The system control block diagram is shown in Fig. 2 [6]. Fig. 2(a) can be simplified to Fig. 2(b) by control block equivalent transformations. The resulting transfer function of $G_1(s)$ and $G_2(s)$ can be expressed by:

$$G_1(s) = \frac{K_{pwm}G_c(s)G_d(s)}{Ls + R + K_{pwm}G_c(s)G_d(s)} \tag{5}$$

$$G_2(s) = \frac{sL + R + K_{pwm}G_c(s)G_d(s)}{LCs^2 + RCs + K_{pwm}G_c(s)G_d(s)Cs + 1} \tag{6}$$

The output impedance of the inverter can be defined by:

$$Z_o(s) = \left.\frac{v_c(s)}{-i_g(s)}\right|_{i_{ref}=0} = G_2(s) \tag{7}$$

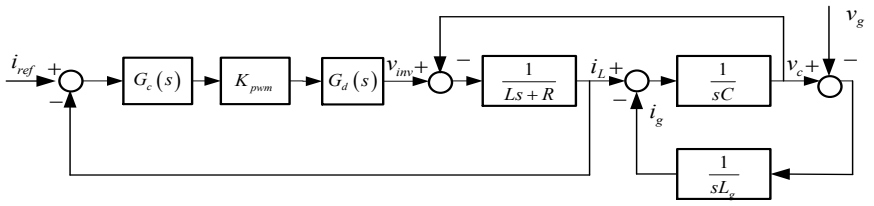

(a)

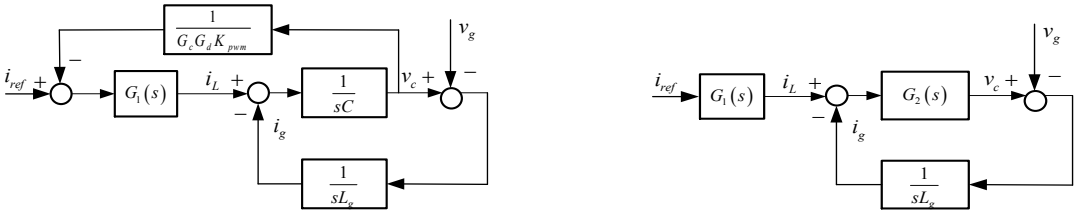

(b)

Fig. 2. Control block diagram for a single-phase grid connected inverter (a) and its equivalent transformation (b)

Therefore, the single-phase grid connected inverter with an *LC* filter can be modeled by the Norton equivalent circuit, as shown in Fig. 3. The inverter is represented by a current source and a parallel output impedance, and the utility grid is modeled by a voltage source and a grid impedance [2]. In this effort, only the grid inductance is considered in the analysis as a worst case scenario. In reality, the resistance in the grid will help to stabilize the system.

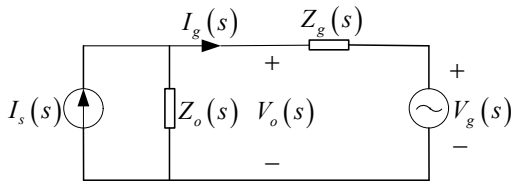

Fig. 3. Norton equivalent circuit

An expression for the inverter output current can be derived by:

$$I_g(s)=\frac{1}{1+Z_g/Z_o}I_s(s)-\frac{1/Z_o}{1+Z_g/Z_o}V_g(s) \tag{8}$$

From (8), it can be found that in order to mitigate the effect caused by grid voltage and grid impedance variation, the output impedance should be designed as high as possible to operate stably [2]. It can be found from (7) that the output impedance depends on the design of the *LC* filter and the controller structure and parameters. Therefore, the inverter output impedance can be shaped by adjusting the controller parameters to improve the system stability.

C. Relationship between inverter output impedance and grid impedance

A current controller is designed by assuming that the inverter is connected into an ideal grid ($L_g = 0$). The bode plot of the uncompensated system (without a current controller) and the bode plot of the compensated system (with current controller) are shown in Fig. 4. When the inverter is connected into a utility grid, the grid impedance can influence the inverter control performance. Fig. 5 shows the relationship between inverter output impedance and grid impedances in the frequency domain. According to [3-4], the stability of the inverter depends on the inverter output impedance's phase at the intersection point of Z_o and Z_g. With an increase in the grid impedance, the phase of the output impedance at the intersection frequency point is decreasing, which implies the system is less stable.

In order to enhance the stability of the system under a wide range of grid impedance, the phase of the inverter output impedance at the intersection point should be increased by shaping the current controller parameters. The magnitude of inverter output impedance also needs to be designed higher to achieve better harmonic rejection ability.

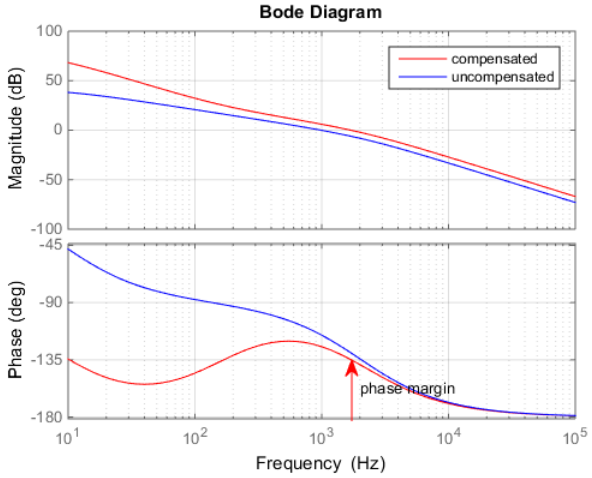

Fig. 4. Bode plot of the compensated and uncompensated system

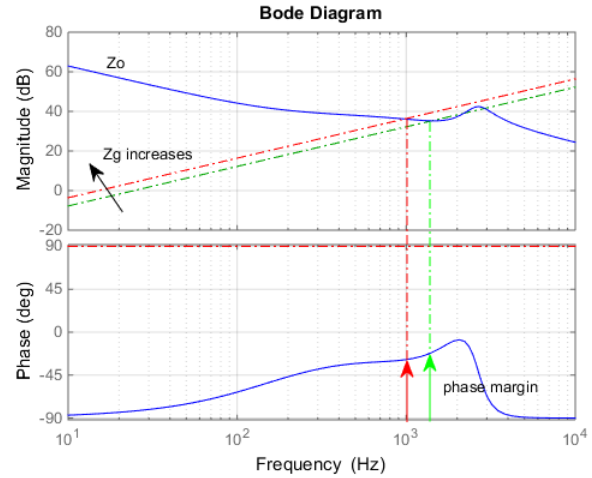

Fig. 5. Bode plot of the inverter output impedance and different grid impedances

D. Shaping PI controller parameters to improve the stability of system under weak grid

By analyzing (7), it can be determined that the output impedance of the inverter can be changed by adjusting the parameters of the PI controller. As seen in Fig. 6, the lower frequency part of the bode diagram shows that the magnitude of the output impedance increases with increasing proportional gain k_p, which improves the ability for harmonic reduction. However, the phase of the inverter output impedance is decreasing, which means the system might be becoming less stable.

As for increasing the integral gain of the PI controller, the phase of the inverter output impedance at the intersection frequency is increased, but the magnitude of the output impedance is decreased in the low frequency range. In the high frequency range, the magnitude and phase of inverter output impedance does not change much. It can be concluded that increasing the integral gain has the opposite effect on the output impedance as compared to increasing the proportional

gain of the controller. Therefore, it is possible to increase the magnitude and phase of the output impedance by adjusting the PI controller parameters without affecting the performance of the inverter.

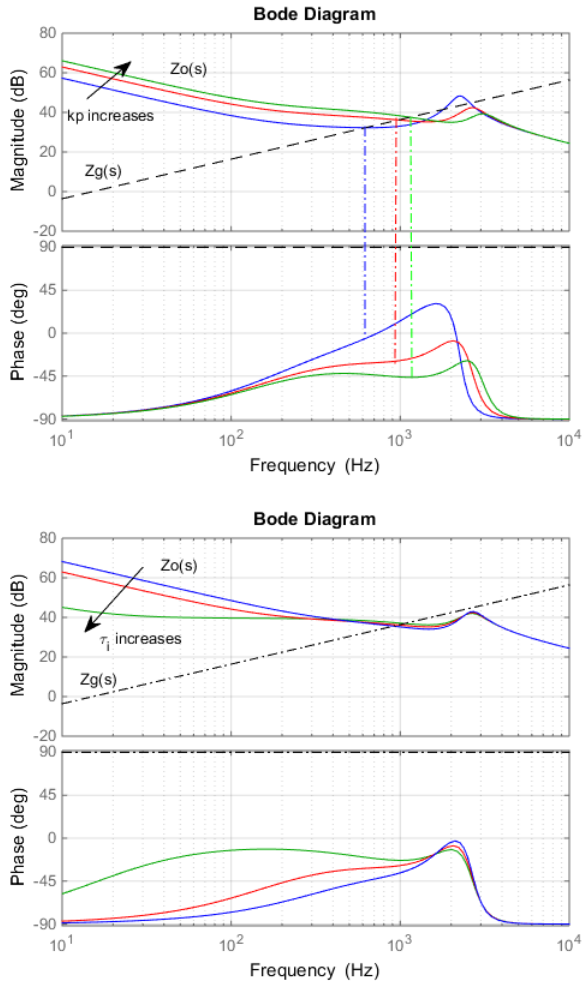

Fig. 6. Bode plot of inverter output impedance and grid impedance (a) proportional gain changes (top) (b) integral gain changes (bottom)

E. Output impedance sensitivity to circuit parameters

From (7), it can be found that the inverter output impedance depends on the circuit parameters and controller parameters. In reality, the circuit parameters can change due to the temperature variation of the surrounding environment. Therefore, it is necessary to explore the effect of circuit parameter variations on the inverter output impedance. Since the parasitic resistance of the filter inductors has little effect on the inverter output impedance, the resistance variation is not investigated here.

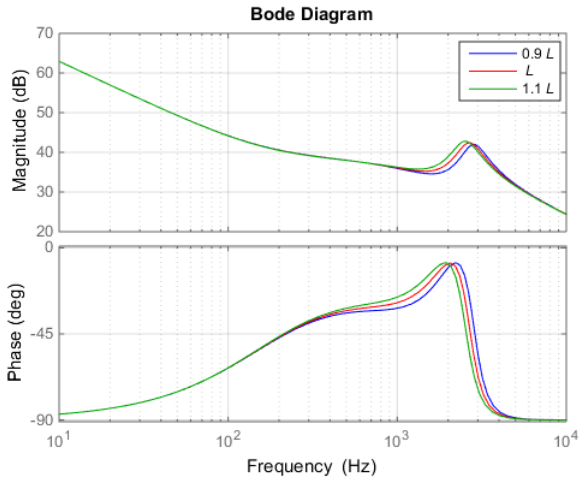

Fig. 7. The inverter output impedance sensitivity to inductance variation

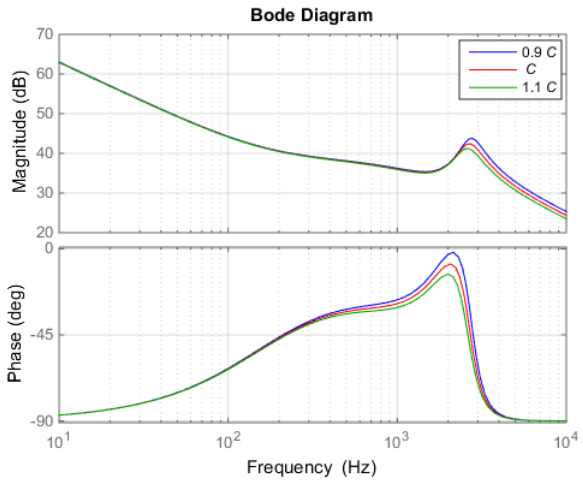

Fig. 8. The inverter output impedance sensitivity to capacitance variation

From Fig. 7, it can be seen that the frequency response of the inverter output impedance shifts to the left slightly as the inductance increases. It mainly affects the magnitude and phase of inverter output impedance around the peak. As shown in Fig. 8, with the increase of filter capacitance, the magnitude of the inverter output impedance remains unchanged in low frequency range, but it decreases in the high frequency range. The phase margin of the inverter output impedance is also decreased.

III. Simulation Results

The system shown in Fig. 1 is simulated by MATLAB to validate the theoretical analysis. The system parameters are given in Table I. For the simulation, the utility grid voltage (v_g in Fig. 1) is modeled by 7% third harmonics and 5% fifth harmonics and 3% seventh harmonics with phase 30°, 90° and 270°, respectively.

TABLE I
CIRCUIT PARAMETERS

Circuit Parameter	Symbol	Value
DC-link Voltage	V_{dc}	380 V
Utility Grid Voltage	v_g	120 V
Fundamental Frequency	f_0	60 Hz
Inverter Inductance	L	7 mH
Inductance parasite resistance	R	0.4 Ω
Filter Capacitance	C	1 μF
Switching Frequency	f_s	19.2 kHz

Fig. 9 to Fig. 10 show the simulation results when the proportional gain was changed from $k_p = 2$ to $k_p = 3$; the grid impedance was 19.5 mH. The grid current total harmonic distortion (THD) is 4.30% and 3.76%, respectively. The harmonic reduction ability is improved, which validates the analysis in Section II. Fig. 11 to Fig. 12 show the simulation results when the integral gain was changed from $\tau_i = 0.0005$ to $\tau_i = 0.01$; the grid impedance was 19.5 mH. The grid current total harmonic distortion (THD) is 4.51% and 4.83%, respectively. Table II and Table III show the harmonic analysis of the inverter output current.

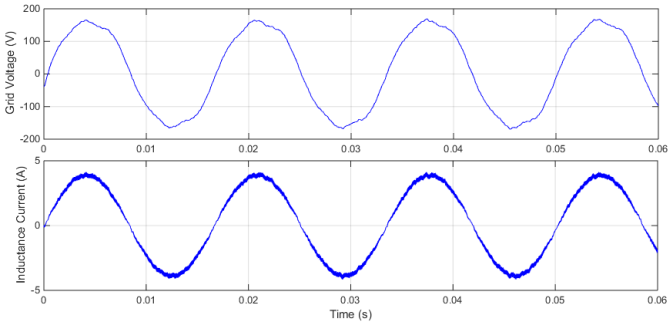

Fig. 9. Output voltage and output current when $L_g = 19.5$ mH ($k_p = 2$)

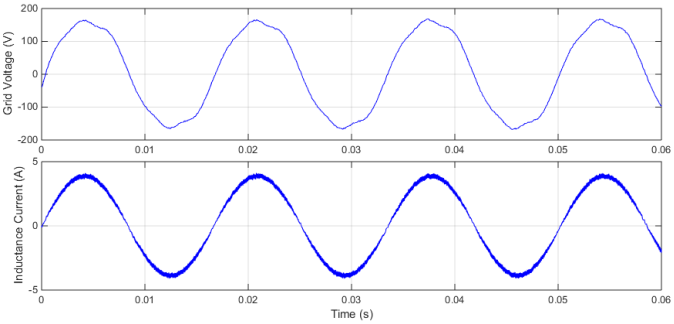

Fig. 10. Output voltage and output current when $L_g = 19.5$ mH ($k_p = 3$)

TABLE II
OUTPUT CURRENT HARMONIC ANALYSIS

Harmonic Order	$L_g = 6.5$ mH		$L_g = 19.5$ mH	
	$k_p = 2$	$k_p = 3$	$k_p = 2$	$k_p = 3$
3rd	0.71%	0.73%	1.12%	0.88%
5th	0.34%	0.42%	0.53%	0.17%
7th	0.45%	0.33%	0.53%	0.32%
9th	0.16%	0.17%	0.24%	0.25%
11th	0.13%	0.15%	0.19%	0.18%
13th	0.16%	0.10%	0.12%	0.18%
THD	3.76%	3.51%	4.30%	3.76%

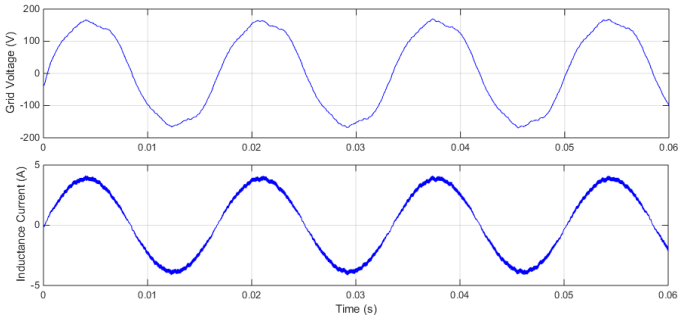

Fig. 11. Output voltage and output current when $L_g = 19.5$ mH ($\tau_i = 0.0005$)

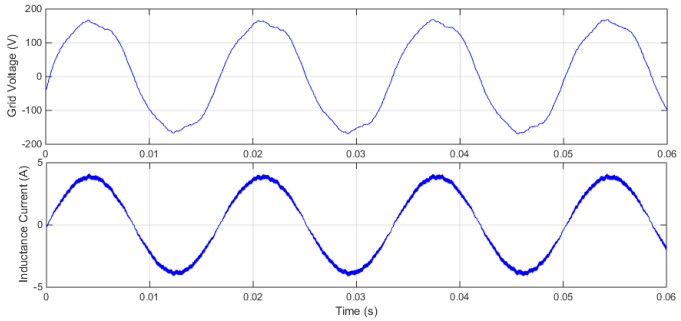

Fig. 12. Output voltage and output current when $L_g = 19.5$ mH ($\tau_i = 0.01$)

TABLE III
OUTPUT CURRENT HARMONIC ANALYSIS

Harmonic Order	$L_g = 6.5$ mH		$L_g = 19.5$ mH	
	$\tau_i = 0.0005$	$\tau_i = 0.01$	$\tau_i = 0.0005$	$\tau_i = 0.01$
3rd	0.52%	0.74%	0.74%	0.98%
5th	0.34%	0.29%	0.14%	0.49%
7th	0.37%	0.46%	0.28%	0.45%
9th	0.14%	0.25%	0.28%	0.40%
11th	0.05%	0.01%	0.20%	0.12%
13th	0.15%	0.10%	0.11%	0.04%
THD	3.51%	3.77%	4.51%	4.83%

IV. EXPERIMENTAL RESULTS

A 1 kW Texas Instruments single-phase grid connected inverter with an *LC* filter was utilized for the experimental

investigation. An ideal and a distorted grid voltage were simulated using a programmable AC source. In order to examine the effect of the grid impedance, an adjustable impedance is inserted between the inverter and the AC source. The measured single-phase inverter output voltage and output current are presented in Fig.13- Fig. 22. The inverter output current harmonics measured by Tektronix oscilloscope are given in Table IV and Table VII. Under the ideal grid, the THD of inverter output current was reduced from 4.94% to 4.65% by increasing the proportional gain of current controller when the grid impedance is 19.5 mH. The output voltage and output current without PI controller is also measured for comparison, which demonstrate the current distortion can be improved by shaping PI controller parameters. The THD of the inverter output current was decreased from 5.09% to 4.73% by decreasing the integral gain of the current controller when L_g is 19.5 mH. Under the distorted grid, the THD of inverter output current was reduced from 5.21% to 4.69% by increasing the proportional gain of current controller when the grid impedance is 19.5 mH. The THD of the inverter output current was decreased from 5.28% to 4.74% by decreasing the integral gain of the current controller. As can be seen from these results, the THD of the inverter output current can be reduced by adjusting the PI controller gains. Because the single-phase inverter is connected to the AC source through a transformer and relay, which makes the grid side inductance larger than the grid impedance in the simulation, the THD of experimental results are higher than the THD of simulation results. But it's still in agreement with the theoretical analysis.

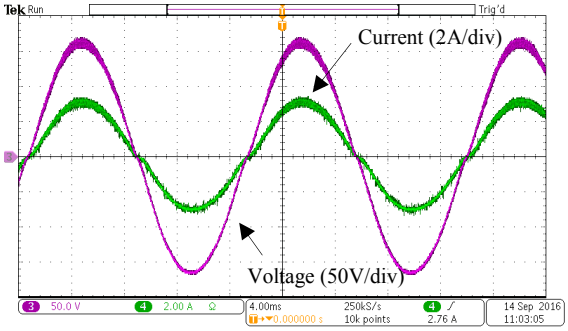

Fig. 13. Output voltage and output current when L_g = 19.5 mH (without PI)

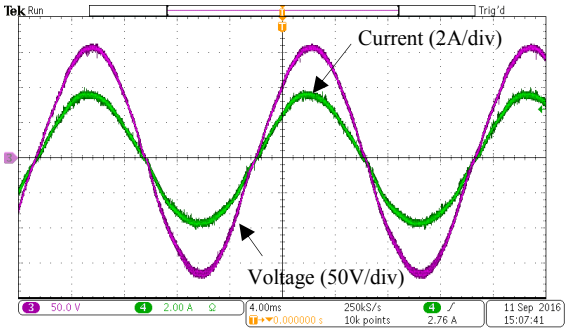

Fig. 14. Output voltage and output current when L_g = 19.5 mH (k_p = 2)

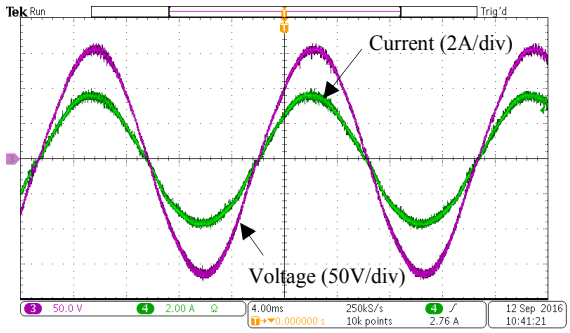

Fig. 15. Output voltage and output current when L_g = 19.5 mH (k_p = 3)

TABLE IV
OUTPUT CURRENT HARMONIC ANALYSIS

Harmonic Order	L_g = 6.5 mH			L_g = 19.5 mH		
	No PI	k_p = 2	k_p = 3	No PI	k_p = 2	k_p = 3
3rd	6.87%	2.34%	1.54%	7.29%	2.70%	1.55%
5th	5.53%	1.52%	0.91%	5.71%	1.63%	0.72%
7th	2.83%	1.77%	1.37%	2.64%	1.91%	1.67%
9th	1.70%	1.97%	1.61%	1.61%	2.20%	1.61%
11th	1.09%	1.00%	0.73%	1.09%	1.18%	0.86%
13th	1.03%	0.69%	0.77%	0.89%	0.91%	0.68%
THD	6.83%	4.85%	4.64%	6.61%	4.94%	4.65%

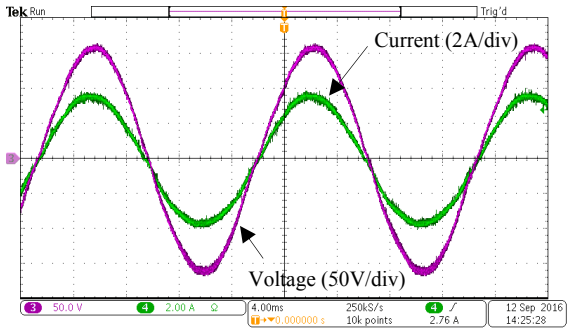

Fig. 16. Output voltage and output current when L_g = 19.5 mH (τ_i = 0.0005)

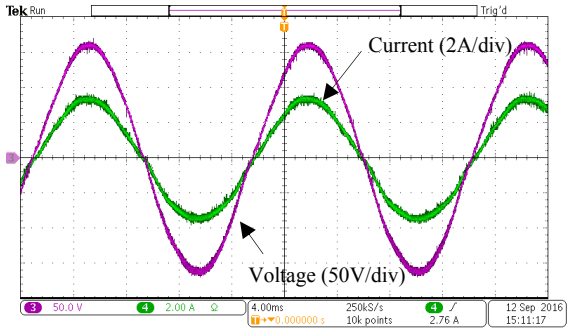

Fig. 17. Output voltage and output current when L_g = 19.5 mH (τ_i = 0.01)

TABLE V
OUTPUT CURRENT HARMONIC ANALYSIS

Harmonic Order	L_g = 6.5 mH		L_g = 19.5 mH	
	τ_i = 0.0005	τ_i = 0.01	τ_i = 0.0005	τ_i = 0.01
3rd	1.82%	2.29%	2.33%	2.05%
5th	0.98%	1.80%	0.92%	2.01%
7th	1.57%	2.02%	1.54%	1.77%
9th	2.13%	1.96%	1.58%	1.93%
11th	1.31%	0.72%	0.77%	0.63%
13th	0.94%	0.54%	0.54%	0.40%
THD	4.78%	5.28%	4.73%	5.09%

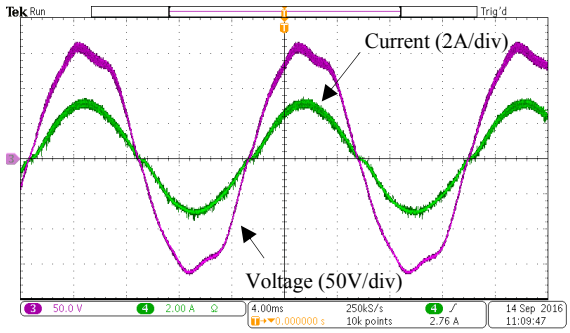

Fig. 18. Output voltage and output current when L_g = 19.5 mH (without PI)

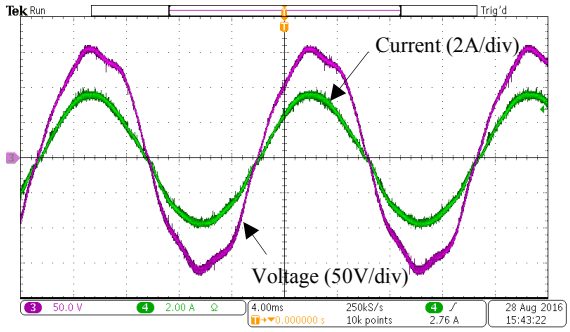

Fig. 19. Output voltage and output current when L_g = 19.5 mH (k_p = 2)

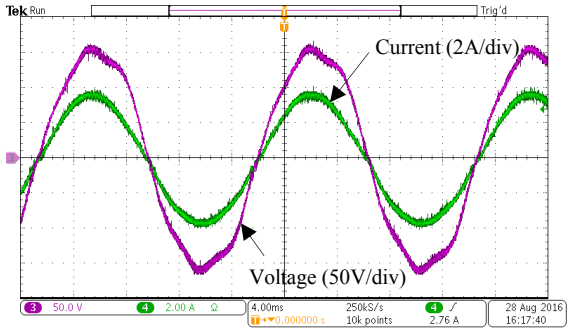

Fig. 20. Output voltage and output current when L_g = 19.5 mH (k_p = 3)

TABLE VI
OUTPUT CURRENT HARMONIC ANALYSIS

Harmonic Order	L_g = 6.5 mH			L_g = 19.5 mH		
	No PI	k_p = 2	k_p = 3	No PI	k_p = 2	k_p = 3
3rd	7.62%	3.80%	2.71%	8.10%	3.47%	2.39%
5th	3.56%	1.68%	1.52%	4.43%	1.92%	0.76%
7th	4.51%	1.90%	1.28%	3.90%	2.02%	1.24%
9th	1.64%	1.57%	1.14%	1.61%	1.95%	1.45%
11th	1.13%	0.85%	0.55%	1.09%	1.22%	0.94%
13th	1.05%	0.92%	0.52%	1.08%	0.74%	0.74%
THD	6.91%	5.09%	4.77%	6.86%	5.21%	4.69%

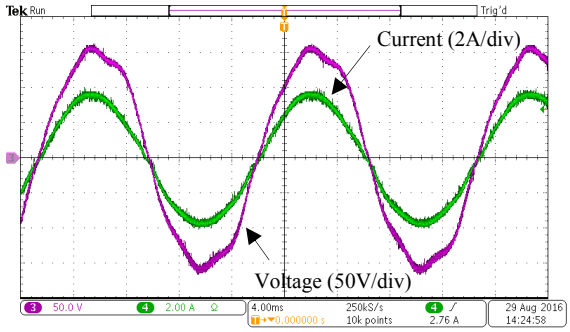

Fig. 21. Output voltage and output current when L_g = 19.5 mH (τ_i = 0.0005)

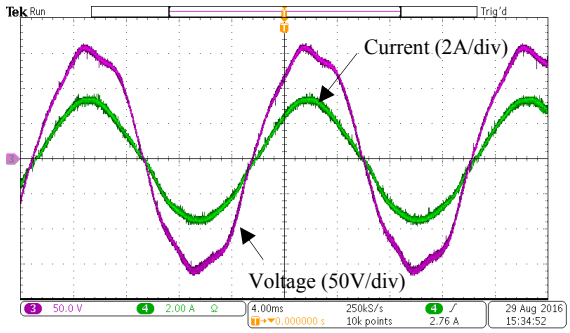

Fig. 22. Output voltage and output current when L_g = 19.5 mH (τ_i = 0.01)

TABLE VII
OUTPUT CURRENT HARMONIC ANALYSIS

Harmonic Order	L_g = 6.5 mH		L_g = 19.5 mH	
	τ_i = 0.0005	τ_i = 0.01	τ_i = 0.0005	τ_i = 0.01
3rd	2.78%	3.65%	2.75%	2.89%
5th	1.59%	1.51%	1.62%	1.06%
7th	1.36%	2.64%	1.59%	2.32%
9th	1.59%	1.67%	1.89%	1.71%
11th	1.06%	0.86%	0.85%	0.60%
13th	0.95%	0.89%	0.78%	0.58%
THD	4.85%	5.51%	4.74%	5.28%

V. CONCLUSION

Introduced in this paper is a method to increase the output impedance of a single-phase grid connected inverter with an *LC* filter to improve the stability and harmonic reduction ability of the system when the inverter is connected to a weak distorted grid. By modeling the output impedance of the inverter, the relationship between output impedance and grid impedance can be investigated. The grid impedance can degrade the control performance of the inverter and make the system less stable. In order to mitigate this effect, PI controller parameters are adjusted to increase the output impedance, which can improve the ability for the harmonic reduction and the stability of the system. Finally, simulation and experiment results for a 1 kW single-phase grid connected inverter with an *LC* filter verify the effectiveness of the proposed method.

REFERENCES

[1] Liserre, M., Teodorescu, R., Blaabjerg, F., "Stability of photovoltaic and wind turbine grid-connected inverters for a large set of grid impedance values," Power Electronics, IEEE Transactions on , vol.21, no.1, pp.263,272, Jan. 2006.

[2] Jian Sun, "Impedance-Based Stability Criterion for Grid-Connected Inverters," in Power Electronics, IEEE Transactions on , vol.26, no.11, pp.3075-3078, Nov. 2011.

[3] M. Céspedes and J. Sun, "Impedance shaping of three-phase grid-parallel voltage-source converters," *2012 Twenty-Seventh Annual IEEE Applied Power Electronics Conference and Exposition (APEC)*, Orlando, FL, 2012, pp. 754-760.

[4] D. Yang, X. Ruan and H. Wu, "Impedance Shaping of the Grid-Connected Inverter with LCL Filter to Improve Its Adaptability to the Weak Grid Condition," in *IEEE Transactions on Power Electronics*, vol. 29, no. 11, pp. 5795-5805, Nov. 2014.

[5] Xiao-Qiang Li, Xiao-Jie Wu, Yi-Wen Geng, and Qi Zhang; "Stability Analysis of Grid-Connected Inverters with an LCL Filter Considering Grid Impedance", Journal of Power Electronics, Vol. 13, No. 5, September 2013.

[6] V. Blasko and V. Kaura, "A novel control to actively damp resonance in input LC filter of a three phase voltage source converter," Applied *Power Electronics Conference and Exposition, 1996. APEC '96. Conference Proceedings 1996., Eleventh Annual*, San Jose, CA, 1996, pp. 545-551 vol.2.

[7] F. Wang, J. L. Duarte, M. A. M. Hendrix and P. F. Ribeiro, "Modeling and Analysis of Grid Harmonic Distortion Impact of Aggregated DG Inverters," in *IEEE Transactions on Power Electronics*, vol. 26, no. 3, pp. 786-797, March 2011.

[8] Y. Tao, Q. Liu, Y. Deng, X. Liu and X. He, "Analysis and Mitigation of Inverter Output Impedance Impacts for Distributed Energy Resource Interface," in *IEEE Transactions on Power Electronics*, vol. 30, no. 7, pp. 3563-3576, July 2015.

Jiao Jiao received her B.S. and M.S. degree in Electrical Engineering from China Agricultural University, Beijing, China, in 2011 and 2013, respectively. She is currently pursuing her Ph.D. degree in Electrical Engineering in the Electrical and Computer Engineering Department at Auburn University. Her current research interests include grid-connected inverter modeling, simulation and control.

R. M. Nelms (F'04) received the B.E.E. and M.S. degrees in electrical engineering from Auburn University, Auburn, AL, USA, in 1980 and 1982, respectively, and the Ph.D. degree in electrical engineering from Virginia Polytechnic Institute and State University, Blacksburg, VA, USA, in 1987. He is currently Professor and Chair of the Department of Electrical and Computer Engineering, Auburn University. His research interests are in power electronics, power systems, and electric machinery. Dr. Nelms is a registered Professional Engineer in Alabama. In 2004, he was named an IEEE Fellow "for technical leadership and contributions to applied power electronics."

Unidirectional Protection Strategy for Multi-terminal HVDC Grids

Ataollah Mokhberdoran, Nuno Silva, Helder Leite and Adriano Carvalho

***Abstract*—Protection issue is identified as the main drawback of emerging multi-terminal HVDC grids. Multi-terminal HVDC grid demands fast short circuit fault current interruption. Fast DC circuit breakers as a promising solution can be implemented as either bidirectional or unidirectional devices. In addition to less implementation cost, the unidirectional DC circuit breakers have less power losses as compared to the bidirectional devices. A protection strategy for multi-terminal HVDC grid based on the unidirectional breaking devices is discussed and assessed in this paper. The performance of unidirectional protection strategy is examined under different fault scenarios in a detailed four-terminal MMC-HVDC grid model. Furthermore, the impacts of unidirectional protection strategy on power converters and also current interruption and surge arrester ratings of the DC circuit breakers are discussed.**

***Index Terms*—DC circuit breaker, HVDC, Protection Device, Voltage Source Converter (VSC), Short-circuit.**

I. Introduction

INCREASING penetration of the clean energy resources has led to a demand for development of more efficient ways to transmit bulk amount of electrical energy over long distances. As a solution, high voltage direct current (HVDC) transmission technology has been employed by different project developers. Large offshore wind farms and onshore AC systems can be interconnected through multi-terminal HVDC (MT-HVDC) grid in order to share the harvested energy between various geographical areas and enhance the system reliability [1].
Voltage source converter (VSC) offers several technical benefits for application in the future MT-HVDC grid. The VSC technology was introduced by conventional two-level converter and has evolved into multilevel converter topologies [2]. Introduction of modular multilevel converter (MMC) paved the way for the application of VSC in HVDC transmission systems. Recently, different variants of the half-bridge MMC have been developed and employed in HVDC industry [3].
The conventional VSCs and the half-bridge MMC topologies are highly vulnerable against DC side short circuit fault due to behavior of IGBTs' antiparallel diodes. Although full-bridge MMCs and other fault-tolerant converters can solve this issue, their power losses and lack of protection selectivity have been identified as their application drawbacks. Moreover, these converters have not been tested practically in full-scale, yet [1].

The research leading to these results has received funding from the People Programme (Marie Curie Actions) of the European Unions Seventh Framework Programme (FP7/2007-2013) under REA grant n 317221.

Ataollah Mokhberdoran and Nuno Silva are with EFACEC Energia, S.A, Un. Switchgear and Automation, Rua Frederico Ulrich, PO Box 3078 4471-907, Maia, Portugal (e-mail: mokhber@fe.up.pt). Ataollah Mokhberdoran, Helder Leite and Adriano Carvalho are with the Department of Electrical and Computer Engineering of University of Porto, Portugal.

HVDC circuit breaker (DCCB) as a promising solution may solve the protection problem in the MT-HVDC grids [1], [4], [5], [6]. Fast DCCBs can be categorized as hybrid DC circuit breakers (HCBs) and solid-state DC circuit breakers (SSCBs). The SSCBs can interrupt the fault current in tens of micro-seconds whereas the interruption time in HCB is expected to be less than 3 ms [4], [5], [3]. Although the HCB interrupts the current fast enough and has acceptable power losses, its realization cost for MT-HVDC grid can be expensive due to the large number of required semiconductor switches [7].
DCCBs are usually considered to be bidirectional and hence interrupt the current in their forward and backward directions [4]. Unidirectional DCCBs (UCBs) conduct the current in their forward and backward directions whereas interrupts the current only in one direction. The application of a unidirectional SSCB in a point-to-point DC connection is investigated in [8] and a unidirectional current releasing DCCB has been proposed in [9]. The protection of radial offshore DC grid using UCBs has also been studied [10]. The main concern regarding the application of UCB in the MT-HVDC grid is its inability in interrupting the fault current flowing in its backward direction as it may occur in a DC bus short circuit fault scenario.
In this paper, a protection strategy based on the unidirectional HCBs (UHCB) is suggested for MT-HVDC grid. The suggested strategy tries to overcome the main drawback of UHCB. Protection logics for DC bus and transmission line faults are investigated. The performance of suggested strategy is examined through different fault scenarios in a four-terminal HVDC grid model. For DC bus fault scenario, two DCCB tripping schemes are considered. Moreover, the superiorities and limitations of unidirectional protection of the MT-HVDC grid are assessed. The impacts of suggested strategy on the MT-HVDC grid elements and the HCB are also studied.

II. Typical protection strategy

Three different protection strategies for the MT-HVDC grids are identified: 1) handshaking approach with AC breakers, 2) fault-tolerant converters with disconnector switches, 3) fast fault identification relays with fast DCCBs [1]. In this paper, the third protection strategy together with the HCBs are considered. The HCBs can be placed at ends of each transmission line and also at DC side of converters. Fig. 1 shows the typical bidirectional DCCBs (BCBs) arrangement and the protection zones in a three-terminal HVDC grid. CB_{xy} represents the DCCB attached to line L_{xy} close to bus B_x. Also, CB_{xx} represents the DCCB attached to VSC_x at bus B_x.

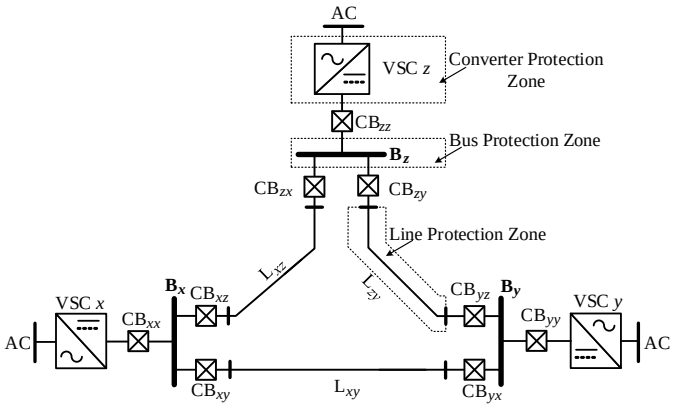

Fig. 1. BCBs arrangement in a multi-terminal HVDC grid

A. DC Bus Fault

Typically, a DC bus is protected by bus differential protection scheme. In the DC bus, sum of all incoming and outgoing currents must be zero. If a short circuit fault occurs at the DC bus, the sum of incoming and outgoing currents becomes non-zero. Therefore, DC bus trip signal can be generated if the sum of currents exceeds a near zero value. The differential protection scheme is quite fast and selective due to its low computing burden. The fault clearance in the DC bus zone can be done by opening all adjacent DCCBs. If the DC bus is connected to a converter, the converter DCCB should also be opened. Assume n transmission lines are connected to bus B_x. The protection logic can be given as (1).

$$Fault\ at\ \mathrm{B}_x \Rightarrow Trip(\mathrm{CB}_{x1}, ..., \mathrm{CB}_{xx}, ..., \mathrm{CB}_{xn}) \quad (1)$$

B. Transmission Line Fault

When using fast protection schemes transmission line cannot be protected by differential protective relays due to communication delay. Therefore, the transmission line is protected by communication-less non-unit protection schemes [11]. The non-unit protection schemes rely on local measurement of current, voltage, current derivative, voltage derivative or their combination [1]. If a fault is detected on the line, both DCCBs of faulty line should trip. The protection logic can be given as:

$$Fault\ on\ \mathrm{L}_{xy} \Rightarrow Trip(\mathrm{CB}_{xy}, \mathrm{CB}_{yx}) \quad (2)$$

III. Unidirectional Protection Strategy

Fig. 2(a) depicts the arrangement of UCBs in a three-terminal HVDC grid. The arrow in UCB symbol shows its current interruption direction. A protection strategy covering the DC bus and the transmission line zones based on the UCBs is suggested for the meshed HVDC grids in this section.

A. DC Bus Fault

Fig. 2(a) shows the fault currents during a short circuit fault at DC bus B_z. Three fault currents flow though three adjacent UCBs. Since the fault current i_{Fzz} flows in the forward direction of CB_{zz}, it can be interrupted by CB_{zz}. Fault

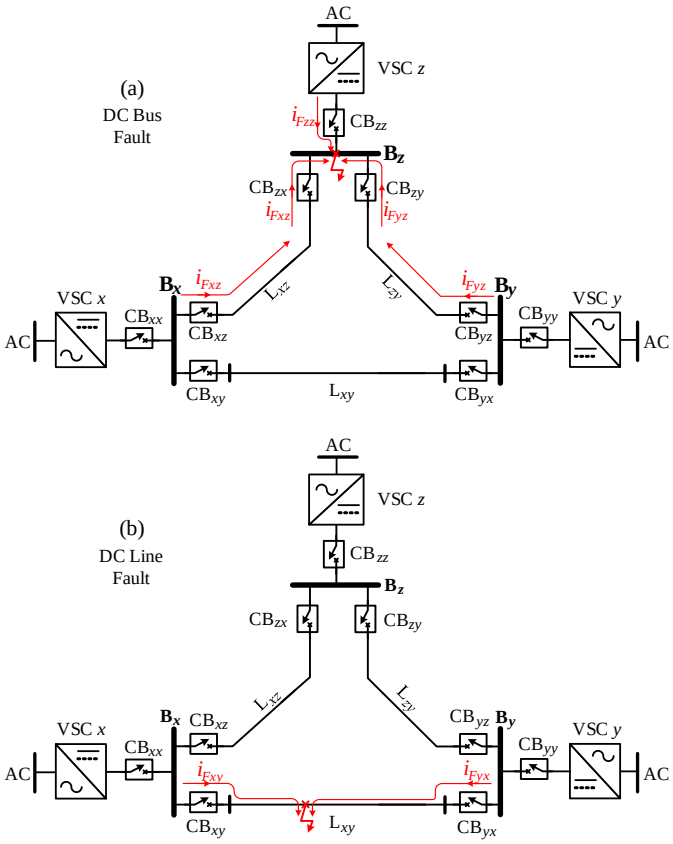

Fig. 2. UHCBs arrangement and directions and fault current directions (a) DC bus fault, (b) DC transmission line fault

currents i_{Fxz} and i_{Fyz} flow through the adjacent lines to the fault location and are in the backward directions of CB_{zx} and CB_{zy} and cannot be interrupted by them.
As shown in Fig. 2(a), i_{Fxz} flows in the forward direction of CB_{xz} and can be interrupted by this UCB, which is placed at the remote end of line. Any other fault current flowing from the adjacent lines can be interrupted by the remote UCB. The protection logic for the DC bus fault can be given by:

$$Fault\ at\ \mathrm{B}_x \Rightarrow Trip(\mathrm{CB}_{1x}, ..., \mathrm{CB}_{xx}, ..., \mathrm{CB}_{nx}) \quad (3)$$

The trip command for remote DCCB can be generated locally or communicated between two buses. In the communication-based method, fault detection is done locally in the faulted bus and the trip command is communicated to the remote DCCBs. On the other hand, the communication-less method relies on the fault detection at the remote buses. A fault at B_x can be detected by the remote DCCBs at the other buses of system either based on the non-unit protection or overcurrent protection schemes .

B. Transmission Line Fault

Fig. 2(b) shows a short circuit fault in line L_{xy}. Two fault currents flow from both ends of the transmission line into the fault location. In any line fault condition, the fault currents flow in the forward directions of corresponding UCBs. Therefore, the fault can be cleared by opening the corresponding

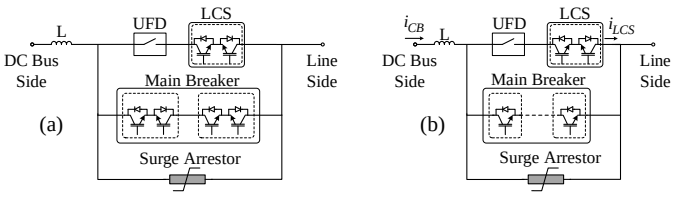

Fig. 3. Hybrid DC circuit breaker (a) typical HCB, (b) UHCB

UCBs. Unidirectional protection logic for transmission line fault is similar to (2).

IV. Hybrid DC Circuit Breaker

A. Typical Hybrid DC Circuit Breaker

The configuration of a typical HCB is depicted in Fig. 3(a) [12]. The main current conduction path contains a fast mechanical disconnector switch (UFD) in series with the load commutation switch (LCS) [5], [12]. The LCS is not required to block the nominal voltage and therefore, it has a lower voltage rating and can be realized by series connection of few semiconductor switches. Hence, the HCB has reasonable power dissipation whereas it is able to interrupt DC fault current quickly (around 2.5 ms) [5]. The parallel solid-state branch is the main breaker unit (MBU) during the fault condition. Voltage rating of the main breaker unit can be identified based on the transient recovery voltage (TRV) of the circuit breaker, which is usually limited by the reference voltage of surge arrester branch [12]. In order to allow bidirectional current flow and also bidirectional fault current interruption the semiconductor switches are connected in anti-series.

B. Unidirectional Hybrid DC Circuit Breaker

The topology of a unidirectional hybrid DC circuit breaker (UHCB) for the positive pole of HVDC system is depicted in Fig. 3(b). In the UHCB topology, two anti-series semiconductor switches are replaced by one switch. Therefore, the UHCB is only able to interrupt the fault current in the transmission line side. The normal power flow can be maintained in both forward and backward directions due to presence of antiparallel diodes. The UHCB requires half the number of semiconductor switches in its MBU as compared to the typical HCB [13].

The operation principles of UHCB for the transmission line fault are similar to the typical HCB. However, due to conduction of antiparallel diodes in the LCS unit of UHCB, similar operation sequence cannot be applied for the DC bus fault. Suggested operation flowchart for the UHCB is shown in Fig. 14. In the flowchart, i_{LCS} and i_{CB} represent the LCS unit current and UHCB current as it is illustrated in Fig. 3(b). In case of a line fault i_{LCS} is positive and therefore UHCB can activate the MBU for fault interruption. When i_{LCS} is negative, it means that the fault current flows in the backward direction of the UHCB. This case happens for UHCBs attached to a faulty DC bus. In this case, the LCS unit should be opened and commutate whole the fault current into the antiparallel diodes of MBU. Thereafter, the UFD can be opened. Note that the UHCB still conducts the fault current in its backward direction through the antiparallel diodes of MBU until the fault current is interrupted by the remote UHCB.

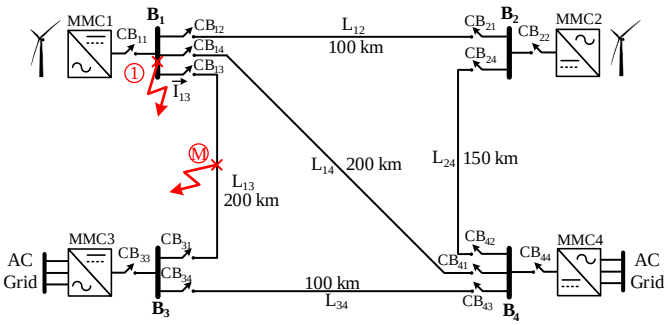

Fig. 4. Test multi-terminal HVDC grid

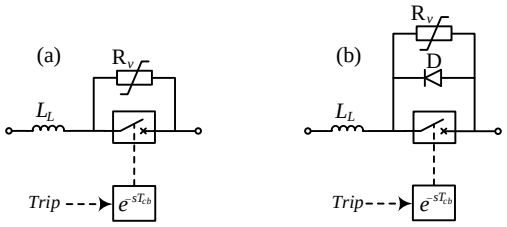

Fig. 5. Aggregated models (a) typical HCB, (b) UHCB

V. Test System

A. Meshed HVDC Grid

A four-terminal meshed HVDC grid model, which was proposed in [14] is used in this study. The system configuration is shown in Fig. 4. The studied model represents a cable-based meshed HVDC grid. The investigated system has a symmetric monopole HVDC configuration and includes four half-bridge MMCs. The MMCs are modeled by a continuous modeling approach with antiparallel diodes representing the blocking capability of the MMCs [14].

In the normal condition, MMCs 1 and 2 inject almost 700 MW into the grid and MMCs 3 and 4 absorb 600 and 800 MW, respectively. The blocking current threshold of MMCs is set to 3.2 kA in order to observe the MMC behavior without blocking during sever fault conditions. The parameters of four-terminal grid are illustrated in Table II.

B. DC Cable

HVDC transmission lines are modeled based on the XLPE insulated cable using frequency dependent modeling approach. The cable cross-sections and properties of material are illustrated in Fig. 15 and Table III, respectively [15].

C. Circuit Breaker Model

Since the internal operation of DCCB is not the subject of this paper, the aggregated models of HCB and UHCB are used. Fig. 5(a) and (b) depict the aggregated models of HCB and UHCB, respectively. As shown in Fig. 5(b) the UHCB model is derived from HCB model by adding one

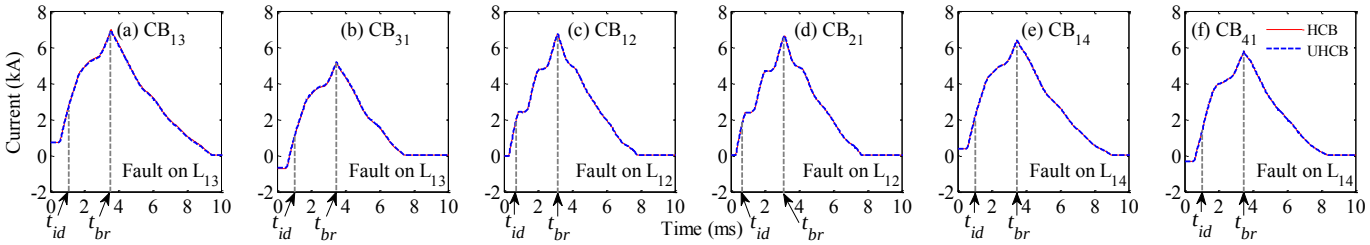

Fig. 6. Fault current for fault at middle of transmission line for BCBs and UCBs (a) fault on L_{13}, CB_{13} current, (b) fault on L_{31}, CB_{31} current, (c) fault on L_{12}, CB_{12} current, (d) fault on L_{21}, CB_{21} current, (e) fault on L_{14}, CB_{14} current, (e) fault on L_{41}, CB_{41} current

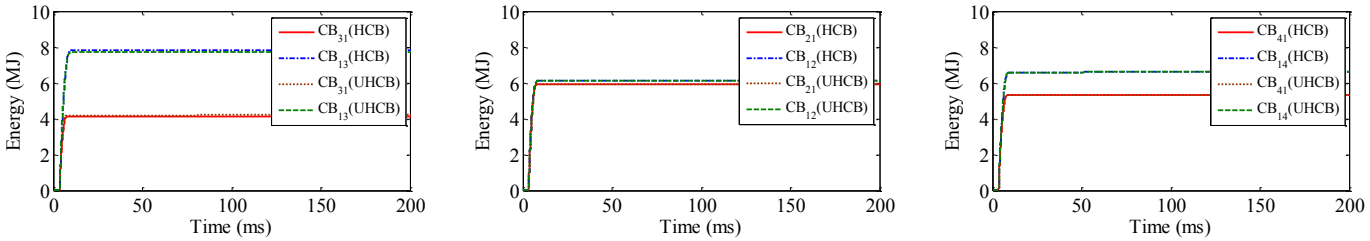

Fig. 7. Absorbed energy in surge arresters of BCBs and UCBs (a) CB_{13} and CB_{31}, (b) CB_{12} and CB_{21}, (c) CB_{14} and CB_{41}

parallel diode (D). The L_L, R_v and T_{cb} represent the limiting inductor, surge arrester and the circuit breaker operation time delay, respectively. The value of limiting inductor (L_L) of the line DCCBs is set to 100 mH. The L_L for the converter station DCCBs is set to 10 mH. The reference voltage of surge arresters is set to 480 kV. The HCB operation delay (T_{cb}) is set to 2.5 ms, which includes time delays in the LCS, UFD and MBU operations [5]. The trip command is received by the DCCB and breaker component interrupts the current independent of its value after a time delay equal to T_{cb}.

D. Protection system

The system performance is studied based on the typical and the suggested unidirectional protection strategies.

1) Typical protection strategy: A non-unit scheme, which has recently been proposed in [11] is employed for transmission line protection. The utilized method uses the local current measurements for line fault detection. The DC bus fault is detected by the differential protection scheme. The DC bus trip signal for fault is generated locally in typical protection strategy.

2) Unidirectional protection strategy: The mentioned non-unit scheme is also used in the unidirectional protection strategy. Two different schemes for the DC bus fault detection are considered in the unidirectional protection strategy: 1) local fault detection (communication-based), 2) remote overcurrent fault detection (communication-less).
In the first method a bus fault is detected by the bus differential relay and the trip command is communicated to the remote UHCBs. Communication time is modeled by a time delay block. In the second method a communication-less system is considered. The bus fault is detected at the remote healthy buses when the line current exceeds specific threshold.

TABLE I
TRIP TIMES OF DIFFERENT TYPES OF DC CIRCUIT BREAKERS FOR DC BUS AND TRANSMISSION LINE FAULTS

DCCB	Trip time (t_{id}) [ms]							
	Fault at B_1		Fault on L_{12}		Fault on L_{13}		Fault on L_{14}	
	BCB	UCB	BCB	UCB	BCB	UCB	BCB	UCB
CB_{11}	0.1	0.1	-	-	-	-	-	-
CB_{12}	0.1	0.1	0.79	0.79	-	-	-	-
CB_{21}	5	1.5	0.66	0.66	-	-	-	-
CB_{13}	0.1	0.1	-	-	1.05	1.05	-	-
CB_{31}	10	2	-	-	0.95	0.95	-	-
CB_{14}	0.1	0.1	-	-	-		1.05	1.05
CB_{41}	10	2	-	-	-	-	0.95	0.95

VI. SIMULATION

The results from study of four fault scenarios are presented and compared in this section.

A. Transmission line fault

Transmission line fault is studied through three independent permanent pole-to-pole low impedance ($R_{fault} = 100\ m\Omega$) short circuit faults at the middle of lines L_{12}, L_{13}, L_{14}. The line fault is incepted at time 0 s. As discussed in section III, the line fault clearing process for UCBs and BCBs are the same. Therefore, to clear the line fault from the system DCCBs at both ends of the faulted line should trip. Fig. 6(a)-(f) show the current in DCCBs for the short circuit fault in different transmission lines. The currents in HCB and UHCB are the same. t_{idxy} and t_{brxy} represent the fault identification time and the DCCB action time for CB_{xy}, respectively. Note that the fault identification and the trip command generation are assumed to be simultaneous.
The numerical values of fault identification time are illustrated in Table I. Due to the longer length of L_{13} and L_{14}, the midpoint fault is detected later than the similar fault in L_{12}. Absorbed energy by the surge arrester of each DCCB is

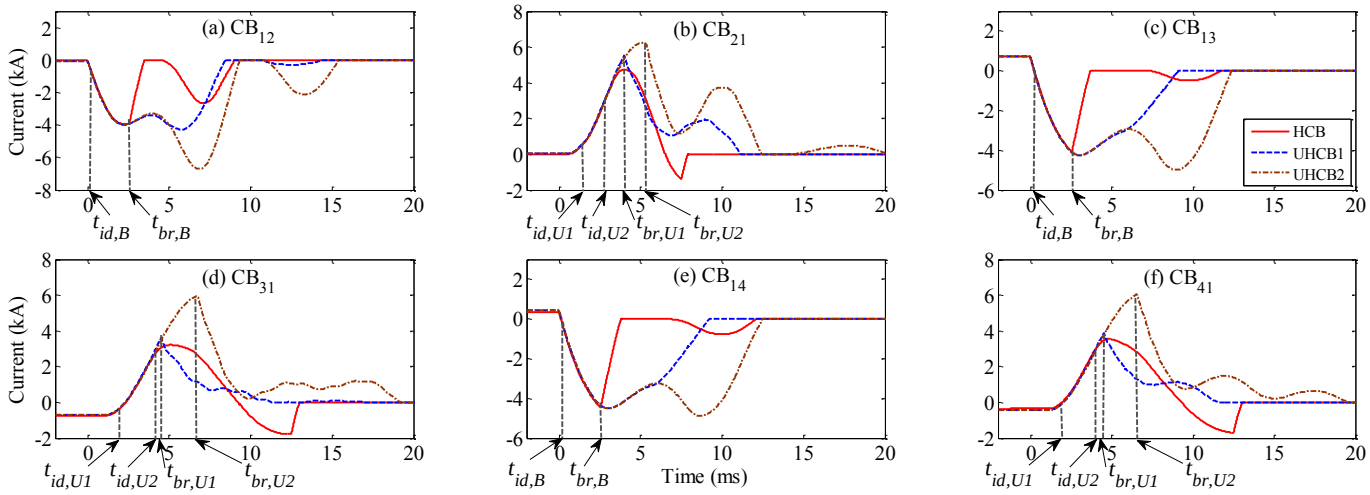

Fig. 8. Current in DCCB during fault at bus (B_1) for BCBs and UCBs (a) CB_{12}, (b) CB_{21}, (c) CB_{13}, (d) CB_{31}, (e) CB_{14}, (f) CB_{41}

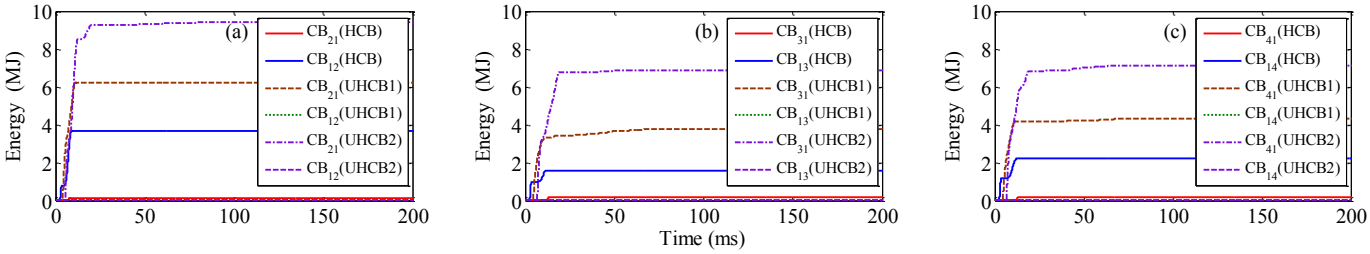

Fig. 9. Absorbed energy in surge arresters of BCBs and UCBs (a) CB_{12} and CB_{21}, (b) CB_{13} and CB_{31}, (c) CB_{14} and CB_{41}

depicted in Fig. 7. The difference in dissipated energy in the surge arresters is due to unequal interrupted fault currents in corresponding DCCBs and also different fault distances from DCCB. DCCBs with positive pre-fault current (pre-fault and fault currents are in the same direction) reach higher current than the DCCB with negative pre-fault current and therefore, larger amount of energy is dissipated in their surge arresters.

B. DC bus fault

During a bus fault in the MT-HVDC grid, due to the low inductance between the converter and fault location, high fault current flows in the DC side of the converter. The fault current may exceed the self-protection threshold of the MMC and cause the MMC blocking. Protection of converter against DC bus faults can rely on either AC side circuit breaker or the converter station DCCB. In this study, the MMC is protected by a DCCB at its DC side. A permanent pole-to-pole low impedance ($R_{fault} = 100\ m\Omega$) short circuit fault is incepted at bus B_1 at time 0 s. In the typical bidirectional strategy upon fault detection by the differential scheme, CB_{11}, CB_{12}, CB_{13}, CB_{14} should trip and disconnect the adjacent lines from B_1. Therefore, terminal 1 of the MT-HVDC grid will be disconnected from rest of the system and consequently, the amount of harvested energy from generation nodes of system will be reduced. Hence, MMC 3 and 4 will absorb less power as compared to pre-fault conditions. The remote DCCBs of the adjacent lines trip after a longer time delay to disconnect the cables from healthy DC buses.

In the unidirectional protection strategy, upon fault detection at bus B_1 all adjacent UHCBs including CB_{11}, CB_{12}, CB_{13}, CB_{14} are opened. The fault currents flow in the backward directions of CB_{12}, CB_{13}, CB_{14} and these UHCBs are unable to interrupt the fault current. Therefore, based on 3, CB_{21}, CB_{31} and CB_{41} also should trip. The DC bus fault clearing is studied through two protection schemes as explained in subsection V-D2. In the communication-based method, communication delay is modeled by a time delay block. The time delay block represents sum of propagation and transmitter/receiver delays. The propagation delay is set to 5 μs/km and the transmitter/receiver delay is set to 1 ms [16]. The trip times of remote DCCBs are illustrated in Table I. The second method is an overcurrent protection scheme. The overcurrent thresholds are set to 3 kA for all lines.

Fig. 8(a)-(f) show currents of all DCCBs attached to the adjacent lines for three discussed protective schemes. In Fig. 8 HCB, UHCB1 and UHCB2 represents the bidirectional, communication-based and overcurrent-based unidirectional protective schemes, respectively. In addition, t_{id} and t_{br} represent fault identification and current interruption times for each protective scheme. Absorbed energy in the surge arrester of each DCCB is depicted in Fig. 9(a)-(c).

As can been in Fig. 8, current in CB_{21}, CB_{31} and CB_{41} reach higher values in overcurrent-based scheme as compared to the communication-based scheme. As seen in Fig. 8(a), (c) and (e), the HCBs interrupt the bus fault current before

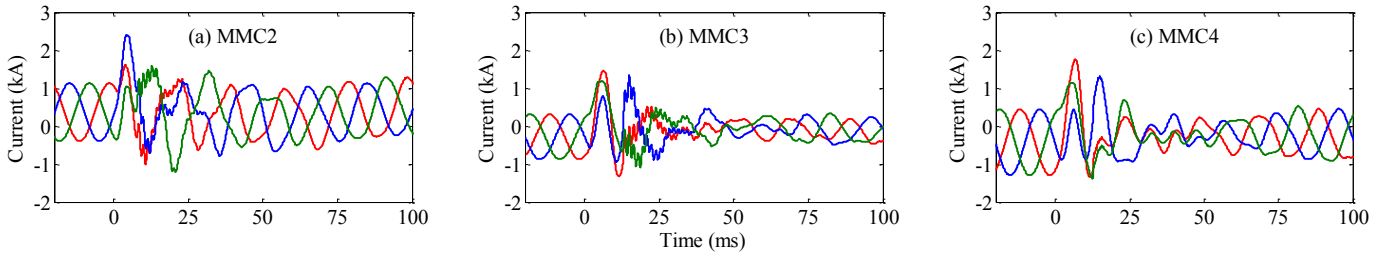

Fig. 10. The arm currents of MMCs in presence of BCBs (a) MMC2, (b) MMC3, (c) MMC4

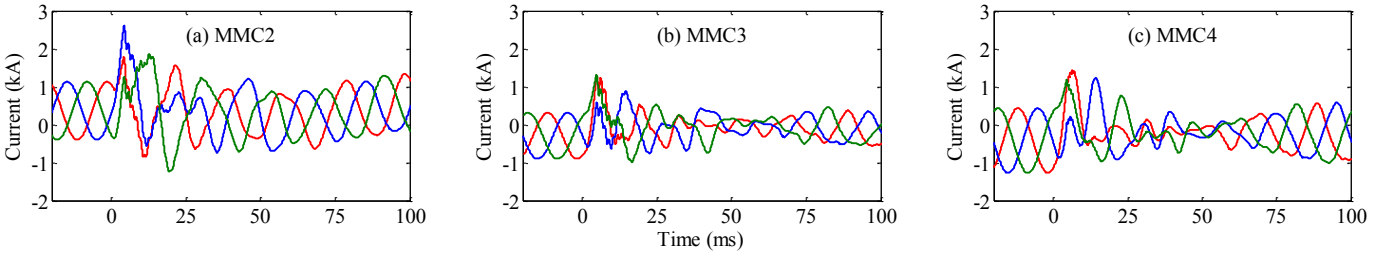

Fig. 11. The arm currents of MMCs in presence of UCBs (communication-based method) (a) MMC2, (b) MMC3, (c) MMC4

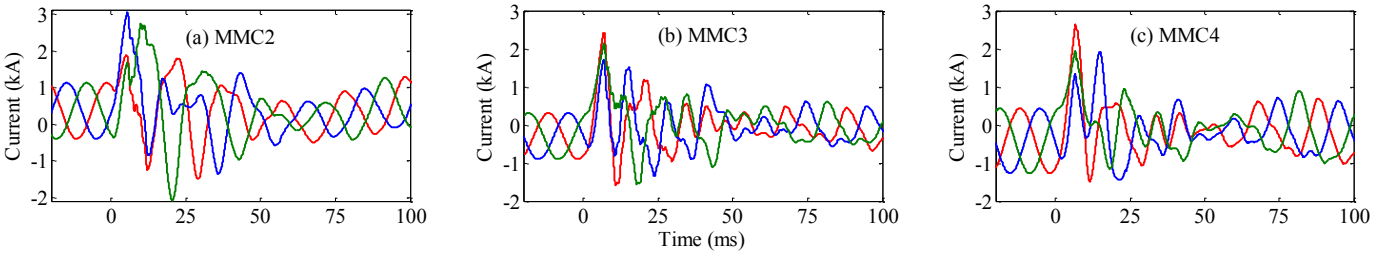

Fig. 12. The arm currents of MMCs in presence of UCBs (overcurrent-based method) (a) MMC2, (b) MMC3, (c) MMC4

reaching higher values. On the other hand, the remote UHCBs in the communication-based unidirectional protective scheme (UHCB1) also interrupt the bus fault current before reaching higher values. Due to higher interrupted current and larger cable inductance in unidirectional protection strategy, UHCBs' surge arresters absorb more energy than the HCBs.

Fig. 10 shows the MMC arm currents for healthy buses (MMC 2, 3 and 4) in presence of HCBs. In addition, the arm currents of MMC 2, 3 and 4 in presence of UHCBs for communication-based scheme are depicted in Fig. 11. Also, the arm currents of mentioned MMCs in presence of UHCBs for overcurrent-based scheme are illustrated in Fig. 12. The arm currents of MMC 1 are not included since this converter is isolated from the MT-HVDC grid due to converter station DCCB (CB_{11}) action during the DC bus fault.

VII. Discussion

A. Circuit breaker current rating

The maximum current in possible fault scenarios sets the requirements for DCCB current interruption rating.

1) Communication-based method: Due to lower inductance of short transmission lines, rate of rise of fault current in short lines is higher as compared to the long lines. Hence, the remote DCCBs in short lines might be required to interrupt higher current as compared to long lines. For instance, as can be seen in Fig. 8(b), the current in CB_{21} reaches almost 5.6 kA with unidirectional strategy while it does not exceed 3.9 kA in CB_{12} in the bidirectional strategy (see Fig. 8(a)). Note that the length of line L_{12} is 100 km. On the other hand, for line L_{13} (200 km), the current in CB_{31} reaches almost 3.8 kA with unidirectional strategy and it reaches almost 4 kA in CB_{13} in the bidirectional strategy (see Fig. 8(c) and (d)). The bus fault is cleared in longer time in communication-based unidirectional strategy as compared to the bidirectional strategy. Fig. 13(a) provides a comparison between the maximum interrupted current of different DCCBs during the DC bus and corresponding transmission line faults. As shown in the figure, the DCCBs are required to interrupt higher fault current during the line fault as compared to the DC bus fault in communication-based unidirectional protection strategy. Results of this study imply that the communication-based unidirectional scheme does not necessarily require DCCBs with higher current rating. Despite longer fault detection and trip times in the communication-based unidirectional scheme, the cable inductance and the DCCB current limiting inductor limit the rate of rise of fault current in the remote DCCB.

2) Overcurrent-based method: As can be seen in Fig. 8, the current in CB_{21}, CB_{31} and CB_{41} reach higher value in

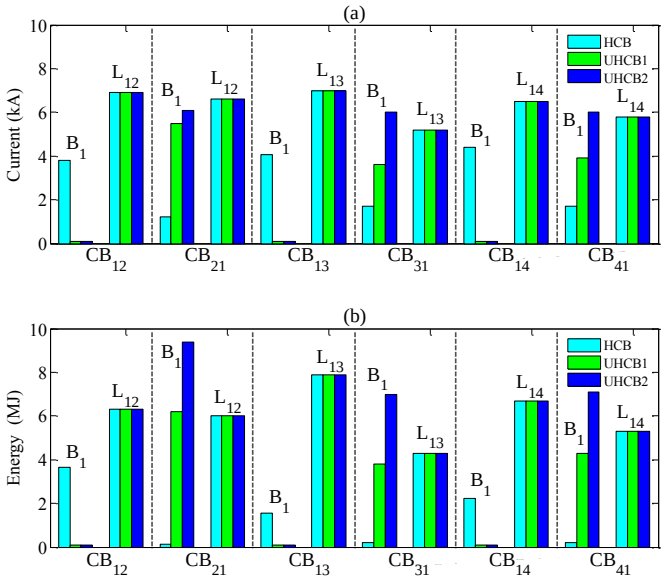

Fig. 13. (a) Maximum interrupted current and (b) absorbed energy in different DC circuit breakers during DC bus and line faults

overcurrent-based unidirectional scheme as compared to the current in CB_{12}, CB_{13} and CB_{14} in the bidirectional and the communication-based unidirectional schemes. The overcurrent protection threshold may be set to lower values in order to shorten the fault identification time if it is coordinated with the non-unit protection scheme. As shown in Fig. 13(a), the maximum interrupted current in CB_{31} and CB_{41} is slightly higher for the DC bus fault with overcurrent-based method as compared to the maximum interrupted current for corresponding transmission line faults. Hence, the UHCBs might be required to interrupt higher current as compared to the HCBs depending on the overcurrent protection parameters.

B. Surge arrester energy rating

1) Communication-based method: The amount of absorbed energy in the surge arrester of DCCB depends on the interrupted current value and the fault location distance from the DCCB. The magnitude of interrupted current has higher impact on the amount of absorbed energy. The absorbed energy in surge arresters of DCCBs during the transmission line and the DC bus faults are compared in Fig. 13(b). As can be seen, the surge arresters of UHCBs dissipate lower amount of energy during DC bus fault in communication-based unidirectional method as compared to corresponding transmission line fault. Note that the amount of absorbed energy in CB_{21} during bus fault is almost equal to the absorbed energy in CB_{12} during the line fault. These results imply that the energy rating of surge arresters for UHCBs with communication-based unidirectional strategy is not necessarily different than their energy rating for HCBs with the bidirectional strategy.

2) Overcurrent-based method: Due to the higher fault current during the DC bus fault in overcurrent-based method, the surge arresters dissipate higher amount of energy as compared to the line fault conditions (see Fig. 13(b)). Hence, the surge arresters in UHCBs with overcurrent-based method are required to be rated for higher energy absorption as compared to the HCBs with the typical strategy.

C. Impact on the converters

As seen in Fig. 10, Fig. 11 and Fig. 12, MMC 2 arm currents reach higher values as compared to the arm currents of other MMCs. MMC 2 is connected to the faulted bus (B_1) through a 100 km cable, which is shorter than other adjacent cables. Therefore, MMC 2 is more influenced by the fault transient as compared to the other MMCs. Furthermore, as can be seen in Fig. 12(a), one of MMC 2 arm currents reaches almost 3 kA, which would be higher than self-protection threshold level of MMC. Although in this study MMC 2 is not blocked, the application of unidirectional protection strategy may cause blocking of the MMCs connected to the faulted bus by a short transmission line. This issue can be avoided by either slight increase in the inductance of DCCBs limiting inductor or using IGBTs with higher current capability in MMCs.

D. Impact on DCCB

The MBU and LCS in the UHCB requires half the number of semiconductors as compared to the HCBs. For instance, an HCB with 320 kV and 9 kA voltage and current ratings requires 1416 IGBTs with 3.3 kV voltage rating in the MBU [7]. By applying unidirectional protection strategy this number can be reduced to 708 by mean of the UHCB. Due to the large number of required IGBTs by the HCB and considering the peripheral circuits and elements for each IGBT, this reduction can significantly decrease the initial investment for implementation of the HCBs.

VIII. Final Remarks

The UHCBs show technical and economic advantages thanks to their less initial and operational costs as compared to the typical HCBs. A unidirectional protection strategy for MT-HVDC grid is suggested in this paper. The results of study confirm that the unidirectional protection strategy can be utilized for protection of the MT-HVDC grid.

Two methods for remote DCCB tripping are considered: 1) communication-based and 2) overcurrent-based methods. The communication-based method shows better performance as compared to the overcurrent-based method.

The results of comparison study for different parameters of DCCBs imply that the current rating of DCCBs and the size of surge arresters are not necessarily different for the bidirectional and unidirectional strategies. However, the impact of suggested strategy on all converters of the grid, particularly the converters with shorter transmission line between them should be analyzed. In order to avoid blocking of the MMCs at healthy buses, slight increase in DCCB limiting inductor size or current rating of MMC's IGBTs might be required.

Application of unidirectional protection strategy may significantly reduce the number of required semiconductor switches in the MBU of HCBs. Considering the large number of required semiconductor switches by the HCB and also the peripheral circuits and elements of each semiconductor switch, this reduction can significantly decrease the initial investment for implementation of the HCBs.

APPENDIX

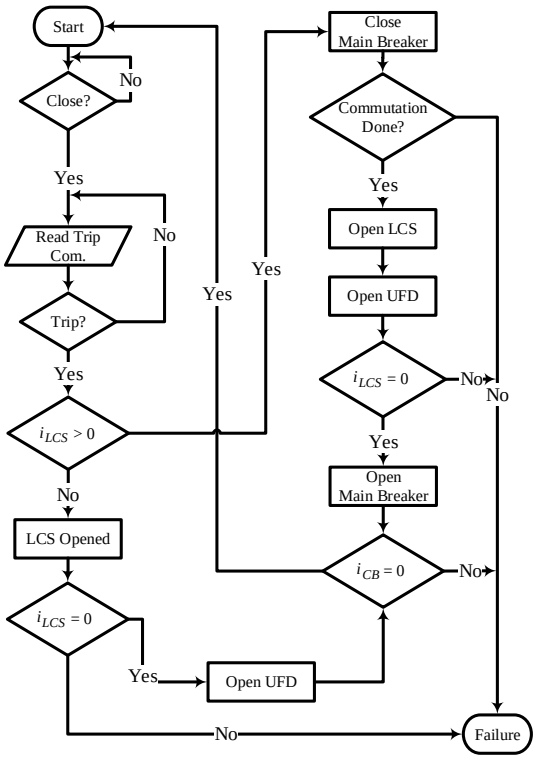

Fig. 14. Unidirectional hybrid DC circuit breaker operation logic flowchart

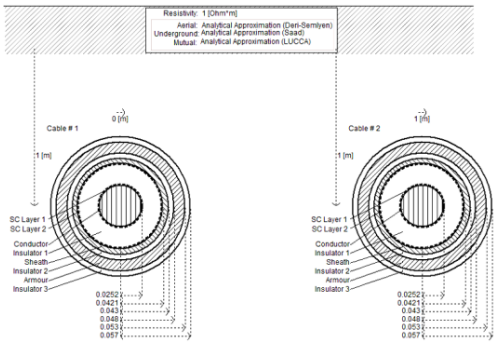

Fig. 15. Cross-section and configuration of the XLPE insulated HVDC cable

TABLE II
FOUR-TERMINAL HVDC SYSTEM PARAMETERS [14]

Parameter	Converter 1, 2, 3	Converter 4
Rated power	900 MVA	1200 MVA
AC grid voltage	400 kV	400 kV
Converter AC voltage	380 kV	380 kV
Transformer, u_k	0.15 pu	0.15 pu
Arm capacitance C_{arm}	29.3 μF	39 μF
Arm reactor L_{arm}	84.8 mH	63.6 mH
Arm,resistance R_{arm}	0.885 Ω	0.67 Ω
Bus filter reactor L_s	10 mH	10 mH

TABLE III
DC CABLE DATA [15]

Layer	Radius (mm)	Resistivity (m)	Rel. permeability	Rel. permittivity
(1) Core	25.2	1.72×10^{-8}	1	1
(2) Insulator	40.2	-	1	2.3
(3) Sheath	43.0	2.20×10^{-7}	1	1
(4) Insulator	48.0	-	1	2.3
(5) Armor	53.0	1.80×10^{-7}	10	1
(6) Insulator	57.0	-	1	2.1

REFERENCES

[1] N. Chaudhuri, B. Chaudhuri, R. Majumder, and A. Yazdani, *Multi-terminal direct-current grids: Modeling, analysis, and control*. John Wiley & Sons, 2014.

[2] A. Mokhberdoran and A. Ajami, "Symmetric and asymmetric design and implementation of new cascaded multilevel inverter topology," *IEEE Transactions on Power Electronics*, vol. 29, no. 12, pp. 6712–6724, Dec 2014.

[3] A. Mokhberdoran, A. Carvalho, N. Silva, H. Leite, and A. Carrapatoso, "Application study of superconducting fault current limiters in meshed hvdc grids protected by fast protection relays," *Electric Power Systems Research*, vol. 143, pp. 292 – 302, 2017.

[4] A. Mokhberdoran, A. Carvalho, H. Leite, and N. Silva, "A review on hvdc circuit breakers," in *Renewable Power Generation Conference (RPG 2014), 3rd*, Sept 2014, pp. 1–6.

[5] J. Häfner and B. Jacobson, "Proactive hybrid hvdc breakers - a key innovation for reliable hvdc grids," in *Electric system of the future - Integrating supergrids and microgrids international symposium, Italy*, Sept 2011, pp. 1–8.

[6] B. Geebelen, W. Leterme, and D. V. Hertem, "Analysis of dc breaker requirements for different hvdc grid protection schemes," in *AC and DC Power Transmission, 11th IET International Conference on*, Feb 2015, pp. 1–7.

[7] G. Liu, F. Xu, Z. Xu, Z. Zhang, and G. Tang, "Assembly hvdc breaker for hvdc grids with modular multilevel converters," *IEEE Transactions on Power Electronics*, vol. PP, no. 99, pp. 1–1, 2016.

[8] K. Sano and M. Takasaki, "A surgeless solid-state dc circuit breaker for voltage-source-converter-based hvdc systems," *IEEE Transactions on Industry Applications*, vol. 50, no. 4, pp. 2690–2699, July 2014.

[9] A. Mokhberdoran, A. Carvalho, N. Silva, H. Leite, and A. Carrapatoso, "A new topology of fast solid-state hvdc circuit breaker for offshore wind integration applications," in *Power Electronics and Applications (EPE'15 ECCE-Europe), 2015 17th European Conference on*, Sept 2015, pp. 1–10.

[10] D. Jovcic, M. Taherbaneh, J. P. Taisne, and S. Nguefeu, "Offshore dc grids as an interconnection of radial systems: Protection and control aspects," *IEEE Transactions on Smart Grid*, vol. 6, no. 2, pp. 903–910, March 2015.

[11] S. P. Azad and D. V. Hertem, "A fast local bus current-based primary relaying algorithm for hvdc grids," *IEEE Transactions on Power Delivery*, vol. PP, no. 99, pp. 1–1, 2016.

[12] A. Hassanpoor, J. Häfner, and B. Jacobson, "Technical assessment of load commutation switch in hybrid hvdc breaker," *IEEE Transactions on Power Electronics*, vol. 30, no. 10, pp. 5393–5400, Oct 2015.

[13] A. Mokhberdoran, N. Silva, H. Leite, and A. Carvalho, "A directional protection strategy for multi-terminal vsc-hvdc grids," in *2016 IEEE 16th International Conference on Environment and Electrical Engineering (EEEIC)*, June 2016, pp. 1–6.

[14] W. Leterme, N. Ahmed, J. Beerten, L. Angquist, D. V. Hertem, and S. Norrga, "A new hvdc grid test system for hvdc grid dynamics and protection studies in emt-type software," in *AC and DC Power Transmission, 11th IET International Conference on*, Feb 2015, pp. 1–7.

[15] F. Mura, C. Meyer, and R. W. D. Doncker, "Stability analysis of high-power dc grids," *IEEE Transactions on Industry Applications*, vol. 46, no. 2, pp. 584–592, March 2010.

[16] S. C. F. Behrouz A. Forouzan, *Data Communications and Networking*. McGraw-Hill Forouzan Networking, 2007.

A Novel Identification Method of Thermal Resistances of Thermoelectric Modules Combining Electrical Characterization Under Constant Temperature and Heat Flow Conditions

Saima Siouane, Slaviša Jovanović and Philippe Poure

***Abstract*—The efficiency of a Thermoelectric Module (TEM) is not only influenced by the material properties, but also by the heat losses due to the internal and contact thermal resistances. In the literature, the material properties are mostly discussed, mainly to increase the well-known thermoelectric figure of merit ZT. Nevertheless, when a TEM is considered, the separate characterization of the materials of the p and n elements is not enough to have a suitable TEM electrical model and evaluate more precisely its efficiency. Only a few recent papers deal with thermal resistances and their influence on the TEM efficiency; mostly, the minimization of these resistances is recommended, without giving a way to determine their values. The aim of the present paper is to identify the internal and contact thermal resistances of a TEM by electrical characterization. Depending on the applications, the TEM can be used either under constant temperature gradient or constant heat flow conditions. The proposed identification approach is based on the theoretical electrical modeling of the TEM, in both conditions. It is simple to implement, because it is based only on open circuit test conditions. A single electrical measurement under both conditions (constant-temperature and constant-heat) is needed. Based on the theoretical electrical models, one can identify the internal and thermal resistances.**

***Index Terms*—Thermoelectric Module (TEM); thermal resistances; contact thermal resistance; electrical characterization; identification; electrical model.**

I. Introduction

FOR a small scale power production, a Thermoelectric Module (TEM) appears as the most promising solution. It has the advantages of no moving parts, high reliability, long lifetime being noiseless and environmentally friendly [1], [2]. A thermoelectric module is a solid state semiconductor device that converts heat into electricity by using the Seebeck effect. The TEM is made of p and n type semiconductor elements that are electrically connected in series, to generate a higher voltage, and thermally in parallel to keep each semiconductor element at the same thermal gradient. These elements are typically arranged in a planer array and sandwiched between two thermal ceramic plates, where heat is transferred between the hot and the cold sides [3]. Each junction formed by the p and n elements is connected to metal contacts (see Fig. 1). When an input heat flow Q_H is applied at the hot side, a temperature gradient is created between the hot and cold sides of the TEM, and therefore the appearance of an electrical current I is observed. This phenomenon is known as 'Seebeck effect'.

In Fig.1, T'_H and T'_C denote the external hot and cold sides temperatures applied to the TEM respectively, whereas T_H and T_C denotes the internal hot and cold sides temperatures applied to the p and n elements. Notice that the thermal gradient $\Delta T = T_H - T_C$ applied externally to the TEM is lower than the thermal gradient $\Delta T' = T'_H - T'_C$ across the p-n junction elements. This is due to the contact thermal resistance θ_c between the TEM's semiconductors and their metal contacts. This contact thermal resistance is considered in the TEM electrical modeling presented in this paper.

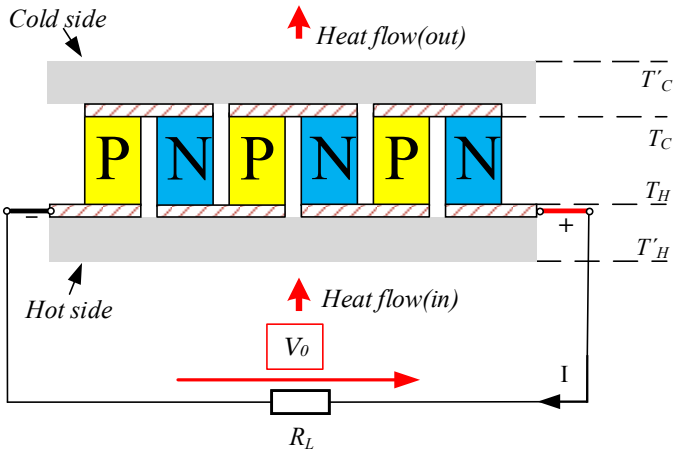

Fig. 1. General Structure of a TEM

Potential applications of thermoelectric modules are in thermal energy harvesting to power wireless sensors or microelectronic devices such as wearable medical sensors [4]. They can also be an energy source to power wristwatches [5]. Moreover, TEMs can also be combined with photovoltaic cells by first converting the solar energy into electricity and heat, and then using the wasted heat to generate electricity [6].

A thermoelectric module is subjected to a limit on its thermoelectric conversion efficiency (η), typically around 5% [7]. As a result, the applications of the thermoelectric module have been limited to specialized domains where the cost

Saima Siouane, Slaviša Jovanović and Philippe Poure, Institut Jean Lamour (UMR7198) Université de Lorraine, Vandoeuvre lès Nancy, France e-mail: (first_name.name@univ-lorraine.fr).

is a major consideration [8]. The thermoelectric conversion efficiency is defined as the ratio between the energy supplied to the load P and the heat energy Q_H absorbed at the hot junction of a TEM:

$$\eta = \frac{P}{Q_H} \tag{1}$$

The enhancement of the thermoelectric module efficiency is related to the material properties [9]. The key to expanding the range of applications of thermoelectric modules is the development of more efficient materials by improving their internal physical properties [8]. The thermoelectric module efficiency is evaluated by the well-known figure of merit ZT defined as:

$$ZT = \frac{\alpha^2 \theta_m}{R_E} T \tag{2}$$

where α is the Seebeck coefficient, θ_m the internal thermal resistance, R_E the electrical resistance of the TEM, and T the average temperature given by:

$$T = \frac{T_H + T_C}{2} \tag{3}$$

A greater figure of merit ZT indicates more efficient thermoelectric materials [10] having a higher Seebeck coefficient, a lower electrical resistance despite of a higher internal thermal resistance.

Different thermoelectric materials have different values of figure of merit which limit their use to applications with specific temperature range. Fig. 2 [11] shows that for lower temperatures (200 to $400K$) bismuth telluride (Bi_2Te3) is preferred while for temperatures between 600 and $800K$ the material lead telluride ($PbTe$) is recommended. At higher temperatures (from 800 to $1300K$) silicon germanium ($SiGe$) is used [12], [13]. For all these materials and temperature ranges it holds that ZT is around 1 [14], [15].

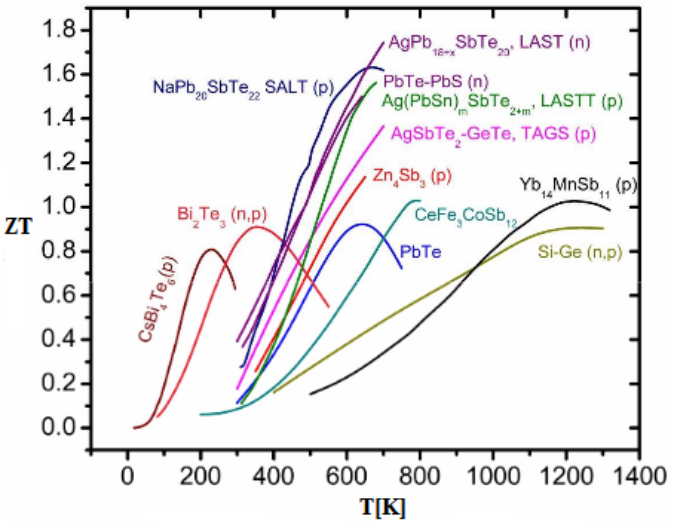

Fig. 2. Figure of merit ZT of different thermoelectric materials performing a function of temperature

Furthermore, the contact thermal resistance θ_c, which in bad designs may be of order of magnitude of the internal thermal resistance, can strongly influence the efficiency of a thermoelectric module [16], [17].

The aim of this paper is to identify, in addition to the material properties separately determined for each p and n element, the TEM parameters influencing its efficiency, mainly the internal and contact thermal resistances. Moreover, the knowledge of these parameters is mandatory for electrical modeling and simulation of the TEM. The influence of these parameters on the electrical modeling of the TEM under different operating conditions is detailed in [18].

This paper is built as follows. The electrical modeling of the thermoelectric module is described in Section II. In this section, two conditions are considered: constant temperature gradient and constant heat flow. Section III presents the approach used to identify the thermal resistances of a thermoelectric module using electrical characterization under open circuit conditions for both constant temperature gradient and constant heat flow conditions.

II. TEM ELECTRICAL MODELING

The electro-thermal model of a TEM is given in Fig. 3. The electrical part of the model is drawn in black whereas the thermal one is shown in purple. The contact thermal resistance can be modeled by two series resistors θ_c at the top and bottom of the TEM. The internal thermal resistance is called θ_m.

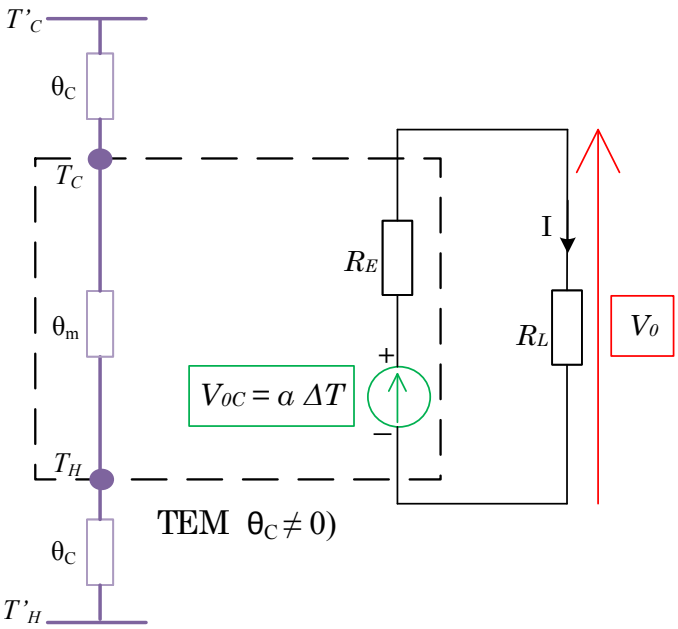

Fig. 3. Electro-thermal model of a TEM

A detailed view of the parameters used in the presented TEM model is shown in Table I.

In this section, the equivalent electrical model of a TEM under constant temperature gradient conditions is first described. Next, considering constant heat flow conditions, the electrical modeling of a TEM is also presented.

TABLE I
PARAMETERS OF THE TEM

Parameter	Description
R_E	TEM electrical resistance
θ_m	TEM internal thermal resistance
R_L	Load resistance
θ_c	Contact thermal resistance
α	Seebeck coefficient
T'_H	Temperature applied at the hot side of the TEM
T'_C	Temperature applied at the cold side the TEM
T_H	Hot side temperature at the terminals of p-n elements
T_C	Cold side temperature at the terminals of p-n elements
Q_H	Input heat flow
Q_C	Output heat flow

A. TEM modeling under constant temperature gradient conditions

In this case, the external thermal gradient $\Delta T' = T'_H - T'_C$ across the thermoelecrtic module is maintained constant. Due to the contact thermal resistance θ_c, the thermal gradient ΔT at the terminals of the p and n elements is decreased.

The heat flow rates through the hot side of the TEM (the input heat flow Q_H) and its cold side (the output heat flow Q_C), as shown in Fig. 1, are expressed respectively by Fourier's equations [20]–[22]:

$$Q_H = \frac{T_H - T_C}{\theta_m} + \alpha\, T_H I - \frac{1}{2} R_E I^2 \tag{4}$$

$$Q_C = \frac{T_H - T_C}{\theta_m} + \alpha\, T_C I + \frac{1}{2} R_E I^2 \tag{5}$$

By observing the electro-thermal model presented in Fig. 3 and applying the current-voltage analogy to the thermal part of the system where current and voltage correspond to heat flow and temperature respectively, the expression of the heat flow through the metal contacts on the hot and cold sides of the TEM can be formulated as:

$$Q_H = \frac{T'_H - T_H}{\theta_c} \tag{6}$$

$$Q_C = \frac{T_C - T'_C}{\theta_c} \tag{7}$$

The difference between the heat flows Q_H and Q_C provides the relationship between the heat flow difference and the power transmitted to the load R_L [16]:

$$Q_H - Q_C = \frac{T'_H - T_H}{\theta_c} - \frac{T_C - T'_C}{\theta_c} = V_O I \tag{8}$$

where V_O is the output voltage across the load R_L under constant temperature gradient conditions, and can be defined by:

$$V_O\Big|_{\Delta T' = cnst} = \alpha\, \Delta T\Big|_{\Delta T' = cnst} - R_E I \tag{9}$$

Knowing that $T_H = \Delta T + T_C$, the temperature applied at the cold side of the p and n elements is given by:

$$T_C = -\frac{\theta_c\, V_O I + \Delta T - T'_H - T'_C}{2} \tag{10}$$

By replacing the temperature T_C by its expression in Eq. 8, the expression of the thermal gradient at the terminals of the p and n elements with contact thermal resistances can be expressed by:

$$\Delta T\Big|_{\Delta T' = cnst} = \left(\frac{1}{\alpha\, \theta_c\, \theta_m\, I + \theta_m + 2\,\theta_c}\right) \times \{\theta_c\, \theta_m\, [(\alpha\, \theta_c\, V_O + R_E) I^2 + (V_O - \alpha\, (T'_H + T'_C)) I] + \theta_m\, \Delta T'\} \tag{11}$$

By substituting Eq. 9 in Eq. 11, the thermal gradient at the terminals of the p and n elements under constant temperature gradient conditions becomes:

$$\Delta T\Big|_{\Delta T' = cnst} = \left(\frac{1}{\alpha^2\, \theta_c^2\, \theta_m\, I^2 - \theta_m - 2\,\theta_c}\right) \times \{\alpha\, R_E\, \theta_c^2\, \theta_m\, I^3 + \alpha\, \theta_c\, \theta_m\, (T'_H + T'_C)\, I - \theta_m\, \Delta T'\} \tag{12}$$

By observing Eq. 12, it can be noticed that the temperature gradient ΔT seen by the p and n elements of the TEM is load current dependent. Thus, to identify it during the TEM functioning, not only the TEM's parameters should be known but also the connected load conditions. To simplify the ΔT measurement, and consequently the open circuit voltage generated by the TEM, open circuit conditions are usually chosen where the load R_L is disconnected from the TEM ($I = 0$), thus bringing Eq. 12 to a much simpler form of temperature divider.

The open circuit voltage generated by the TEM with contact thermal resistances under constant temperature gradient conditions is therefore given by:

$$V_{OC}\Big|_{\Delta T' = cnst} = \alpha \Delta T\Big|_{\Delta T' = cnst, I = 0} = \frac{\theta_m}{\theta_m + 2\,\theta_c} \alpha \Delta T' \tag{13}$$

Fig. 4 illustrates the open circuit voltage measurement of the TEM under constant temperature gradient conditions.

B. TEM modeling under constant heat flow conditions

Under constant heat flow conditions, the input heat flow Q_H applied to the hot side and the temperature T'_C at the cold side of the TEM are maintained constant [23].

The thermal gradient at the terminals of the p and n elements for the constant heat flow conditions can be expressed as:

$$\Delta T\Big|_{Q_H = cnst} = \frac{\frac{1}{2} R_E \theta_m I^2 - \alpha\, \theta_m T_C I + Q_H \theta_m}{1 + \alpha \theta_m I} \tag{14}$$

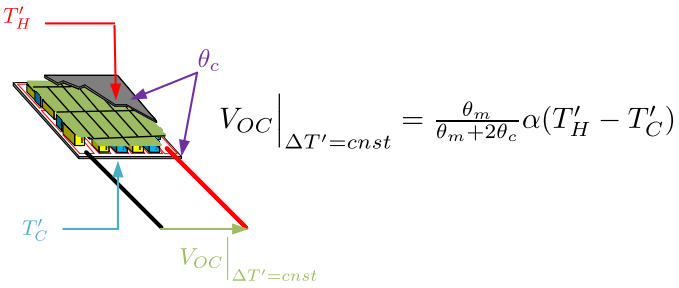

Fig. 4. Open circuit voltage measurement of the TEM under constant temperature gradient conditions

By substituting the expression of T_C derived in the previous section and given by Eq. 10 in Eq. 14, we obtain:

$$\Delta T\Big|_{Q_H=cnst} = \left(\frac{1}{\alpha\theta_m I+2}\right)\times \{(\theta_m(R_E+\alpha\,\theta_c V_O)I^2 - \alpha\theta_m(T'_H+T'_C)I +2Q_H\theta_m\} \tag{15}$$

In order to get the expression of the thermal gradient ΔT only as a function of Q_H and T'_C, T'_H should be first expressed as a function of these variables. By observing Fig. 3 from the previous section and taking the same current-voltage analogy, the input heat flow Q_H can be considered as the current flowing through the thermal resistances θ_m and θ_c connected in series. Thus, by using Eq. 6, the following expression can be obtained for T'_H:

$$T'_H = T_H + Q_H\theta_c = \Delta T + T_C + Q_H\theta_c \tag{16}$$

Similarly, using Eq. 8, we can write:

$$Q_H - \frac{T_C - T'_C}{\theta_c} = V_O I \tag{17}$$

which gives:

$$T_C = -\theta_c V_O I + T'_C + Q_H\theta_c \tag{18}$$

By substituting Eq. 18 in Eq. 16, and then the obtained result in Eq. 15, the thermal gradient ΔT at the terminals of the p and n elements with contact thermal resistances can be expressed with:

$$\Delta T\Big|_{Q_H=cnst} = \left(\frac{1}{1+\alpha\theta_m I}\right)\times \{\theta_m(\tfrac{1}{2}R_E+\alpha\,\theta_c V_O)I^2 - \alpha\theta_m(T'_C+Q_H\theta_c)I +Q_H\theta_m\} \tag{19}$$

Knowing that the output voltage of the TEM under constant heat flow conditions is given by:

$$V_O\Big|_{Q_H=cnst} = \alpha\,\Delta T\Big|_{Q_H=cnst} - R_E I \tag{20}$$

and by replacing Eq.20 in Eq. 19, the expression of the thermal gradient at the terminals of the p and n elements under constant heat flow conditions becomes:

$$\Delta T\Big|_{Q_H=cnst} = \left(\frac{1}{\alpha^2\theta_c\theta_m I^2 - \alpha\theta_m I - 1}\right)\times (\alpha\theta_c\theta_m R_E I^3 - \frac{1}{2}\theta_m R_E I^2 + \alpha\theta_m(T'_C + Q_H\theta_c)I - Q_H\theta_m) \tag{21}$$

As it has been noticed for the constant temperature gradients conditions, the temperature gradient ΔT of the TEM under constant heat flow conditions is also load current dependent. To eliminate this load current dependence, only the open circuit conditions ($I = 0$) will be considered during the measurements.

Under constant heat flow conditions, the TEM can be also modeled by an equivalent constant voltage source V_{OC} in series with an equivalent internal resistance. Here, the open circuit voltage of the TEM is:

$$V_{oc}\Big|_{Q_H=cnst} = \alpha\Delta T\Big|_{Q_H=cnst,\, I=0} = \alpha\theta_m Q_H \tag{22}$$

Fig. 5 illustrates the open circuit voltage measurement of the TEM under constant heat flow conditions.

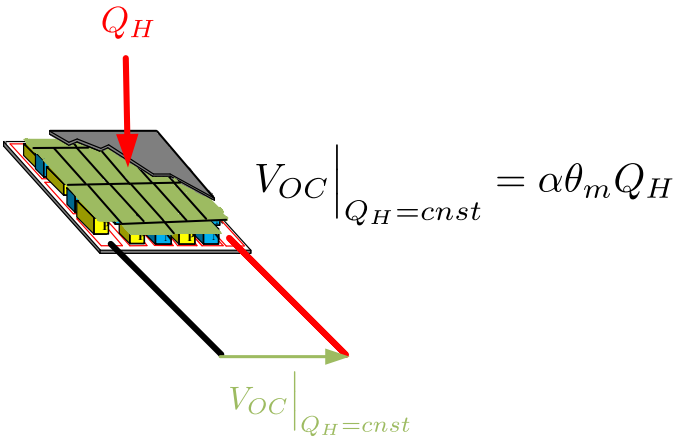

Fig. 5. Open circuit voltage measurement of the TEM under constant heat flow conditions

Based on Eqs. 13 and 22, giving the expressions of the open circuit voltages under both constant temperature gradient and constant heat flow conditions, one can identify the thermal resistances of the TEM only by measuring these two values, as described hereafter in the next section.

III. Identification of Thermal Resistances by Electrical Characterization

The theoretical thermal resistance θ_m of the TEM could be calculated from the following data, if they are provided by the manufacturer:

- ρ_{mp} the thermal resistivity of the p element.
- ρ_{mn} the thermal resistivity of the n element.
- N is the number of pairs of semiconductors of the TEM.
- A_p and A_n are the cross sectional areas of p and n elements, respectively.

- L_p and L_n are the length of p and n elements, respectively.

The analytical expression of θ_m is given by [24]:

$$\theta_m = \frac{\rho_{mp} L_p \rho_{mn} L_n}{N(\rho_{mp} L_p A_n + \rho_{mn} L_n A_p)}. \quad (23)$$

Notice that these data values are not always provided by the manufacturer. Nevertheless, in any case, the thermal resistance θ_m can be identified using electrical characterization. Based on the electrical model of the TEM under constant heat flow conditions, the open circuit voltage measurement allows us to find the value of θ_m by knowing the values of the Seebeck coefficient α and the input heat flow Q_H, and by using Eq. 22:

$$\theta_m = \frac{V_{oc}\Big|_{Q_H=cnst}}{\alpha Q_H}. \quad (24)$$

The value of α directly depends on the materials used for the TEM manufacturing and is given by:

$$\alpha = N(\alpha_p - \alpha_n). \quad (25)$$

where, α_p and α_n are the Seebeck coefficients of the p and n elements, respectively. One can notice that the values of α_p and α_n are mostly provided by the manufacturer.

In order to identify the contact thermal resistance θ_c, the open circuit voltage of the TEM under constant temperature gradient conditions must be measured. This allows us to determine the value of θ_c by substituting the value of θ_m previously determined (Eq. 24), and by knowing the value of the applied thermal gradient $\Delta T'$ (test conditions).

$$\theta_c = \frac{(\alpha \Delta T' - V_{oc}\Big|_{\Delta T'=cnst})\theta_m}{2V_{oc}\Big|_{\Delta T'=cnst}} \quad (26)$$

This approach of identifying the internal and contact thermal resistances of a TEM is summarized in Fig. 6. It is based on two open circuit voltage measurements, under both constant temperature gradient and constant heat flow conditions, respectively. The proposed method appears as an efficient and simple way for the TEM's thermal resistances identification.

IV. Conclusion

The Seebeck coefficient α of a TEM is generally provided by the manufacturer; in some cases, the θ_m value can also be calculated from the provided data. However, the value of the contact thermal resistance θ_c is not provided while it is required to electrically model the TEM and evaluate its efficiency. In this paper, the identification of the thermal resistances of a thermoelectric module is presented. To do this, some electrical characterizations are necessary. First, the measurement of the open circuit voltage of the TEM, under constant heat flow conditions, allows calculating the value of the internal thermal resistance θ_m. Second, the open circuit voltage of the TEM under constant temperature gradient conditions is measured. This measurement allows to calculate the value of the contact thermal resistance θ_c. Notice that

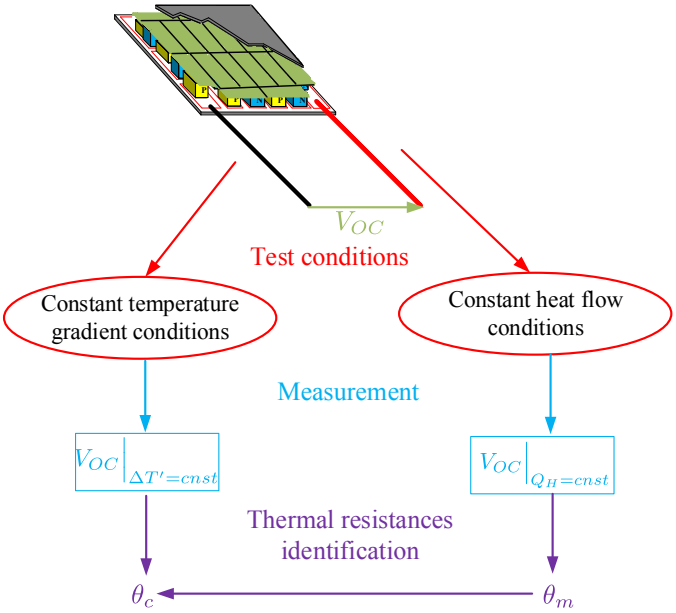

Fig. 6. Identification of internal and contact thermal resistances of the TEM

if the θ_m value is provided by the manufacturer or can be calculated based on the values of α_p and α_n, a single electrical test in open circuit and under constant temperature gradient conditions is needed. Moreover, in addition to the parameter identification, the equations of the electrical model of the TEM are given whatever the operating conditions and by taking into account the internal and contact thermal resistances (θ_m and θ_c).

References

[1] R. Ahiska and H. Mamur, "Design and implementation of a new portable thermoelectric generator for low geothermal temperatures," Renewable Power Generation, IET, Vol. 7, No. 6, pp. 700-706, 2013.

[2] C-T. Hsu, D-J. Yao, K-J. Ye and B. Yu, " Renewable energy of waste heat recovery system for automobiles," Journal of Renewable and Sustainable Energy, Vol. 2, No. 1, 2010.

[3] A. Dewan, S-U. Ay, M. N-Karim and H. Beyenal, "Alternative power sources for remote sensors: A review," Journal of Power Sources, Elsevier, vol. 245, pp. 129-143, 2014.

[4] J. P. Carmo, L. M. Gonalves and J. H. Correia, " Thermoelectric microconverter for energy harvesting systems," IEEE Transactions on Industrial Electronics, vol. 57, No.3, pp. 861-867, 2010.

[5] M. Kishi, H. Nemoto, T. Hamao, M. Yamamoto et al, " Micro thermoelectric modules and their application to wristwatches as an energy source," In IEEE International Conference on Thermoelectrics Eighteenth, pp. 301-307, 1999.

[6] D. Kraemer, B.Poudel, H. P. Feng, J. C. Caylor et al , " High-performance flat-panel solar thermoelectric generators with high thermal concentration," Nature materials, Vol. 10, no.7, pp. 532-538, 2011.

[7] S. Shanhe and C. Jincan, "Simulation investigation of high efficiency solar thermoelectric generators with inhomogeneously doped nanomaterials," IEEE Trans on indus elec, Vol. 62, No. 6, pp. 3569-3575, 2015.

[8] X-F. Zheng, C-X. Liu, Y-Y. Yan and Q. Wang, "A review of thermoelectrics researchRecent developments and potentials for sustainable and renewable energy applications," Renewable and Sustainable Energy Reviews, Vol.32, pp. 486-503, 2014.

[9] M-H. Elsheikh, D-A. Shnawah, M-F-M. Sabri, S-B-M. Said, M-H. Hassan, et al., "A review on thermoelectric renewable energy: Principle parameters that affect their performance," Renewable and Sustainable Energy Reviews, Vol. 30, pp. 337-355, 2014.

[10] S. Zhou, B-G. Sammakia, B. White and P. Borgesen, "A multiscale modeling of Thermoelectric Generators for conversion efficiency optimization," In Thermal and Thermomechanical Phenomena in Electronic

Systems (ITherm), 13th IEEE Intersociety Conference on pp. 985-992, 2012.
[11] O. Yamashita, N. Sadatomi, " Thermoelectric properties of Si1-xGex (x¡= 0.10) with alloy and dopant segregations," Journal of Applied Physics, Vol. 88, pp. 245-251, 2000.
[12] T. M Tritt , H. Bottner, L. Chen, " Thermoelectrics: direct solar thermal energy conversion," MRS Bull, Vol. 33, pp. 3668, 2008.
[13] D.M. Rowe, CRC handbook of thermoelectrics. London, NY, USA, CRC Press, 1995.
[14] B. Poudel, Q. Hao, Y. Ma, Y. Lan, A, Minnich, et al , "High-thermoelectric performance of nanostructured bismuth antimony telluride bulk alloys," Science, Vol. 320, pp. 634-638, 2008.
[15] W. G. J. H. M. Van Sark, "Feasibility of photovoltaicthermoelectric hybrid modules," Applied Energy, Vol. 88, No. 8, pp. 2785-2790, 2011.
[16] Saima Siouane, Slavisa Jovanovic and Philippe Poure, " Influence of contact thermal resistances on the Open Circuit Voltage MPPT method for Thermoelectric Generators", IEEE International Energy Conference - EnergyCon, Leuven, Belgium, April 4-8, 2016.
[17] B. Rasmus, "The Universal Influence of Contact Resistance on the Efficiency of a Thermoelectric Generator," Journal of electronic materials, Vol. 44, No. 8, pp. 2869-2876, 2015.
[18] Saima Siouane, Slavisa Jovanovic and Philippe Poure, " Fully electrical modeling of thermoelectric generators with contact thermal resistance under different operating conditions", Journal of electronic materials, pp. 1-11, 2016.
[19] M.-J. Dousti, A. Petraglia, and M. Pedram, "Accurate electrothermal modeling of Thermoelectric Generators," In Proceedings of the DATE, pp. 1603-1606, 2015.
[20] M. Freunek, M. Muller, T. Ungan, W. Walker and L-M. Reindl, "New physical model for thermoelectric generators," Journal of electronic materials, Vol. 38, No. 7, pp. 1214-1220, 2009.
[21] G. Fraisse, J. Ramousse, D. Sgorlon and C. Goupil, "Comparison of different modeling approaches for thermoelectric elements, Energy Conversion and Management," Elsevier, vol. 65, pp. 351-356, 2013.
[22] E-J. S.Rosado, S-J. Weinstein and R-J. Stevens, "On the Thomson effect in thermoelectric power devices," International Journal of Thermal Sciences, Elsevier, Vol. 67, pp. 5363, 2013.
[23] A. Montecucco, J. Siviter and A-R. Knox, "Constant heat characterisation and geometrical optimisation of thermoelectric generators," Elsevier, Applied Energy, Vol. 149, pp. 248-258, 2015.
[24] N. Karami and N. Moubayed, "New modeling approach and validation of a Thermoelectric Generators," 23rd IEEE In International symposium on industrial electronics (ISIE), pp. 586-591, 2014.

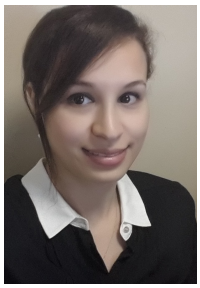

Saima Siouane was born in 1990. She received the Engineer Degree in Electronics from National Polytechnic School, Algiers, Algeria in 2013, the M.S. degree from National School of Engineering of Poitiers, France, in 2014. She is currently pursuing her Ph.D. degree in electronics for energy harvesting system at University of Lorraine - Institute Jean Lamour, Nancy, France.Her research interest mainly focuses on thermoelectric generator, low power DC-DC converter and fault tolerant systems.

Slaviša Jovanović received the B.S. in electrical engineering from the University of Belgrade, Serbia, in 2004, M.S. and Ph.D degrees in electrical engineering from the University of Lorraine, France, in 2006 and 2009, respectively. From 2009 to 2012, he was with the Diagnosis and Interventional Adaptive Imaging laboratory (IADI), Nancy, France, as a research engineer working on MRI-compatible sensing embedded systems. Then, he joined the Faculty of Sciences and Technologies and the Jean Lamour Institute (UMR 7198), University of Lorraine, Nancy, where he is currently an assistant professor. His main research interests include reconfigurable Network-on-Chips, energy harvesting circuits, neuromorphic architectures and algorithm-architecture matching for real-time signal processing. He is the author and co-author of more than 50 papers in conference proceedings and international peer-reviewed journals, and he holds one patent.

Philippe Poure was born in 1968. He received the Engineer Degree and Ph.D. Degree in Electrical Engineering from INPL-ENSEM-GREEN, France, in 1991 and 1995 respectively. From 1995 to 2004, he was an Associate Professor and worked at the University Louis Pasteur of Strasbourg, France, in the field of mixed-signal System-On-Chip for control and measurement in Electrical Engineering. Since September 2004, he joined the Universit de Lorraine, Nancy - France and works on fault tolerant power systems, FPGA based real time applications and energy havesting.

Reconditioning in synchronous operation with one parallel induction generator

Alana S. Magalhães[1,2], Pedro H. F. Moraes[1], Alan H. F. Silva[1,2], Pedro H. G. Gomes[1,2], Aylton J. Alves[1] , Wesley P. Calixto[1,2].

***Abstract*—The purpose of this paper is to compare mathematical modeling and practical bench in order to validate the electrical interactions between an induction generator and a synchronous generator. Two generators was connected to a common bus in steady state, subject to non-linear load. The results comparing modeling and bench tests show that the induction generator besides the active power increasing, has a better way for harmonic currents flowing in common bus. It was concluded that the induction generator repowering and attenuates current harmonic components present at the connection point, improving the network voltage profile.**

***Index Terms*—Repowering, Induction Generator, Synchronous Generator, Harmonics.**

I. INTRODUCTION

Repowering hydroelectric power plants has been increasing the power generated. Since there is spare capacity of turbine power and that is not being exploited by the generator already installed, it can be repowered. There are three possible ways to repowering: i) replacing the synchronous generator for a bigger one; ii) adding a second synchronous generator through double coupling on the turbine shaft; iii) adding a second generator coupled to the turbine shaft, but in this case an induction generator.

The induction generator is a viable technical and economical option to power generation [1]. The induction generator is used in electrical power plants repowering therefore has a low cost, is more robust, has simple construction, lower cost and less maintenance when compared to a synchronous machine. As disadvantage, external resources are required to compensate reactive power. On repowering, smaller induction generator is connected on a common bus to a larger synchronous generator and thus induction generator may have its reactive power compensated by synchronous generator, without power factor losses in the coupling point between them and can be dispensed of the control voltage, as this will be determined by system [2].

The induction generator besides low maintenance, does not require DC excitation and synchronization. In machines parallel operation is necessary to use of motorized thermomagnetic circuit breakers and in the case of induction generators, where the synchronization is not required, it reduces the cost of the circuit breaker [3]. In the distribution system the impact of induction generators connection is studied in [4]. To stabilize reactive field, the induction generator needs to reactive power on system input. The system supplies this reactive power, affecting losses and system voltage drops. The results show the relationship between losses due to change of the voltage profile, and as a solution indicates the power factor correction. The Hydro-Quebec system in Canada, the demand for small generators connection is increased [5].

Recently, study [6] shows that rural electrification can be supplied by small hydropower through induction generator and intelligent controllers in more economic schemes and cost-effective options. Studies in [7] compares the use of conventional synchronous machines together with the static frequency converter (SFC) in the Kadamparai plant with substitution by a variable speed induction generators to utilize the grid load variation effectively. The results show that the plant can be operated by variable speed machines.

The parallel operation voltage and frequency control was performed in [8], where induction generator can provide constant power and does not have excitation control. The synchronous generator has variable excitation in different load conditions. The results also show that changing the reactive load consumption can be supplied by the synchronous generator, keeping the voltage constant to 1 pu. The induction generator operates at full rating and does not respond does not respond to load change in the consumer.

In the interconnected electric power system *IEPS* there is presence of a large number of synchronous generating units of high power and non-linear loads. The application of rules aiming to limit the harmonic content of tensions on possible values of maintaining acceptable power quality is recommended [9]. In [10] is presented tests that induction generator does not introduce harmonics in power system. [11] shows the repowering system using the common bus two machines of the same power, a synchronous generator and an

A. S. Magalhães{1,2}, alanadsm@gmail.com
L. C. A. Junior{1}, leovir.engmecatronica@gmail.com
C. A. Matias{1}, calebeabrenhosa@gmail.com
A. H. F. Silva{1,2}, alanhfs@gmail.com
E. G. Domingues{1}, eldergd@ifgoias.edu.br
A. J. Alves{1}, aylton.alves@ifg.edu.br
W. P. Calixto{1,2}, wpcalixto@ieee.org
1Experimental and Technological Research and Study Group (NExT), Federal Institute of Goias (IFG), Goiânia, Brazil.
2 School of Electrical, Mechanical and Computer Engineering, Federal University of Goias (UFG), Goiânia Brasil.}

induction generator. The results show that the induction generator reduces harmonic content in the common bus.

In [13] proposed the development of a simulation model for repowering steam plant, providing dark areas of links aimed at accelerating the power system restoration process services.

Recently, [14] conduct a study to evaluate the economic and repowering prospects of a plant into disuse in the territory of Petralia Sottana (Sicily). The work shows that the refurbishment of the plant "Catarrate" contributes to the energy independence of the local community, with an estimated annual production of renewable energy of approximately 220 MWh and at the same time, the preservation of industrial heritage.

This paper aims to repowering the system. Furthermore, the objective is that the induction generator insertion in the common bus to a synchronous generator, can improve the sinusoidal profile of voltage and current. Thus, it is noted that the induction generator is still a preferential path for harmonic currents becoming protection synchronous generator, which is a more expensive and less robust machine that induction one.

II. Mathematical Modeling

A. Three-Phase Induction Generator under Non-Sinusoidal Steady State

Fig. 1 presents electrical circuit that models the induction machine in non-sinusoidal steady state, where X_E is stator leakage reactance and E_{ah} is the h order harmonic component of voltage, induced in Phase a machine stator, by the magnetic field produced by sinusoidal spatial distribution of rotating magneto-motive force of h order, fmm_{E0h} [12].

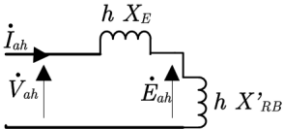

Fig. 1. Induction machine representative electrical circuit.

Considering odd values for h index, which are most likely harmonic components produced by non-linear loads, one can write:

$$\dot{V}_h = \dot{Z}_h \cdot \dot{I}_h \quad (1)$$

With such assumptions the equivalent circuit becomes purely inductive, and impedance $\dot{Z}_h$of the circuit is expressed by:

$$\dot{Z}_h = jh(X_E + k_R \cdot X'_{RB}) \quad (2)$$

As X'_{RB} has very similar value to X_E and $k_R$tends to one, can be a approach to accept $\dot{Z}_h$ to:

$$\dot{Z}_h \cong j2hX_E \quad (3)$$

Therefore, (1), (2) and (3), leads to:

$$\dot{V}_h \cong j2hX_E\dot{I}_h \quad (4)$$

B. Three-Phase Synchronous Generator under Non-Sinusoidal Steady State

For all phases of synchronous machine, and adopting usual nomenclature to represent harmonic reactance proposed in [12], we have (5) where r_E is per phase stator resistance, X_S is synchronous reactance at frequency ω and X_{af} is stator-rotor mutual reactance at frequency ω.

$$\dot{V}_h = [r_E + jhX_S] \cdot \dot{I}_h + j\frac{hX_{af}}{2} \cdot \dot{I}_{f(h)} \quad (5)$$

In practice $r_E \ll X_S$ and representing the last term by (6), leads to (7):

$$\dot{E}_h = j\frac{hX_{af}}{2} \cdot \dot{I}_{f_h} \quad (6)$$

$$\dot{V}_h \cong jhX_S\dot{I}_h + \dot{E}_h \quad (7)$$

Expression (7) suggests the circuit of Fig. 2.

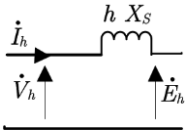

Fig. 2. Cylindrical rotor synchronous machine equivalent circuit.

From undertaken mathematical and physical analyzes, it is concluded that power flowing through terminals $\dot{E}_h$ is practically inductive reactive, therefore suggesting, there is only inductive impedance in circuit which relates $\dot{V}_h$ and $\dot{I}_h$, which may be represented by hX_S.

C. Association between Induction and Synchronous Generator

Assuming two machines, one synchronous and other an induction one, of same power, connected to same bus, Fig. 3, it is possible to make comparative analysis of harmonic current components in both.

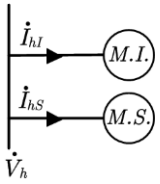

Fig. 3. Parallel machines.

Expressions (4), induction machine and (7), synchronous machine, can be rewritten as illustration of Fig. 3, and (8) and (9), respectively.

$$\dot{V}_h \cong j2hX_E\dot{I}_{hI} \quad (8)$$

$$\dot{V}_h \cong jh(X_S + X)\dot{I}_{hS} \quad (9)$$

Where X is equivalent reactance between terminals $\dot{E}_h$. Substituting (8) in (9) and through algebraic manipulation, it has:

$$\frac{\dot{I}_{hI}}{\dot{I}_{hS}} = \frac{X_S + X}{2 \cdot X_E} \quad (10)$$

Assuming threshold condition, where X is is negligible in comparison to X_S and $X_S = 10 \cdot X_E$, from (10) we have:

$$\frac{\dot{I}_{hI}}{\dot{I}_{hS}} = 5 \quad (11)$$

In expression (11) X_S represents phase leakage reactance of the synchronous machine, plus armature reaction, while X_E is stator leakage reactance of induction machine. By boundary condition, it is possible to ensure the inequality:

$$\dot{I}_{hI} > 5 \cdot \dot{I}_{hS} \quad (12)$$

In (12) it is conclude that in same bus, harmonic components of currents will flow with higher intensity to induction machine. This fact justifies the proposal of this work, of using induction machine as a means to absorb harmonic components of currents, attenuating its flow to synchronous machine. It follows that when the machine is seen only by the fundamental sinusoidal component, the power flowing in the rotor is almost exclusively active, while,

when viewed for a single harmonic component, the power flowing in the rotor is almost entirely inductive reactive. It allows to assume the intensities as irrelevant, or even the direction of electromagnetic torque (motor or generator), to simulate the conditions of harmonic mitigation in synchronous machine.

III. METHODOLOGY

The methodology will be developed in following steps:

i. Modeling the illustrated electrical system in Fig. 4 with the characteristics Tab. I;
ii. Conducting testing connected to common bus nonlinear load N_L;
iii. Conducting testing connected to common bus nonlinear load N_L and synchronous generator S_G;
iv. Conducting testing connected to common bus nonlinear load N_L, synchronous generator S_G and an induction generator I_G.
v. Conducting testing connected to common bus nonlinear load N_L and an induction generator I_G.

The power values will be recorded in meter M_1 in order to prove the increase in power output. For more information on harmonics attenuation, the harmonic content will be recorded at the point of measurement M_1, M_2, M_3 and M_4 to have better understanding of harmonic flows in the system.

A. Connection Machine and Loads for Case Study 1

Laboratory tests will be carried out, for *IEPS* shown in Fig. 4, where M_1, M_2, M_3, M_4 and M_5 are points for quantities measurements.

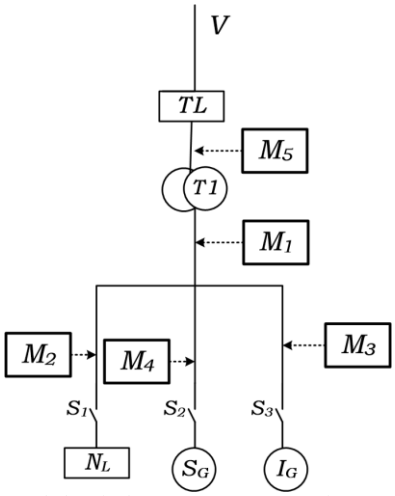

Fig. 4. Interconnected electrical power system - IEPS for Case Study 1.

Experimental tests of this work were performed in the laboratory with a system composed of two generating units, a synchronous and another induction. Both units are in parallel by feeding the first rectifier which constitute the nonlinear load. The N_L load is a resistive load of 500 watts, fed by a rectifier. To regulate properly the speed of generators, S_G and I_G, they used DC motors.

The Fig. 5 presents the equipment used in the laboratory.

Fig. 5. Equipments utilized in laboratory tests.

B. Connection Machine and Loads for Case Study 2

Laboratory tests will be carried out, for *IEPS* shown in Fig. 6, where M_1, M_2, M_3 and M_4 are points for quantities measurements.

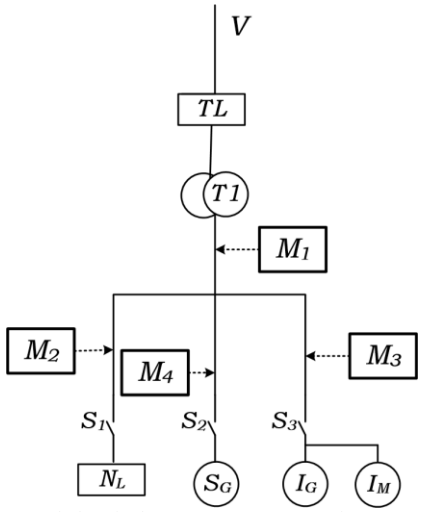

Fig. 6. Interconnected electrical power system - IEPS for Case Study 2.

Experimental tests of this work will be performed in the laboratory with system composed of two generating units, a synchronous and another induction. Both units will be in parallel by feeding nonlinear load N_L consisting of triac rectifier feeding sets of lamps. Two phases with total power of 5 kW and the third phase with 4kW. To regulate generators speed, S_G and I_G. were used diesel engine and induction motor with frequency inverter, respectively. Since the induction motor will be fed by the common bus, through S_3 key.

The Fig. 7 presents the equipment used in the laboratory, in which Fig. 7(a) the induction generator and Fig. 7(b) shows the synchronous generator.

(a) Induction Generator

(b) Synchronous Generator

Fig. 7. Equipments utilized in laboratory tests.

IV. RESULTS

A. Case Study 1

1) Experimental Tests

Components and values of *IEPS* of Fig. 4 are reported in the Tab. I, along with their values.

Table I. Acronyms and Values of the Components from IEPS.

Variable	Components	Components Values of Used
S_G	Synchronous Generator (main generator)	2kVA, 230V, three-phase, salient, 4poles, 60Hz
I_G	Induction Generator	2kVA, 220V, three-phase, cage rotor, 4poles, 60Hz
N_L	Nonlinear Load	500W three-phase, 380V, 60 Hz
T_1	Transformador	5kW, 380/220 V, Δ/Y aterrado
S_1, S_2, S_3	Interrupter	

The main objective of *IEPS* experimental testes is to obtain the increment of power generated plant at the measurement point M_1 and results of total harmonic distortion of current THD_i, measured in points M_1, M_2, M_3 and M_4, maintaining total harmonic distortion of voltage THD_v within standard limits.

The limit established by standard and presented in *IEEE-Std-519-1992*, [9], for voltage harmonic distortions, varies according to the voltage class in the measured point. In this case, as the measurement points has a 380 V voltage level, the limit of total harmonic distortion of voltage THD_v should be 5.0% and the limit of the individual distortion should be 3.0%.

2) Repowering

The Tab. II shows the operating conditions of the synchronous generator S_G and the induction generator I_G for experimental testing. The values of active, reactive and total power and power factor of the S_G and I_G were obtained in the measurement points and M_4 and M_3, respectively for loads N_L. The Tab. III present data of active, reactive and total power and power factor to the measuring point M_1 for the various configurations proposed to loads N_L.

Table II. Active, Reactive and Total Power and Power Factor in S_G e I_G for N_L.

Operation	P(W)	Q(VAr)	S(VA)	fp
S_G	-1085	-3595 I	3767	0.291
I_G	-1007	3783 C	3767	0.256

Table III. Active, Reactive and Total Power and Power Factor in M_1 *for* N_L.

Configuration	P(W)	Q(VAr)	S(VA)	fp
N_L	500	174.9 I	531.3	0.943
$S_G + N_L$	-681	-3379 I	3454	0.2
$S_G + I_G + N_L$	-1644	818 C	1865	0.92
$I_G + N_L$	-514	3949 C	3995	0.133

The Tab. III present the data powers in secondary side of the transformer for various configurations with two types of nonlinear load connected to the system. In the configuration where only N_L is connected, the network is providing active power of 500W. With the synchronous generator connection, configuration $S_G + N_L$, the network is providing active power of 681 W. Connecting the induction generator, setting $S_G + I_G + N_L$, the network is receiving active power of 1644 W. Note that with the inclusion of the induction generator is repowering of the system. Note also that the power factor in M_1 the configuration $S_G + I_G + N_L$ is 0.92.

3) Harmonics

The values shown in Tab. IV and Tab. V illustrate for a total harmonic distortion of voltage and for a total harmonic distortion of current to the measuring points M_1, M_2, M_3 , M_4 and M_5 , respectively.

By measuring M_1, presented in Tab. IV and Tab. V is observed that the value total harmonic distortion of voltage increases of 1.9% for 2.1% in the configuration $S_G + N_L$, and mitigates to 1.7% in $I_G + N_L$. In the setting $S_G + I_G + N_L$, mitigates the amount to 1.5%. The total harmonic distortion of current generated for the setting N_L in M_1 is 23.1%. In setting $S_G + N_L$ mitigates the value to 4.6% and setting $I_G + N_L$ mitigates the value to 5.6%. In the setting $S_G + I_G + N_L$ mitigates the amount to 12.1%. This proves that both the synchronous generator as induction generator mitigates the harmonic distortion in IEPS. In setting $S_G + I_G + N_L$ the value of THD_i is 2.8% in M_3 and 1.5% in M_4 and the value of THD_v is 1.5% in M_3 and 1.4% in M_4, showing that the induction generator behaves as a preferential path for harmonic.

Table IV. Values of *THDv* (%) in M_1, M_2, M_3 *e* M_4 with N_L.

	TDHv			
Configuração	M_5	M_1	M_3	M_4
CNL	1.7	1.9	-	-
SG+CNL	1.7	2.1	-	2.0
SG+IG+CNL	1.6	1.5	1.5	1.4
IG+CNL	1.7	1.7	1.7	-

Table V. Values of *THDi* (%) in M_1, M_2, M_3 *e* M_4 with N_L.

	TDHi			
Configuração	M_5	M_1	M_3	M_4
CNL	17.8	23.1	-	-
SG+CNL	4.3	4.6	-	1.8
SG+IG+CNL	17.9	15.4	2.8	1.5
IG+CNL	5.5	5.6	3.3	-

These results reaffirm the proposed use of induction generators to mitigate the harmonics in the main generators of power plants.

B. Case Study 2

1) Experimental Tests

Components and values of *IEPS* of Fig. 6 are reported in the

Tab. VI, along with their values.

Table VI. Acronyms and Values of the Components from IEPS.

Variable	Components	Components Values of Used
S_G	Synchronous Generator (main generator)	37kVA, 380V, three-phase, salient, 4poles, 60Hz
I_G	Induction Generator	7.5kVA, 380V, three-phase, cage rotor, 4poles, 60Hz
N_L	Nonlinear Load	14kW three-phase, 380V, 60 Hz
S_1, S_2, S_3	Interrupter	

2) Repowering

The operating conditions of synchronous generator S_G and induction generator I_G for experimental testing are presented in Tab. VII. The values of active, reactive and total power and power factor were obtained in measurement points M_4 and M_3, for loads N_L. The Tab. VIII present data of active, reactive and total power and power factor to measuring point M_1 for various configurations proposed to loads N_L. The excitement of synchronous generator was tuned to get the best power factor N_L on $S_G + I_G + N_L$ configuration.

Table VII. Active, Reactive and Total Power and Power Factor in S_G e I_G for N_L.

Operation	P(W)	Q(VAr)	S(VA)	fp
S_G	-23003	-7912	24343	0.945
I_G	-4011	4737	6214	0.645

Table VIII. Active, Reactive and Total Power and Power Factor in M_1 *for* N_L.

Configuration	P(W)	Q(VAr)	S(VA)	fp
N_L	1452	2996	5713	0.254
$S_G + N_L$	-21682	-4751	22699	0.955
$S_G + I_G + N_L$	-19847	-553	22011	0.895
$I_G + N_L$	2830	8985	13332	0.334

The Tab. VIII presents the data powers in secondary side of the transformer for various configurations with types of nonlinear load connected to system. In the configuration where only N_L is connected, the network is providing active power of 1452 W. In $S_G + N_L$ configuration, with synchronous generator connection, that provides active power of 23003 W, as Tab. VII. Network starts to receive active power of 21682 W in the case.

Connecting induction generator, setting $S_G + I_G + N_L$, the network is receiving active power of 19847 W. In this case, has a load receiving 452 W, synchronous generator providing 23003 W, induction generator providing 4011 W, as Tab. VII. The primary machine of induction generator, connected to S_3 key receive 5368 W. Note that with induction generator inclusion, the system is repowering. Note also that the power factor in M_1 the configuration $S_G + I_G + N_L$ is 0.895, this is due to the power factor of synchronous generator manufacturer that is 0.8.

3) Harmonics

The values shown in Tab. IX and Tab. X illustrate for a total harmonic distortion of voltage and for a total harmonic distortion of current to measuring points M_1, M_2, M_3 and M_4.

Table IX. Values of *THDv* (%) in M_1, M_2, M_3 *e* M_4 with N_L.

	TDHv			
Configuration	M_1	M_2	M_3	M_4
CNL	1.6	1.6	-	-
SG+CNL	1.5	1.5	-	-
SG+IG+CNL	1.5	1.5	1.5	1.4
IG+CNL	1.5	1.5	1.5	-

Table X. Values of *THDi* (%) in M_1, M_2, M_3 *e* M_4 with N_L.

	TDHi			
Configuration	M_1	M_2	M_3	M_4
CNL	137.9	137.9	-	-
SG+CNL	21.9	-	-	3.4
SG+IG+CNL	41.9	137	3.7	3.4
IG+CNL	81.2	137.1	3.5	-

By measuring M_1, presented in Tab. IX and Tab. X is observed that the value total harmonic distortion of voltage is 1.6% in N_L configuration and mitigates to 1.5% in configurations $S_G + N_L$, $I_G + N_L$, and $S_G + I_G + N_L$. The total harmonic distortion of current generated for the N_L setting in M_1 is 137.9%. In setting $S_G + N_L$ mitigates the value to 21.9% and setting $I_G + N_L$ mitigates the value to 41.9%. In the setting $S_G + I_G + N_L$ mitigates to 81.2%. This proves that both synchronous and induction generator decrease the harmonic distortion in *IEPS*. In setting $S_G + I_G + N_L$ the value of THD_i is 3.7% in M_3 and 3.4% in M_4 and the value of THD_v is 1.5% in M_3 and 1.4% in M_4, showing that the induction generator behaves as a preferential path for harmonic.

These results reaffirm the proposed use of induction generators to repowering and attenuation the harmonics in the main generators of power plants.

The Fig. 8 shows the current waveform with non-linear load connected in system. The total harmonic distortion of voltage THD_v and current THD_i with nonlinear load connected to system was 1.6% and 137.9%, respectively. All individual harmonics were significant with values above 18.1%, individual harmonic values are shown in Tab. XI.

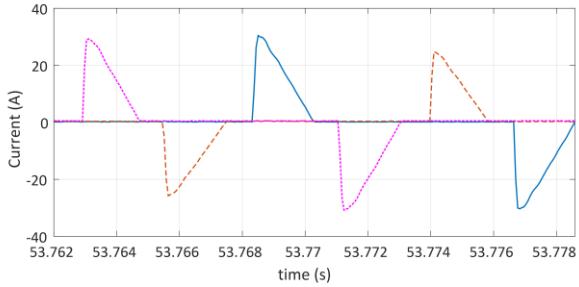

Fig. 8. Waveform in M_1 with THD_i- N_L connected.

Table XI. Values in M_1 with THD_i- N_L connected.

THD_v	1.6%		
THD_i	137.9%		
Harmonic	AB	BC	CA
60 Hz (Fnd))	100%	100%	100%
180 Hz (h^3)	89.2%	89.5%	89.4%
300 Hz (h^5)	70.0%	70.2%	70.8%
420 Hz (h^7)	48.1%	48.3%	49.3%
540 Hz (h^9)	29.9%	30.2%	30.6%
660 Hz (h^{11})	21.4%	21.1%	20.7%
780 Hz (h^{13})	20.7%	19.9%	19.1%
900 Hz (h^{15})	19.5%	18.8%	18.1%

The Fig. 9 shows the current waveform, after entry of synchronous generator with non-linear load connected to system. The total harmonic distortion of voltage THD_v and current THD_i after synchronous generator switching with a nonlinear load connected was 1.5% and 21.9%, respectively.

The total harmonic distortion of current THD_i attenuated from 137.9% to 21.9% and the most significant individual harmonic orders were the third order h_3 an attenuation from 89.5% to 14.1% and fifth order h_5 with an attenuation from 70.8% to 13.4%, the values of the other harmonics are listed in Tab. XII. The reduction is due to the fact that the synchronous generator is overexcited in order to supply reactive induction generator, while maintaining the power factor as close to 0.92 in M_1, when the configuration $S_G + I_G + N_L$.

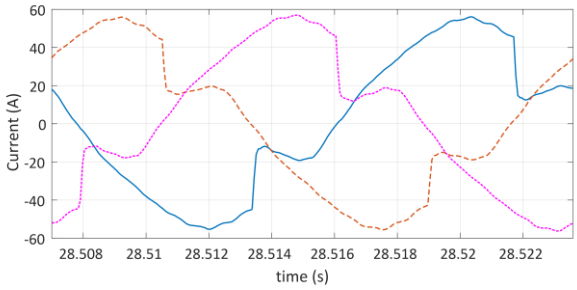

Fig. 9. Waveform in M_1 with THD_i- $S_G + N_L$ connected.

Table XII. Values in M_1 with THD_i- $S_G + N_L$ connected.

THD_v	1.5%		
THD_i	21.9%		
Harmonic	AB	BC	CA
60 Hz (Fnd))	100%	100%	100%
180 Hz (h^3)	13.7%	13.0%	14.1%
300 Hz (h^5)	13.4%	11.4%	13.0%
420 Hz (h^7)	8.3%	6.5%	8.3%
540 Hz (h^9)	5.0%	3.9%	4.7%
660 Hz (h^{11})	3.6%	2.7%	3.4%
780 Hz (h^{13})	3.0%	2.1%	2.7%
900 Hz (h^{15})	3.2%	2.3%	2.9%

The Fig. 10 shows the current waveform, after induction generator input with synchronous generator and non-linear load connected to system. The total harmonic distortion of voltage THD_v and current THD_i after induction generator switching with a synchronous generator and a nonlinear load connected was 1.5% and 41.9%, respectively. The total harmonic distortion of current THD_i increased from 21.9% to 41.9% and the most significant individual harmonic orders were the third order h_3 an increment from 14.1% to 45.6% and fifth order h_5 with an increment from 13.4% to 38.3%. The values of the other harmonics are listed in Tab. XIII. The purpose of this configuration is to keep the power factor as close to 0.92 in M_1, which means that there is reduction of harmonics in relation to the configuration N_L, but increase over the $S_G + N_L$.

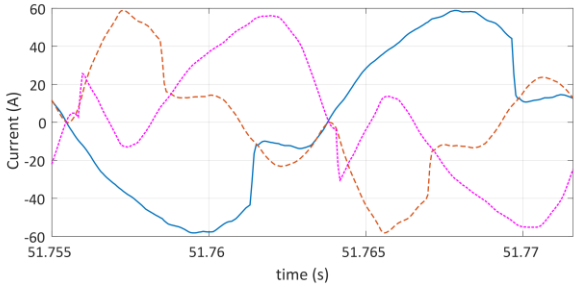

Fig. 10. Waveform in M_1 with THD_i- $S_G + I_G + N_L$ connected.

Table XIII. Values in M_1 with THD_i- $S_G + I_G + N_L$ connected.

THD_v	1.5%		
THD_i	41.9%		
Harmonic	AB	BC	CA
60 Hz (Fnd))	100%	100%	100%
180 Hz (h^3)	12.2%	35.3%	45.6%
300 Hz (h^5)	12.1%	38.3%	27.5%
420 Hz (h^7)	7.4%	0.6%	9.3%
540 Hz (h^9)	4.3%	8.3%	4.1%
660 Hz (h^{11})	3.1%	3.5%	1.4%
780 Hz (h^{13})	2.7%	2.2%	1.0%
900 Hz (h^{15})	2.8%	5.3%	1.6%

The Fig. 11 shows the current waveform, after entry of induction generator with non-linear load connected to system. The total harmonic distortion of voltage THD_v and current THD_i after synchonous generator swiching off, with the induction generator and a nonlinear load connected to system was 1.5% and 81.2%, respectively. The total harmonic distortion of current THD_i attenuated from 137.9% to 81.2% and the most significant individual harmonic orders were the third order h_3 an attenuation from 89.5% to 83.0% and fifth order h_5 with an increment from 70.8% to 76.6%, the values of the other harmonics are listed in Tab. XIV. It shows a decrease with respect to N_L configuration, but it is important to note that with induction generator connection there feeding of primary machine that increases distortion at M_3 measuring point. Furthermore, the induction generator is a smaller machine than the synchronous one.

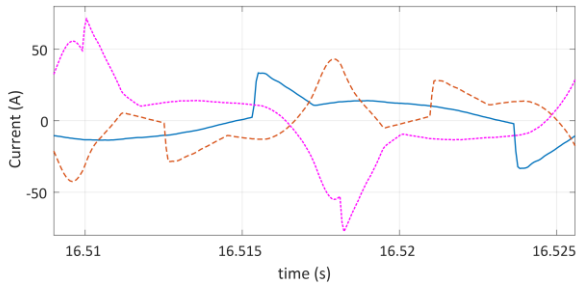

Fig. 11. Waveform in M_1 with THD_i- $I_G + N_L$ connected.

Table XIV. Values in M_1 with THD_i- $I_G + N_L$ connected.

THD_v	1.5%		
THD_i	81.2%		
Harmonic	AB	BC	CA
60 Hz (Fnd))	100%	100%	100%
180 Hz (h^3)	37.6%	83.0%	61.1%
300 Hz (h^5)	29.4%	76.6%	30.5%
420 Hz (h^7)	20.7%	5.8%	10.1%
540 Hz (h^9)	12.6%	20.6%	3.5%
660 Hz (h^{11})	9.1%	9.1%	1.0%
780 Hz (h^{13})	8.8%	6.8%	1.2%
900 Hz (h^{15})	8.3%	11.8%	2.1%

The individual harmonic distortion of current generated at M_1 is higher than N_L configuration. Both for $S_G + N_L$ setting as for $S_G + N_L$ there is an attenuation in individual distortions, to be more significant in configuration $S_G + N_L$.

It is necessary to conduct a detailed analysis $S_G + N_L$ and $I_G + N_L$ configurations, where it is important to consider that: i) the synchronous generator is configured to supply the reactive induction generator keeping the power factor as 0.92 in M_1, which makes work in the region where shows attenuation characteristic of harmonics; ii) at M_3 measuring

point is included the induction generator and the primary machine, increasing total harmonic distortion of this configuration, since the primary machine still has power biphasic and iii) the induction generator is active power machine approximately five times smaller than synchronous one.

V. CONCLUSIONS

This work confirmed through the results that induction generator in connection with a synchronous generator and a nonlinear load has the ability, to increase the power generated, available for the electrical system, besides increasing the power generation available for the electrical system, attenuating harmonic distortion current and voltage in commom bus. The induction machine besides showing low cost, robustness, simple construction, lower cost and less maintenance compared with synchronous machine, repowering the system. The results showed that harmonic distortion bus suffers reductions for synchronous generator connection as for induction generator connection. It is noted in results that induction generator provided a preferred path for current harmonic order, even when two machines produce or consume equivalent and proportional reactive power.

ACKNOWLEDGMENT

The authors would like to thank Coordination for the Improvement of Higher Education Personnel (CAPES), the National Counsel of Technological and Scientific Development (CNPq) and the Research Support Foundation of Goias State (FAPEG) for financial support research and scholarships.

REFERENCES

[1] J. M. Chapallaz; J. D. Ghali; P. Eichenberger and G. Fischer. "Manual on Motors Used as Generators". MHPG Series, Vol. 10, Friedr. Vieweg & Sohn Verlagsgesellschaft mbH, Germany.

[2] D. M. Medeiros. "The use of pumps operating as turbines and induction generators to generate electricity". Thesis in Portuguese, Federal University of Itajubá, Itajubá, Minas Gerais, Brazil, 2004.

[3] K. D Pham. "Cogeneration Application: Interconnection of Induction Generators with public Eletric Utility". Rural Electric Power Conference - REPC, 1991.

[4] V, Pongpornsup. "Impacts of Non-Utility Induction Generator to Distribution Network". IEEE Transmission and Distribution Conference and Exhibition, Vol. 2, Pages 1352-1356, 2002.

[5] R. Behome; M. Plamondon, H. Nakra, D. Desrosiers, C. Gagnon. "Case Study on the Integration of a Non-Utility Induction Generator to the Hydro-Quebec Distribution Network". IEEE Transactions on Power Delivery, Vol. 10, No. 3, 1995.

[6] J.A. Laghari, H. Mokhlis, A. H. A. Bakar, M. Hasmaini, "A comprehensive overview of new designs in the hydraulic, electrical equipments and controllers of mini hydro power plants making it cost effective technology". Renewable and Sustainable Energy Reviews, Vol. 20, Pages 279-293, 2013.

[7] N. Sivakumar, DAS. Devadutta, PADHY, N.P. Padhy. "Variable speed operation of reversible pump-turbines at Kadamparai pumped storage plant - A case study". Elsevier Energy Conversion and Management, Pages 96 - 104, 2014.

[8] P.J. Reddy, S.P. Singh, "Voltage and Frequency Control of Parallel Operated Synchronous and Induction Generators in Micro Hydro scheme". Computation of Power, Energy, Information and Communication (ICCPEIC), Vol. 1, Pages 124 - 129, 2014.

[9] IEEE STD 519-1992. "IEEE Recommended Practices and Requirements for Harmonic Control in Electrical Power Systems". New York, 1993.

[10] R. L. Nailen. "Spooks on the Power Line? Induction Generators and the Public Utility". IEEE Transaction on Industry Applications, Vol. 1A-18, No. 6, 1982.

[11] A. S. Magalhães; L. C. A. Junior; C. A. Matias; A. H. F. Silva; E. G. Domingues; A. J. Alves and W. P. Calixto. "Repowering of a Synchronous Generation Plant by Induction Generator." IEEE Congreso Chileno de Ingeniería Eléctrica, Electrónica, Tecnologías de la Información y Comunicaciones (IEEE CHILECON 2015), 2015, Santiago.

[12] E. Delbone. " Harmonic Attenuation in the Synchronous Generator due the Nonlinear Loads Using Induction Generators". Thesis in Portuguese, Federal University of Uberlandia, Uberlandia, Minas Gerais, Brazil, 2012.

[13] R. Behome; M. Plamondon, H. Nakra, D. Desrosiers, C. Gagnon. " Steam Power Plant Re-powering to provide Black-Start Ancillary Service and speed up Power System Restoration". IEEE Bologna PowerTech Conference, 2003.

[14] A. Gaglianoa, G. M. Tinab, F. Noceraa , F. Patania. " Technical and Economic Perspective for Repowering of Micro Hydro Power Plants: a Case Study of an Early XX Century Power Plant". Energy Procedia, 6th International Conference on Sustainability in Energy and Buildings, SEB-14, 2014.